

**Exploring New Satellite Technology for Extratropical Cyclone and Surface Heat Flux
Analysis**

by

Juan A. Crespo

A dissertation submitted in partial fulfillment
of the requirements for the degree of
Doctor of Philosophy
(Atmospheric, Oceanic, and Space Sciences)
in The University of Michigan
2018

Doctoral Committee:

Dr. Derek J. Posselt, NASA Jet Propulsion Laboratory, Co-Chair
Professor Christopher S. Ruf, Co-Chair
Associate Professor Mark G. Flanner
Associate Professor Valeriy Y. Ivanov
Assistant Professor Gretchen Keppel-Aleks

Juan A. Crespo

crespoj@umich.edu

ORCID iD: 0000-0002-6044-7838

© Juan A. Crespo, 2018

For my parents, who always encouraged me to go one-step further.

Great are the works of the Lord, studied by all who delight in them.
Psalm 111:2

Acknowledgements

I first want to thank Dr. Derek Posselt, my advisor and mentor since 2011. He is the one who stirred my interest in extratropical cyclones and always encouraged me to think outside the box, to the point where I am trying to use a tropical satellite to study storms that do not form in the tropics. I would also like to thank my co-chair, Dr. Chris Ruf, and the rest of my committee, Drs. Gretchen Keppel-Aleks, Mark Flanner, and Valeriy Ivanov, who have offered critical, vital, and priceless feedback throughout the dissertation process. I would also like to thank my various collaborators and those who have offered assistance throughout my graduate school career, such as Drs. Mark Kulie, Catherine Naud, Charles Bussy-Virat, J. Brent Roberts, and Timothy Lang.

I would also like to thank my Atmospheric Observations, Simulations, and Statistics (AOSS) group labmates: Omar, Greg, Sam, David, Annareli, and Fei. They have been a great source for feedback and sanity even after we have parted ways. Additionally, many thanks to all the friends I have made within AOSS/CLaSP/UofM, St. Francis of Assisi, throughout Ann Arbor, and those who I have stayed in touch with from Purdue, Indiana, and beyond. You have all been a source of joy and light even during the darkest of days, and I am forever grateful to you all.

Last but certainly not least, I have to thank my parents, Isabel and Carlos Crespo. They recognized my passion for science early on and always encouraged me to go the extra mile, even if I was a stubborn and spoiled child. They came to this amazing country in order to give our family a better future. I will never fully comprehend the sacrifices they have made and the endless love they have for us. I love you for all that you have done for our family and me.

Preface

This dissertation is a collection of work that has been published in other scholarly journals, or will be submitted for publication in the near future. Chapter 2 has been published in *Monthly Weather Review* (Crespo and Posselt 2016) and Chapter 4 has been published in the *Journal of Applied Meteorology and Climatology* (Crespo et al. 2017). Both are being used as chapters with permission from the American Meteorological Society. Chapter 5 is being prepared for submission to a peer-reviewed journal when this dissertation is to be submitted.

Table of Contents

Dedication	ii
Acknowledgements	iii
Preface	iv
List of Tables	vii
List of Figures	viii
Abstract	xi
Chapter 1: Introduction	1
1.1 Introduction to Extratropical Cyclones	1
1.2 Influence of Surface Heat Fluxes on Extratropical Cyclones	5
1.3 Current Methods of Observing Surface Heat Fluxes from Spaceborne Instruments	8
1.4 The Cyclone Global Navigation Satellite System and its application for Surface Heat Flux and Extratropical Cyclone Analysis	10
1.5 Organization of Thesis	12
Chapter 2: A-Train-Based Case Study of Stratiform–Convective Transition within a Warm Conveyor Belt	16
2.1 Introduction	16
2.2 Data and Methods	19
2.3 Synoptic Overview	21
2.4 Analysis of A-Train Products	23
2.4.1 2D Overview	23
2.4.2 Vertical Structure	24
2.4.3 AMSR-E 89 GHz Scattering Index	27
2.5 Implications for Satellite Storm Sampling Frequency	30
2.6 Summary and Conclusions	32
Chapter 3: Surface Heat Flux Analysis Around Extratropical Cyclones	43
3.1 Introduction	43
3.2 Latent and Sensible Heat Fluxes Observed during the November 2006 Case Study	45
3.3 Estimating Surface Heat Fluxes from Spaceborne Instruments	47
3.4 Conclusions	49
Chapter 4: Assessing CYGNSS’s Potential to Observe Extratropical Fronts and Cyclones	53
4.1 Introduction	53

4.2 Data and Methods.....	54
4.2.1 Simulated CYGNSS Ground Tracks and Specular Point Locations	54
4.2.2 Cyclone and Front Detection and Compositing Methodology	55
4.3 Results	57
4.4 Conclusions	61
Chapter 5: CYGNSS Estimates of Latent and Sensible Heat Fluxes	66
5.1 Introduction	66
5.2 Data and Methods	67
5.2.1 COARE 3.5 Algorithm	67
5.2.2 Inputs to COARE from CYGNSS	69
5.2.3 Inputs to COARE from MERRA-2	70
5.2.4 Simple Sensitivity Analysis	71
5.3 Results	72
5.3.1 CYGNSS Surface Wind Observations of Extratropical Cyclones	72
5.3.2 CYGNSS Estimates of Surface Heat Fluxes around Extratropical Cyclones	74
5.3.3 Comparisons of CYGNSS Surface Heat Fluxes with KEO	76
5.3.4 COARE 3.5 Sensitivity Analysis	78
5.4 Conclusions	80
Chapter 6: Conclusions	92
6.1 Summary of Thesis	92
6.2 Future Work	95
6.3 Importance of Thesis	98
References	100

List of Tables

Table 5.1. Comparisons of latent and sensible heat flux (W/m^2) estimates from KEO, CYGNSS, and MERRA-2	83
Table 5.2. Comparisons of surface wind speeds from KEO, CYGNSS, and MERRA-2, which correspond to the same times listed in Table 5.1	83
Table 5.3. Results from the simple sensitivity analysis of the COARE 3.5 algorithm, as a result when one inputs the standard deviation (σ) for each variable. Top table are the results for the entire CYGNSS constellation on 15 September 2017, and the bottom table is from the same day, but within a 25 km radius of the KEO buoy (32.3°N , 144.6°E)	84
Table 5.4. Same sensitivity analysis from Table 5.3, but with $100 \text{ W}/\text{m}^2$ binned results of latent heat flux	84

List of Figures

- Figure 1.1.** The Norwegian Cyclone Model adopted from Bjerknes and Solberg (1922). Streamlines in top portion show the direction of wind, with gray areas highlight areas of precipitation, and dashed lines as frontal boundaries. Each step is as follows: (I) incipient frontal cyclone, (II and III) narrowing of the warm sector, and (IV) occlusion. Bottom portion highlights the cross section from the dotted line in the top portion of the image. 14
- Figure 1.2.** The Shapiro and Keyser Extratropical Cyclone Model (Shapiro and Keyser 1990). Top shows lower tropospheric geopotential height contours and frontal locations, gray areas highlight precipitation areas, while the bottom shows lower tropospheric potential temperatures, with cold on the north and warm on the south. Each step is as follows: (I) incipient frontal cyclone, (II) frontal fracture, (III) frontal T-bone and bent-back front, and (IV) frontal T-bone and warm seclusion..... 15
- Figure 2.1.** GFS Analysis for 1800 UTZ 21 Nov (a, d, g), 0600 UTC 22 Nov (b, e, h), and 1800 UTC 22 Nov (c, f, j). Row a-c: 300 hPa geopotential heights (m, black contours) and wind speed (m/s, colored). Row d-f: 700 hPa wind (knots, wind barbs) and total column precipitable water (mm, colored). Row g-j: 850 hPa Potential Temperature (K, colored) and sea level pressure (hPa, black contours). X marks the approximate location of the surface low center..... 36
- Figure 2.2.** GFS Analysis for 0600 UTZ 23 Nov (a, d, g), 1800 UTC 23 Nov (b, e, h), and 0600 UTC 24 Nov (c, f, j). Row a-c: 300 hPa geopotential heights (m, black contours) and wind speed (m/s, colored). Row d-f: 700 hPa wind (knots, wind barbs) and total column precipitable water (mm, colored). Row g-j: 850 hPa Potential Temperature (K, colored) and sea level pressure (hPa, black contours). X marks the approximate location of the surface low center..... 37
- Figure 2.3.** MODIS observed cloud top pressure (units: hPa) around approximately a) 1800 UTC 21 Nov, b) 0600 UTC 22 Nov, c) 1800 UTC 22 Nov, d) 0600 UTC 23 Nov, e) 1800 UTC 23 Nov, and g) 0600 UTC 24 Nov. The white regions indicate missing data. X marks the approximate location of the surface low center. 38
- Figure 2.4.** AMSR-E observed water vapor (a, d, g; Units: mm), cloud liquid water (b, e, h; Units: mm), and rain rate (c, f, j; Units: mm/hour) at approximately 0600 UTC 22 Nov (a-c), 1800 UTC 22 Nov (d-f), and 0600 UTC 24 Nov (g-j). X marks the approximate location of the surface low center..... 39
- Figure 2.5.** CloudSat Radar Reflectivity (dBZe) with Equivalent Potential Temperature (K, contours) and precipitation rate (black line plot, red values indicate missing data) at approximately a) 0600 UTC 22 Nov, b) 1800 UTC 22 Nov, and c) 0600 UTC 24 Nov 2006. Equivalent potential temperature is computed from ECMWF temperature and water vapor mixing ratio fields interpolated to the CloudSat track..... 40

- Figure 2.6.** AMSR-E 89 GHz vertically polarized brightness temperature (a, d, and g), vertical – horizontal polarized brightness temperature difference (b, e, and h), and scattering index (c, f, and i) for 0659 UTC 22 November (a, b, and c), 1704 UTC 22 November (d, e, and f), and 0647 UTC 24 November (g, h, and i). Colored values correspond to values of each quantity, and the 10 GHz S89 value is contoured in black in (c, f, and i). X marks the approximate location of the surface low center..... 41
- Figure 2.7.** 89 GHz scattering index (S89) relative frequency of occurrence statistics for the three AMSR-E overpass times and geographic regions depicted in Fig. 7. Only pixels with S89 values exceeding 10 K, and with associated AMSR-E surface precipitation rate retrievals exceeding 2 mm h^{-1} are used to create the S89 histograms..... 42
- Figure 3.1.** Surface latent heat flux (top, units: W/m^2) and sensible heat flux (bottom, units: W/m^2) on 21 November 1200 UTC (left), 22 November 1200 UTC (middle), and 23 November 1200 UTC (right); all overlaid with wind barbs of surface winds (m/s). L marks the approximate location of the cyclone center..... 51
- Figure 3.2.** QuikSCAT observations from 22 November approximately 0700 to 1100 UTC. Left: Estimated surface wind speeds in knots. Right: Rain impact on surface wind observations, where: 0 = no rain impact, 10 = high rain impact..... 52
- Figure 4.1.** Frequency with which simulated CYGNSS specular points will pass within (a) 500 km of a low pressure center, (b) 25 km of a warm front, and (c) 25 km of a cold front over 2 years. The results are gridded into $5^\circ \times 5^\circ$ latitude/longitude boxes, and only results over ocean are shown. (d) Depiction of one day of simulated CYGNSS orbits showing the extent of coverage of each observatory in the constellation..... 63
- Figure 4.2.** Distribution of winds (top row), latent heat flux (LHF; middle row), and sensible heat flux (SHF; bottom row) across cold fronts (left column) and warm fronts (right column) within the latitude range 40°S to 40°N . Shown are the results from the full set of storms (black lines), 2014 only (blue lines), and 2015 only (red lines) for the CYGNSS sample (solid) and the full sample (dashed) 64
- Figure 4.3.** Frequency distribution of surface wind speeds (top row), latent heat flux (LHF; middle row), and sensible heat flux (SHF; bottom row) for cold fronts (left column) and warm fronts (right column). Results are divided into samples that occur only on the poleward and westward (cold) side of the cold and warm fronts (blue), only on the equatorward and eastward (warm) side of cold and warm fronts (red), and all samples (black). As in Fig. 2, the CYGNSS sample is represented by solid lines, while the full sample is dashed..... 65
- Figure 5.1.** CYGNSS surface wind [m/s] observations on 21 March 2017. Mean sea level pressure (hPa, black contour) shown at 00z (top) and 21z (bottom), with CYGNSS winds ± 3 hours around this time..... 85
- Figure 5.2.** CYGNSS surface wind [m/s] observations on 30 Oct. 2017. Mean sea level pressure (hPa, black contour) shown at 00z (top) and 03z (bottom), with CYGNSS winds ± 3 hours around this time..... 86
- Figure 5.3.** Latent (top) and sensible (bottom) heat flux estimates [W/m^2] on 21 March 2017. Mean sea level pressure (hPa, black contour) shown at 21z, with CYGNSS heat fluxes ± 3 hours around this time..... 87
- Figure 5.4.** Latent (top) and sensible (bottom) heat flux estimates [W/m^2] on 30 October 2017. Mean sea level pressure (hPa, black contour) shown at 03z, with CYGNSS heat fluxes ± 3 hours around this time..... 88

Figure 5.5. Latent heat flux estimates (W/m^2) on 15 (top) and 16 (bottom) September 2017 of Typhoon Talim. Mean sea level pressure (hPa, black contour) shown at 1200 UTC each day, with CYGNSS heat fluxes ± 3 hours around each time period.....	89
Figure 5.6. From Garfinkel et al. (2011), relation of the drag coefficient ($C_{D10N} \times 1000$) and wind speed (U_{10N}) between various heat flux algorithms.....	90
Figure 5.7. Distribution of latent heat flux estimates (W/m^2) across an entire day (15 Sept 2017), with bins of $50 \text{ W}/\text{m}^2$	91
Figure 5.8. Same as Figure 5.7, but with sensible heat flux (W/m^2) with bins of $10 \text{ W}/\text{m}^2$	91

Abstract

Extratropical cyclones play a large role in every day weather and Earth's general climate, as they not only transport energy and moisture between the lower and higher latitudes, but also are associated with many extreme weather events observed across the globe. Throughout the winter of 2017 and 2018, we have already seen the impact extratropical cyclones have here in the United States. In December 2017, an extratropical cyclone brought snow as far south as Louisiana, and dumped up to six inches throughout Mississippi and Alabama. One month later, the nation was captivated as a "bomb cyclone" developed in the western Atlantic Ocean before making landfall in New England, causing blizzard conditions and affecting travel in one of the busiest corridors in the United States.

Given their importance, it is critical that we build an understanding of how these systems develop at all scales, as well as surface processes involved in their genesis and evolution. While the scientific community has a good understanding of how extratropical cyclones develop at the synoptic scale thanks to nearly a century of research, there are still uncertainties when it comes to understanding how these systems develop at the mesoscale and microscale, as well as how surface processes could play a role in their development. This thesis offers a new understanding of how extratropical cyclones can develop by using existing and new satellite technologies that offer a unique analysis. For example, by using the existing NASA Afternoon-Train (A-Train) observations, we are able to observe a stratiform-to-convective transition within the warm front, something that had not been observed from a remote sensing platform before at this time.

This fascinating transition raised more questions regarding how and why this transition occurred. One theory was the involvement of surface heat fluxes, as previous research has shown their influence on extratropical cyclone development. Given the importance of surface heat fluxes on not only marine-based extratropical cyclones, but also other weather phenomenon, it is important to consistently observe these fluxes. With the lack of in-situ measurements over the world's oceans, spaceborne instruments need to be able to fill in this gap. By using the recently launched Cyclone Global Navigation Satellite System (CYGNSS), which offers improved estimates of surface wind speeds in nearly all weather conditions across the tropical and subtropical oceans, we can get better estimates of surface heat fluxes. While CYGNSS is a tropical mission, it is able to continuously observe extratropical cyclones that form in the lower latitudes, especially in areas where surface heat fluxes are strongest, such as off the coast of Japan and off the East Coast of the United States. This thesis highlights wind speed observations and surface heat flux estimates within and around some low-latitude extratropical cyclones that were observed in CYGNSS's first year in orbit. These new CYGNSS observations offer a unique perspective of extratropical cyclone genesis and evolution, as this thesis lays the foundation for potential future satellite missions that aim to estimate surface heat fluxes from space.

Chapter 1: Introduction

1.1 Introduction to Extratropical Cyclones

Extratropical Cyclones (ETCs) play an important role in Earth's climate as they regulate the planet's energy balance through meridional transportation of energy from the equator poleward, as well as through the effects from the clouds they produce within the climate system. They are primarily driven by temperature and moisture gradients between the warm equatorial regions and the colder middle and high latitudes. This leads to ETCs primarily forming during the winter seasons around the midlatitudes in both hemispheres, as the two air masses are separated by boundaries of large temperature gradients, leading to the cyclone's cloud and precipitation formation (Bjerknes and Solberg 1922; Oort 1971; Field & Wood 2007). ETCs are an important source of freshwater in the middle and high latitudes, and are associated with a majority of the precipitation observed in the planet's temperature zones (Heideman and Fritsch 1988; Hawcroft et al. 2012; Catto 2016). Additionally, up to 90% of rainfall observed in storm track regions are being produced by fronts associated with ETCs (Catto et al. 2012).

A majority of the water vapor that is converted into clouds and precipitation within extratropical fronts and cyclones originates within the planetary boundary layer (PBL) equatorward of the cyclone center. This moisture is transported by the poleward-ascending warm conveyor belt airstream (Harrold 1973; Browning et al. 1973; Carlson 1980; Browning 1986; Wernli 1997; Eckhardt et al. 2004; Madonna et al. 2014; Catto 2016). The warm conveyor belt (WCB) efficiently precipitates nearly all the moisture they transport into the ETC, making a

substantial contribution to the total precipitation in the extratropics. WCBs produce approximately half of the wintertime precipitation (Eckhardt et al. 2004; Field and Wood 2007) and are associated with more than 70% of the annual extreme precipitation events observed in the southeastern United States, eastern China, Japan, and South America (Pfahl et al. 2014).

Since WCBs are associated with ETCs, they are more frequently observed during the winter seasons compared to summer in both hemispheres, though there is a stronger seasonal cycle in the Northern Hemisphere. WCBs are frequent in regions of intense baroclinicity and high low-level moisture content (Stohl 2001; Eckhardt et al. 2004; Madonna et al. 2014). Since warm conveyor belts mainly originate in the moist subtropical marine PBL between 20° and 47° in the Northern Hemisphere, they can transport large quantities of sensible and latent heat upward and poleward (Browning 1990, Wernli and Davies 1997; Madonna et al. 2014). These moisture sources for WCBs are typically located over the ocean and close to their respective starting points, with their uptake of moisture often being associated with anomalies of latent heat flux due to a reduction of near-surface relative humidity and enhanced wind velocity (Neiman and Shapiro 1993; Pfahl et al. 2014). As the air in the WCB rapidly progresses poleward during its ascent, the specific humidity decreases significantly as the water vapor condenses (Madonna et al. 2014), leading to the production of clouds and precipitation, which are strongly correlated to the amount of moisture transported by the WCB (Field and Wood 2007).

The community's modern day understanding of extratropical cyclones originated from the Norwegian Cyclone Model, developed by Jacob Bjerknes in the early 20th century at the Bergen School of Meteorology. By using surface based observations throughout Western Europe, as well as some aerial observations through kite soundings, visual ground observations of clouds aloft, and observations along mountain slopes, Bjerknes was able to show, three-dimensionally, how

cyclones formed, evolved, and dissipated throughout their lifetime. The Norwegian Cyclone Model (Figure 1.1) shows that the initial phase of an extratropical cyclone begins when two air currents of different temperatures are flowing in opposite directions, with a continuous boundary separating the two air masses. The temperature and flow difference induce a cyclone formation, forming the cyclone center (Bjerknes 1919).

In a typical cyclone in the Northern Hemisphere, the cold dry air begins to curve around the north and west portions of the cyclone center, forming the cold front to the south of the center. Meanwhile, warm moist air dominates the southeastern portion of the system and pushes poleward, forming the warm front east of the cyclone. The cold and warm fronts act as boundaries, and were originally estimated to go from the surface to the tropopause. However, further observational studies showed a separation between upper-air dynamics and low-level surface fronts (Reed and Sanders 1953, Shapiro 1970). As the cyclone center moves eastward, the cold front pushes warm air aloft and narrows the warm sector, catching up to the poleward moving warm front. Eventually, these two fronts combine to form an occlusion, with only cold air circulating at the surface of the cyclone and warm air aloft, increasing the stability of the atmosphere, causing the cyclone to weaken and dissipate (Bjerknes 1919, Bjerknes and Solberg 1922).

With the advent of electronic computing in the latter half of the 20th century, researchers were able to develop idealized numerical studies of baroclinic waves and simulations initialized with real data. Since observations were limited over the oceans (compared to observations over land), this gave researchers a better chance at understanding how marine-based extratropical cyclones developed. These studies observed a loss of cold frontal baroclinicity near the cyclone center during the early stages of cyclogenesis, a subsequent westward migratory warm front going into the northerly flow west of the cyclone, and the formation of warm air seclusion in the fully

developed cyclone surrounded by post-cold frontal air (Shapiro and Keyser 1990, Hoskins and West 1979, Keyser et al. 1989). However, since these idealized simulations differed from the Norwegian Cyclone Model, especially its occlusion described in the latter half of its life, the researchers were hesitant to apply these results and modify the cyclone model, let alone suggest an alternative until these results could be compared to real-life cyclones.

Shapiro and Keyser (1990) were able to show, with observations of a marine extratropical cyclone, that the previous model simulations were indeed representing the real atmosphere. In a case study from 1987 over the northern Pacific Ocean, they observed a frontal T-Bone structure as the ETC matured, with an east-west oriented warm front bridging across the cyclone center into the northerly flow west of the cyclone, as well as the warm air seclusion as the post-cold frontal air wrapped around the cyclone center. These results, along with other case studies and field campaigns, finally showed that the idealized models of marine ETCs were correct, but that the Norwegian Cyclone Model could not represent them well. This led to the creation of the Shapiro-Keyser Cyclone Model (Figure 1.2). It described the formation and evolution of marine extratropical cyclones with four phases: 1) a continuous and broad front, 2) frontal facture in the vicinity of the cyclone center with discontinuous warm/cold front gradients, 3) frontal T-bone and back bent warm front, and finally 4) warm-core seclusion within the post-cold frontal air stream. The Shapiro-Keyser Cyclonic Model was meant to compliment, not replace, the Norwegian Cyclone Model, and is specifically geared towards marine-based ETCs, while the former is now geared towards describing land-based ETCs (Shapiro and Keyser 1990).

While there are certainly case studies of ETCs that may not conform to either one of these cyclonic models, these cyclonic models have increased our understanding of how extratropical cyclones form and develop at the synoptic level. However, there remain unanswered questions

associated with how changes in cyclone circulation and environment relate to variations to the distribution and intensity of clouds and precipitation, along with how surface processes, especially over the ocean, relate to ETC development. Numerous case studies have examined the dynamics of the flow through the warm conveyor belt, as well as the effect of condensational heating within the WCB on ETC strength and structure. Previous studies have examined the effect of latent heating on storm strength and structure (e.g., Stoelinga 1996; Businger et al. 2005) while other case studies have focused specifically on frontal structure (Posselt and Martin 2004; Igel and van den Heever 2014) and the WCB itself (Boutle et al. 2011; Joos and Wernli 2012; Flaounas et al. 2016). While significant progress has been made with various field campaigns and modelling studies, there is much to examine regarding the influence of surface heat fluxes and their impact on marine-based extratropical cyclones, as well how one can continually observe these surface heat fluxes using remote sensing instruments.

1.2 Influence of Surface Heat Fluxes on Extratropical Cyclones

Surface sensible (SHF) and latent (LHF) heat fluxes are primarily driven by surface winds and differences in temperature and humidity between the surface and the lower planetary boundary layer (~10 meters above the surface). Over the world's oceans, these fluxes are driven by turbulent motions within the PBL, and are an important component in general air-sea interaction, as they transport mass, momentum, and energy between the surface and lower troposphere (Hartmann 1994). While there are various ways to compute surface heat fluxes, one of the most common methods is to use the bulk aerodynamic formulas,

$$LHF = \rho_a L_v C_{DE} U (q_s - q_a) \text{ (Eqn. 1.1)}$$

$$SHF = \rho_a c_p C_{DH} U (T_s - T_a) \text{ (Eqn. 1.2)}$$

where ρ is air density at the surface, L_v is the latent heat of condensation, and c_p is specific heat at constant pressure. C_{DH} and C_{DE} are the exchange coefficients of sensible heat and moisture (respectively), U is surface winds, T_s and T_a are temperature at the surface and 10 meters (respectively), and q_s and q_a are specific humidity at the surface and 10 meters (respectively).

Surface heat fluxes have an impact on everyday weather and climate, and they serve a large role in the development of extratropical cyclones, especially as they form over the Earth's oceans near landmasses. Extreme marine cyclogenesis and "bomb" cyclones (where the surface pressure drops 24 hPa in 24 hours) tend to occur east of cold continental landmasses with large sea surface temperature (SST) gradients in the immediate vicinity (Sanders and Gyakum 1980). Such examples include the Gulf Stream and Kuroshio Currents that run parallel to the North American and Japanese East Coasts, respectively. During the winter seasons, both of these warm currents are flowing parallel to cold continental air masses, making this a prime area for marine cyclogenesis. As a low pressure system begins to form near the coast, the cyclonic rotation pulls the cold and dry air from the continent over the warm ocean currents. This leads to large vertical gradients of temperature and specific humidity, and as Equation 1 shows, leads to an increase in latent and sensible heat fluxes the greater these differences become. These fluxes and associated instability can magnify the closer these warm ocean currents are to cold continental air masses (Cione et al. 1993).

While strong vertical gradients of temperature and specific humidity play a role in surface heat fluxes, surface winds also play an important role in these fluxes, as we see in Equation 1. Strong surface winds from ETCs can increase LHF and SHF as they induce turbulence near the surface, causing the exchange of momentum and energy between the air and sea to increase. Previous studies have noted that as these surface heat fluxes increase from the strong surface winds

of an extratropical cyclone, the baroclinicity and instability within the boundary layer increases, which can cause rapid intensification of these cyclones (Vukovich et al. 1991; Cione et al. 1993; Catto 2016). Additionally, the exchange coefficients (C_{DH} and C_{DE}) are computed as functions of wind, but become less certain with higher wind speeds (Neiman and Shapiro 1993).

One case study that highlighted the impact that surface fluxes have on extratropical cyclones was the work of Neiman and Shapiro (1993), as they analyzed a powerful extratropical cyclone observed during the Experiment on Rapidly Intensifying Cyclones over the Atlantic (ERICA) field campaign in January 1989. As this cyclone formed off the East Coast of the United States over the warm Gulf Stream current, it pulled cold and dry continental air from the west over the warm and moist ocean surface. Coupled with the strong winds associated with this ETC and the close proximity of the Gulf Stream in relation to the US coastline, the combined latent and sensible heat fluxes peaked around 1300 W/m^2 near the cyclone center, reducing the static stability in this region (Vukovich et al. 1991). With the reduced static stability, the increased surface fluxes led to perturbations and an increase in baroclinicity within the boundary layer (Cione et al. 1993), causing the surface pressure of the cyclone to drop by 60 hPa within 24 hours, officially defining this storm as a meteorological “bomb” (Sanders and Gyakum 1980). Though positive latent and sensible heat fluxes are typically the focus of this analysis, this case study also highlighted the importance of negative heat fluxes (where 10-meter temperature and humidity are greater than the surface). These negative fluxes, though lower than their positive counterparts, can direct energy away from the cyclones into a colder surface below, which can hamper cyclogenesis and ETC maturation. Ultimately, Neiman and Shapiro (1993) showed that latent and sensible heat fluxes play an extremely crucial role in extreme marine cyclogenesis and evolution, and continues to merit their study and analysis. Chapter 3 will offer a more in depth analysis of the role surface

fluxes could have played on an extratropical cyclone that was analyzed by Crespo and Posselt (2016).

Though we know that surface sensible and latent heat fluxes play an important role in marine extratropical cyclone development, we currently lack consistent in situ measurements and estimations within marine-based ETCs due to poor spatial coverage offered by buoys. Though field campaigns can offer detailed analysis of some ETCs and have paved the way for our current understanding of surface heat fluxes and their role in cyclogenesis, they are often limited to a particular area and do not offer continuous coverage. Given how important surface heat fluxes are in understanding and forecasting extratropical cyclones and other weather phenomenon, our community needs improved and consistent measurements and estimates of surface sensible and latent heat fluxes. Current estimates are limited due to a lack of in-situ observations and current satellite technology being unable to accurately estimate surface fluxes due to attenuation and gaps in coverage from the orbits. By exploring the possibility of estimating surface heat fluxes from space, we can help fill in this gap in an area of need for our community.

1.3 Current Methods of Observing Surface Heat Fluxes from Spaceborne Instruments

While proper estimates of surface heat fluxes are crucial in understanding marine based extratropical cyclones, as well as properly forecasting them, current surface heat flux measurements have been limited to a few buoys and some field campaigns. Though these observations can offer detailed estimates at their respective time and location, they do not offer sufficient temporal and spatial coverage to study large-scale phenomena. Given that surface heat fluxes can vary on small temporal and spatial scales, the ability to estimate surface heat fluxes

from space using remote sensing instruments can help fill in some gaps where in situ observations are lacking.

While satellite observations can provide improved spatial and temporal coverage, current remote sensing technology is not able to observe sensible and latent heat fluxes from space directly. Though current satellite technology cannot make direct observations of these fluxes, they can observe the components needed to estimate LHF and SHF using spaceborne instruments, such as temperature and wind speed (Singh et al. 2005), and compute the fluxes using these measurements. The Special Sensor Microwave/Imager (SSM/I) instruments, which are part of the Defense Meteorological Satellite Program (DMSP), are one of the few current spaceborne instruments that can provide estimates of latent heat fluxes, as it estimates fluxes using measurements of temperature, humidity, and wind speed. As a microwave radiometer, it can provide key observations at the surface, which are used to derive near-surface products, such as humidity and wind speeds (Wentz 2013). Though SSM/I can be considered a complete package, it is possible to estimate surface heat fluxes using a combination of scatterometers (e.g., QuickSCAT, ASCAT), radiometers (e.g. AMSR-E, AMSU), and even reanalysis data (e.g., MERRA-2) to fill in necessary gaps.

Regardless of method, nearly all satellite instruments mentioned have a major weakness: thick cloud cover and precipitation. Given that many of these instruments observe within the microwave spectrum, clouds and precipitation attenuate their signals, causing inaccurate or missing estimates of components like humidity and wind speed. Along with signal attenuation, most of these satellites are polar orbiting; while this provides observations towards the upper latitudes, this often leads to poor temporal sampling with high revisit times. Additionally, if the field of view is too narrow, there can be significant gaps between swaths of these polar orbiting

satellites, possibly missing key aspects of a weather system. Though these inaccuracies and missing data for each individual component may be minimal, the inaccuracies could greatly affect estimates of latent and sensible heat fluxes. At best, one can simply ignore these inaccuracies and not compute surface heat fluxes whenever they occur, but this can lead to large gaps of estimates that may already have a significant amount of missing data. However, a new satellite mission launched in 2016 could provide the foundation needed to improve our estimates of SHF and LHF from a remote sensing perspective.

1.4 The Cyclone Global Navigation Satellite System and its application for Surface Heat Flux and Extratropical Cyclone Analysis

The Cyclone Global Navigation Satellite System (CYGNSS), launched on 15 December 2016, is a constellation of eight satellites that are designed to estimate surface winds over the tropical and subtropical oceans as part of a new NASA Earth Science Mission. Each CYGNSS satellite is able to measure Global Positional Satellite (GPS) navigation signals scattered by the ocean using a delayed Doppler mapping instrument (DDMI) that consists of a multichannel Global Navigation Satellite System reflectometry (GNSS-R) receiver, low-gain zenith antenna for reception of direct signals, and two high-gain nadir antennas for surface scattered signal reception. The scattered GPS signals are then used to derive wind speeds 10 meters above the surface. CYGNSS uses the GPS L1 channel (1575 MHz, 19-cm wavelength), which does not experience appreciable attenuation in the presence of precipitation. Because of this technology, CYGNSS is designed to observe and estimate surface winds within the core of tropical cyclones, which could not be previously measured accurately with other spaceborne instruments. With a low-inclination orbit of 35°, CYGNSS will maximize its spatial and temporal sampling within the tropics; each

CYGNSS observatory is able to observe up to four specular points per second whenever they are in science data collecting mode (32 specular points/second for the entire constellation). With low revisit times, CYGNSS is better able to observe a tropical cyclone's rapid intensification and evolution, which can lead to improved forecast with a better understanding of inner-core processes (Ruf et al. 2013, 2016).

Though CYGNSS is designed for tropical cyclone research, its orbit inclination of 35° comes far enough poleward to begin to observe extratropical cyclones forming in the lower latitudes. Early on-orbit results have shown that CYGNSS can consistently make observations as far as 37° , with some observations reaching the 40^{th} parallel in both hemispheres. While CYGNSS will only observe a small portion of extratropical cyclones that form throughout the globe, it is able to observe areas of extreme marine cyclogenesis, such as those mentioned in section 1.2. Chapter 4 will further discuss Crespo et al. (2017), which looks into how often CYGNSS is expected to observe ETCs forming in the lower latitudes using a climatological data of cyclone centers and fronts along with an orbit simulated that projected two years of CYGNSS orbits and observation locations.

Given CYGNSS's ability to provide improved estimates of wind speeds, the theory behind this thesis is that these improved wind speeds in all conditions can provide improved estimates of latent and sensible heat fluxes within and around extratropical cyclones and other tropical convection. However, CYGNSS is only able to estimate surface winds; though this gives us two of main components of surface heat fluxes (wind speed and exchange coefficient) other sources must be used for temperature and specific humidity in order to calculate effective estimates. The second version of the Modern-Era Retrospective analysis for Research and Applications (MERRA-2) reanalysis dataset is being used to fill in these gaps, as it utilizes satellite observations

in its reanalysis procedure, and is an hourly dataset, reducing possible temporal errors and assumptions. As discussed in Chapter 5, future estimates of surface heat fluxes from CYGNSS will utilize satellite observations and estimates of temperature and specific humidity, which will then be used to develop a product that will be made available for the entire CYGNSS mission.

Previous research has shown that surface sensible and latent heat fluxes play a critical role in the development and evolution of marine-based extratropical cyclones. As stated in section 1.1, ETCs are an integral part of Earth's energy balance, climate, and weather. By offering better remote sensing based observations of surface heat fluxes associated with ETCs, it will allow our community to have an improved dataset for low-latitude ETC analysis. Though CYGNSS may only observe part of what is needed to estimate these fluxes, this thesis effectively lays the foundation for improved LHF and SHF estimates from spaceborne instruments, as well as possible future follow on missions for CYGNSS. As satellite technology continues to improve, it is the hope of the author that we will see multiple instruments being able to observe and estimate surface heat fluxes in all conditions with improved temporal and spatial sampling.

1.5 Organization of Thesis

While there are many aspects of extratropical cyclones to observe and many tools from which to observe them, this thesis focuses on a few case studies observed by NASA's Afternoon Train Satellite Constellation (A-Train) and the Cyclone Global Navigation Satellite System (CYGNSS). Chapters 2 and 3 are based on the same case study of a long-lived marine based extratropical cyclone that travelled parallel to the East Coast of the United States in late November 2006. Chapter 2 is based on the work of Crespo and Posselt (2016), and provides a detailed look in how this ETC developed, focusing on satellite based observations, and how its associated warm

front transitioned into a convective and unstable structure. Chapter 3 provides some insights into how surface heat fluxes might have played a role in this ETC's rapid development and warm frontal convective transition. It also provides motivation and transitions into Chapter 4, where we examine how CYGNSS can observe the surface processes of extratropical cyclones, despite its tropical orbit, by using an orbit simulator and database of previously observed ETCs. This chapter is based on the work presented in Crespo et al. (2017).

Chapter 5 focuses on developing surface heat flux estimates using CYGNSS surface winds and the COARE 3.5 algorithm, a well-known tool used throughout the air-sea community. We will combine wind speed observations from CYGNSS and estimate surface heat fluxes along its tracks, to not only observe if CYGNSS can provide these types of observations, but also offer some analysis of some of the extratropical cyclones it has observed within its first year on orbit. We will also compare the results from CYGNSS to some ground truth and reanalysis data to see how well this method does in comparison to other sources. Additionally, this chapter will conclude with a simple sensitivity analysis and see how known errors in the input data could impact the results produced through the COARE 3.5 algorithm. Finally, chapter 6 rounds out this thesis with a details summary, as well as providing steps for future work and the development of the CYGNSS Surface Heat Flux Product, which aims to provide surface heat fluxes for the entire CYGNSS mission. We conclude this chapter with a reminder of why this analysis is important, and how we can set the foundation for future scientific missions.

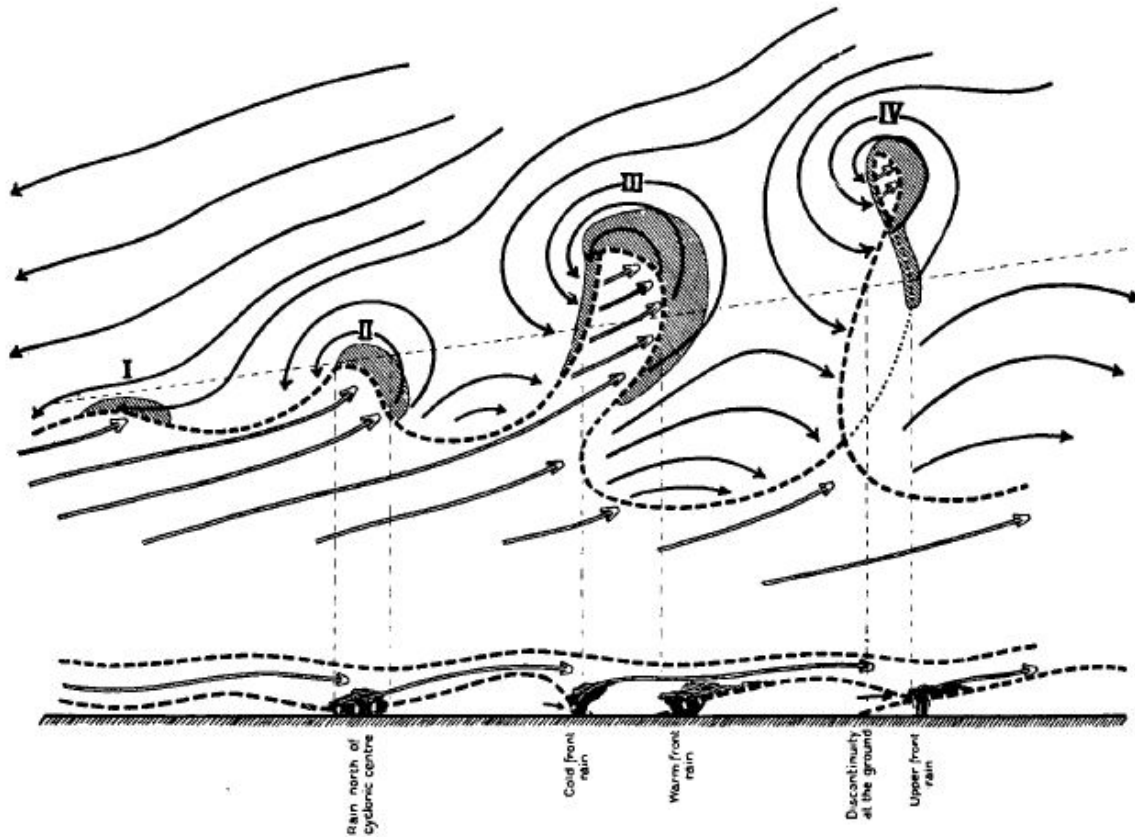


Figure 1.1: The Norwegian Cyclone Model adopted from Bjerknes and Solberg (1922). Streamlines in top portion show the direction of wind, with gray areas highlight areas of precipitation, and dashed lines as frontal boundaries. Each step is as follows: (I) incipient frontal cyclone, (II and III) narrowing of the warm sector, and (IV) occlusion. Bottom portion highlights the cross section from the dotted line in the top portion of the image.

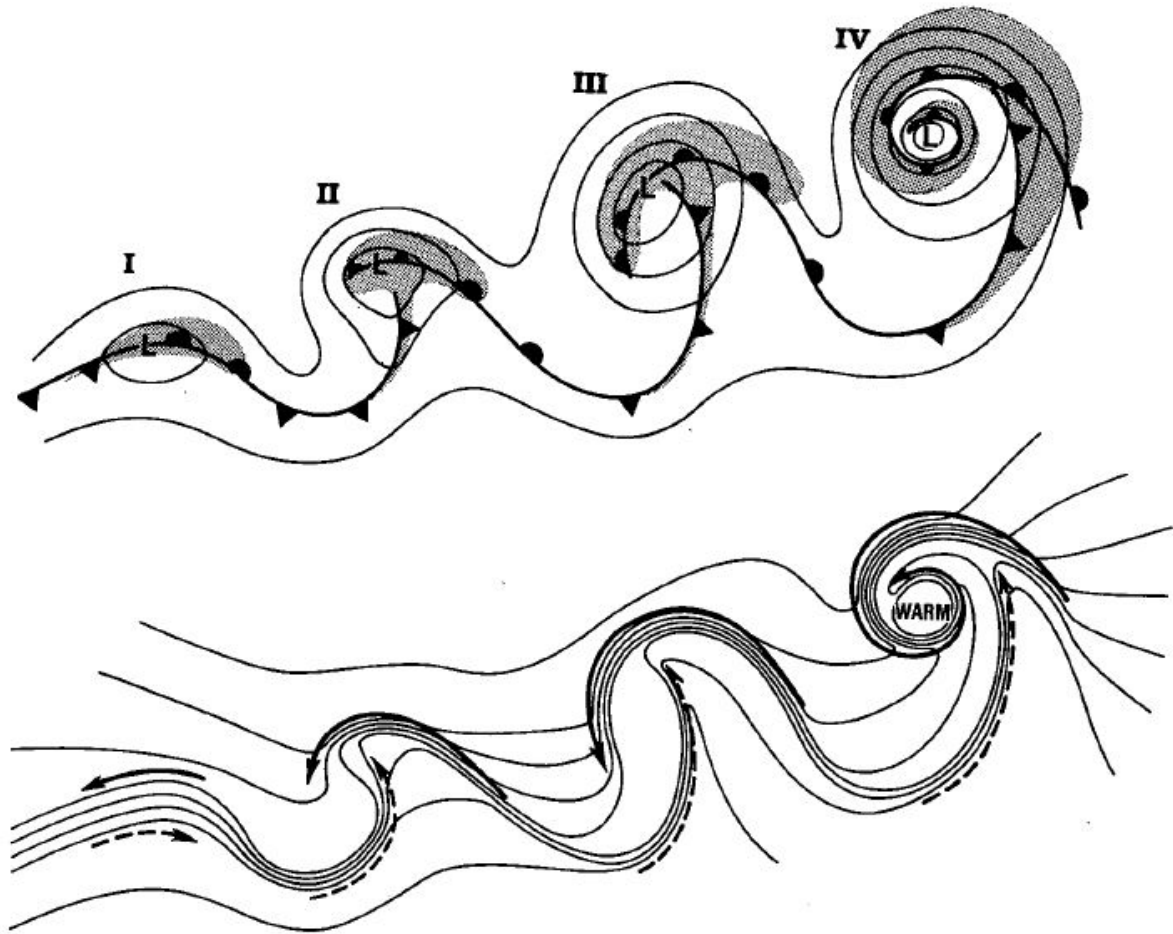


Figure 1.2: The Shapiro and Keyser Extratropical Cyclone Model (Shapiro and Keyser 1990). Top shows lower tropospheric geopotential height contours and frontal locations, gray areas highlight precipitation areas, while the bottom shows lower tropospheric potential temperatures, with cold on the north and warm on the south. Each step is as follows: (I) incipient frontal cyclone, (II) frontal fracture, (III) frontal T-bone and bent-back front, and (IV) frontal T-bone and warm seclusion.

Chapter 2: A-Train-Based Case Study of Stratiform–Convective Transition within a Warm Conveyor Belt

2.1 Introduction

Extratropical cyclones play a vital role in regulating Earth’s energy balance through poleward meridional transport of energy and through the effects of the clouds they produce within the climate system. Extratropical cyclones (ETCs) are an important source of fresh water in the midlatitudes, as they can produce most of the precipitation received in the planet’s temperate zones (Heideman and Fritsch 1988; Hawcroft et al. 2012), with up to 90% of the rainfall in storm track regions being produced by fronts associated with ETCs (Catto et al. 2012). The precipitation produced along the frontal regions originates in the planetary boundary layer (PBL) to the south and east of the cyclone center, and is transported by the poleward ascending warm conveyor belt airstream (Harrold 1973; Browning et al. 1973; Carlson 1980; Browning 1986; Wernli 1997; Eckhardt et al. 2004; Madonna et al. 2014).

Warm conveyor belts (WCBs) efficiently precipitate nearly all the moisture they transport, and make a substantial contribution to the total precipitation in the extratropics. They produce approximately half of the wintertime precipitation (Eckhardt et al. 2004; Field and Wood 2007), and are associated with more than 70% of extreme precipitation events in the southeast United States, eastern China, Japan, and South America (Pfahl et al. 2014). WCBs are more frequent in the winter seasons compared to summer in both hemispheres, have a stronger seasonal cycle in the Northern Hemisphere, and are particularly frequent in regions of intense baroclinicity and high

low-level moisture content (Stohl 2001; Eckhardt et al. 2004; Madonna et al. 2014). Given that WCBs mainly originate in the moist subtropical marine PBL between 20°-47° in the Northern Hemisphere (Wernli and Davies 1997; Madonna et al. 2014), they can transport large quantities of sensible and latent heat upward and poleward (Browning 1990). WCBs are crucial for the formation of mixed-phased clouds and precipitation within ETCs, along with cirrus clouds in their outflow (Browning 1990; Madonna et al. 2014). Moisture sources for WCBs are typically located over the ocean and close to their respective starting points, with their uptake of moisture often being associated with anomalies of latent heat flux due to a reduction of near-surface relative humidity and enhanced wind velocity (Neiman and Shapiro 1993; Pfahl et al. 2014). As air in the WCB progresses rapidly poleward during its ascent, the specific humidity decreases significantly as the water vapor condenses (Madonna et al. 2014), leading to the production of clouds and precipitation, which are strongly correlated to the amount of moisture transport by the WCB (Field and Wood 2007). While recent studies have been careful to define WCBs in terms of their origin and depth of ascent using parcel trajectories (e.g. Madonna et al. 2014), we characterize the WCB more generally as a poleward moving air stream within an ETC featuring large amounts of water vapor observed through precipitable water and cloud cover.

Numerous case studies have examined the dynamics of the flow through the WCB, as well as the effect of condensational heating in the WCB on cyclone strength and frontal structure. Several have examined the effect of latent heating on storm strength and structure (e.g., Reed et al. 1988; Kuo et al. 1991; Davis 1992; Whittaker and Davis 1994; Stoelinga 1996; Businger et al. 2005), while others have focused more specifically on fronts (Posselt and Martin 2004; Reeves and Lackmann 2004; Igel and van den Heever 2014) and the WCB itself (Boutle et al. 2011; Joos and Wernli 2012; Flaounas et al. 2015). While significant progress has been made in recent years,

there is much yet to examine regarding the interaction between cloud processes and the thermodynamic and dynamic structure of frontal zones, and how changes in cyclone circulation and environment are related to variations in the distribution and intensity of clouds and precipitation. To this end, this paper examines a long-lived WCB associated with a marine ETC that occurred in late November 2006, and the dynamics of its warm frontal zone. This cyclone formed east of the Florida coast as an upper level trough moved into the southeastern portion of the United States. For the next five days, the cyclone evolved similarly to the marine cyclone model proposed by Shapiro and Keyser (1990) and slowly travelled northeastward parallel to the United States, exhibiting a significant WCB. Once the cyclone matured, the cyclone center remained in relatively the same location for over 24 hours while the WCB advanced poleward ahead of the cyclone. As the WCB remained in approximately the same longitudinal location, it was sampled several times by NASA's Afternoon-Train (A-Train) satellite constellation.

The research presented here leverages a unique opportunity to conduct a multivariate analysis of the time evolution of the cloud structure and precipitation within a long-lived WCB, as most other studies have used composites of satellite observations to examine the connection between extratropical cyclone dynamics and cloud features (Evans et al. 1994; Lau and Crane 1995, 1997; Klein and Jacob 1999; Tselioudis et al. 2000; Tselioudis and Rossow 2006; Naud et al. 2006, 2010, 2012, 2014, 2015; Field and Wood 2007; Field et al. 2008; Posselt et al. 2008; Berry et al. 2011; Govekar et al. 2011, 2014; Bender et al. 2012). The instruments aboard the A-Train reveal a clear transition from stratiform to convective cloud structures during the evolution of the WCB, and examination of the coincident thermodynamic structure reveals a discernible transition from stable to unstable thermodynamic structure within the cyclone and its warm conveyor belt.

2.2 Data and Methods

This paper utilizes data from NASA's Earth Observing System Afternoon-Train (A-Train) Satellite Constellation, specifically from the Moderate Resolution Imaging Spectroradiometer (MODIS, Barnes et al. 1998), the Advanced Microwave Scanning Radiometer - Earth Observing System (AMSR-E, Kawanishi et al. 2003), and CloudSat (Stephens et al. 2002). AMSR-E and MODIS are located on the Aqua satellite, whose aim is to explore the global hydrological cycle and its role in the Earth's climate system (Parkinson 2003). The AMSR-E instrument is a conically scanning passive microwave radiometer with 6 horizontally- and vertically-polarized frequencies (6.925, 10.65, 18.7, 23.8, 36.5, and 89.0 GHz), observing water-related geophysical variables. Retrieval algorithms combine the brightness temperatures observed from the multiple dual-polarized channels to retrieve estimates of precipitation, integrated water vapor, and integrated cloud liquid water, along with other atmospheric and surface variables (Kawanishi et al. 2003).

MODIS has 36 channels that span the visible and infrared spectral bands, with wavelengths ranging from 0.4 to 14.5 μm . MODIS radiances can be used to retrieve cloud top properties (i.e. pressure and temperature), precipitable water, and temperature and water vapor profiles (Parkinson 2003). It can also retrieve aerosol optical depth and size distribution in the daytime, but these are limited in the presence of cloud cover and sun glint (King et al. 2003). Cloud optical thickness and effective radius is derived globally using 6 visible and near infrared bands at 1km spatial resolution (King et al. 2003; Parkinson 2003). Of all of the instruments onboard the Aqua satellite, MODIS has the finest spatial resolution, ranging from 250m in the visible to 500m in the shortwave infrared and 1 km in the thermal infrared (Parkinson 2003; Kawanishi et al. 2003).

The CloudSat mission is designed to produce a global survey of clouds, and to quantitatively evaluate their representation in global atmospheric circulation models. CloudSat

provides a rich source of information for evaluating cloud properties derived from other satellite data, such as those observed by the instruments onboard Aqua. CloudSat is by nature limited in its ability to observe the horizontal extent of clouds since it is a non-scanning nadir-pointing instrument. Nevertheless, as the first 94 GHz space borne cloud profiling radar (CPR), CloudSat is designed to measure vertical structure of clouds and precipitation from space, stimulate important research on clouds and precipitation, and provide a demonstration of 94 GHz space borne technology (Stephens et al. 2002). The relatively high frequency was chosen to optimize cloud detection, at the expense of attenuation in moderate to heavy precipitation. Radar measurements along CloudSat's track are averaged at 0.32s time intervals, which provides cloud and precipitation information over a 1.4 km elliptical footprint with 500 m vertical range gates that are oversampled to give an effective vertical resolution of 250 m between the surface and 30km in altitude (Stephens et al. 2002, 2008). Thermodynamic (temperature and water vapor) fields along the CloudSat track are obtained from the European Centre for Medium-Range Weather Forecasts (ECMWF) operational analysis, which were interpolated in space and time to the CloudSat track at a 0.5° resolution (termed the ECMWF-AUX dataset in the set of CloudSat data products; Posselt et al. 2008).

Three-dimensional wind, temperature, and water vapor fields are obtained from the National Oceanic and Atmospheric Administration (NOAA) National Center for Environmental Prediction (NCEP) Global Forecast System (GFS) analysis on a 1.0 x 1.0 degree grid. Data was obtained from the NOAA National Operational Model Archive & Distribution System (NOMADS; <http://nomads.ncdc.noaa.gov/>). We identify the location of the WCB using vertically integrated water vapor content (precipitable water vapor) and winds in the lower free troposphere. The WCB in our case is defined to be an airstream that is rooted in the tropics and proceeds

poleward, curving cyclonically and anticyclonically as it ascends east of the cyclone center. While all clouds observed in the MODIS, AMSR-E, and CloudSat data ultimately result from rising motion produced by the cyclone, we note that a portion of the cloud shield in frontal zones and around the cyclone center was likely not produced by trajectories that satisfy the Lagrangian criterion used to define WCBs (e.g., as defined via detailed trajectory analysis by Madonna et al., 2014).

2.3 Synoptic Overview

During 20-21 November 2006, a deep upper-tropospheric trough moved into the southeastern United States, and by 1800 UTC 21 November, a weak region of relatively low surface pressure (1008 hPa) associated with the upper-level trough had formed over the western Atlantic Ocean east of South Carolina (Figures 2.1a & 2.1g). East of the newly formed cyclone, southerly winds began to advect water vapor northward from the tropics, as can be seen in the observed precipitable water overlaid with the 700 hPa wind field (Figure 2.1d). As the WCB formed on the 21 November, two outflow branches were observed, curving cyclonically and anticyclonically away from northward edge of the WCB (Figure 2.1d-2.1e) (Martinez-Alvarado et al. 2013). Strong water vapor flux convergence is indicated in the region that stretched from Cape Hatteras, North Carolina to the northeast. The northern boundary of the WCB is approximately marked by the 40 mm precipitable water contour, which extended along the low-level warm front at this time. Over the subsequent 24 hours, the surface low pressure center remained nearly stationary (Figures 2.1g-2.1j) while the northernmost extent of the WCB migrated slowly poleward (Figures 2.1d-2.1f). The low pressure center at upper levels also moved poleward, and by 23 November the upper and lower tropospheric low pressure centers were collocated (Figures 2.1a-

2.1c, 2.2a, 2.2d, and 2.2g.). Precipitable water values in the WCB south of the warm front remained consistently high, exceeding 55 mm to the east of the surface low pressure center.

As the WCB progressed poleward during 22-24 November, the southerly winds increased in magnitude, exceeding 40 knots within the WCB at the 700 hPa level (Figure 2.2d). Clear evidence of a decrease in the cyclonically curving branch of the WCB is evident in Figures 2.2d – 2.2f. Spatial separation between the cyclone center and the anticyclonically curving branch of the WCB led to seclusion of a region of relatively high water vapor near the cyclone center. In addition to the anticyclonic curvature in the WCB, the low level anti-cyclonic circulation east of the parent low caused the WCB to narrow as it approached the cyclone (Figures 2.2e-2.2f). Recent work has highlighted the role of latent heat release in the WCB in amplifying the downstream ridge (Pomroy and Thorpe 2000; Massacand et al. 2001; Grams et al. 2011; Schemm et al. 2013; Chagnon et al. 2013). In this case, the upper level flow above the northern edge of the WCB developed a shortwave ridge within the amplified downstream jet starting on 23 November, which was also visible at the 700 hPa level (Figures 2.2a-2.2f). After 0000 UTC on the 24 November, as the WCB narrowed, the upper level low acquired a positive tilt and began to merge with the northern branch of the jet stream, and the surface low rapidly propagated northeastward (Figure 2.2c). By the 25 November, the cyclone center had moved over the western Atlantic Ocean, and the WCB had weakened and thinned, no longer advecting large amounts of water vapor northward from the tropics (not pictured).

2.4 Analysis of A-Train Products

2.4.1 2D Overview

At 1800 UTC 21 November, the surface low pressure system was still developing (Fig. 2.1), and MODIS cloud top pressures depicted upper level clouds that were primarily linear and aligned from the southwest to the northeast along the lower-tropospheric baroclinic zone (Figure 2.3a). The nascent cyclonically turning WCB airstream can be seen in the high clouds observed by MODIS over the eastern Carolinas at this time as well. Examination of the surface precipitation reports over the United States, along with retrieved rainfall from AMSR-E, indicated that moderate precipitation of around 5 mm/hour was being produced in the northwest quadrant of the storm.

Cyclonic and anticyclonic curvature in the WCB can be seen in the retrieved precipitable water at 0600 UTC 22 November (Figure 2.4a); however, the bulk of the integrated cloud water and precipitation were located in the cyclonically curving portion of the flow (Figures 2.4b and 2.4c). Cloud top pressure from MODIS reflects the transport of water primarily northward and westward at this time, as clouds along the eastern side of the warm front were not as geographically extensive (Figure 2.3b). Along the leading edge of the WCB near the approximate location of the warm front, cloud liquid water values exceeded 1.5 mm (Figure 2.4b) with over 70 mm of water vapor present in the same region (Figure 2.4a), and rain rates were estimated to be over 8 mm/hour (Figure 2.4c). Between 0600 UTC & 1800 UTC 22 November, the primary cloud shield moved to the north and east of the cyclone center (Figure 2.3c), consistent with the development of the low level trough in the region at this time (Figures 2.2c, 2.2f, 2.2j). There was a significant decrease in water vapor, cloud liquid water, and rain rate directly north of the cyclone center (Figures 2.4e & 2.4f), as the bulk of the water vapor transport had shifted to the east and into the anticyclonically curving portion of the warm conveyor belt (Figure 2.2f).

Throughout 23 November, MODIS imagery showed the primary cloud shield to be located east of the surface low (Figures 2.2g & 2.2h) at the northern edge of the WCB, and it remained remarkably stationary from 1800 UTC 22 November through 1800 UTC 23 November (Figures 2.3c-2.3e). At the same time, a break in the cloud cover was observed directly north of the cyclone center (Figures 2.3d-2.3e) as the cyclonic branch of the WCB became separated from the anticyclonic branch, as discussed in the Synoptic Overview (Figure 2.2d). By comparing Figures 2.2e and 2.3e, we notice that most of the cloud cover coincidentally remained concentrated over the location of the warm conveyor belt, with less cloud cover remaining over the east coast of the United States, northwest of the cyclone center (Fig. 2.3e). The orbit of the A-Train, combined with the more limited spatial extent of the AMSR-E swath, led to a gap in retrievals of cloud and precipitation over the cyclone center during 23 November. The next overpass of the storm center occurred at approximately 0600 UTC 24 November, and revealed a significant change in the character of the water vapor, cloud, and rain distribution (Figs. 2.4g – 2.4j). The distribution of water vapor became more spatially non-uniform compared to the observations on the 22 November, and the AMSR-E retrievals indicated pockets of high cloud liquid water and rain rate (Figs 2.4h - 2.4j). This is an indication of a transition in the nature of the cloud structure and precipitation processes within the warm front.

2.4.2 Vertical Structure

Examination of the cloud horizontal extent, integrated cloud liquid water, and rain rate provide some indication of the hydrological features within the storm. However, details of the microphysical influence on the thermodynamic structure and the vertical condensate distribution cannot be obtained using 2D and vertically integrated observations. CloudSat is capable of

observing the internal structure of clouds (Stephens et al. 2002), and in this case, it intersected the WCB and the warm front multiple times as the WCB remained in nearly the same longitudinal location for a few days. The observations closest to the cyclone center were obtained at approximately 0600 and 1800 UTC 22 November and 0600 UTC 24 November. Both observations on 22 November correspond to times during which the precipitation and cloud liquid water distributions at the intersection between warm and cold fronts were relatively uniform in extent and modest in magnitude, while the cloud content and precipitation were more spatially non-uniform on 24 November, as was previously shown in the results from AMSR-E (Figure 2.4).

Examination of the CloudSat profiles of reflectivity, combined with equivalent potential temperature (θ_e) computed from ECMWF temperature and water vapor interpolated to the CloudSat track, are depicted in Figure 2.5. At 0600 UTC on 22 November, CloudSat observed cold-frontal convective clouds south of 35°N, while to the north it intersected the warm frontal clouds located within the northern end of the WCB airstream (Figure 2.5a). θ_e profiles within this cross-section depict the effect of evaporating precipitation at low levels: θ_e is nearly constant from the surface to approximately 2 km in the region just north of the surface warm front. The frontal region itself can be seen in the moist isentropes slope from near the surface at 36°N to a height of nearly 10 km near 43°N. The largely stratiform nature of the cloud in the warm frontal region is reflected in the high degree of spatial continuity in the radar reflectivity (and by extension, the cloud content) north of 36°N. Retrieved precipitation rates at this time were relatively low (less than 10 mm/hour), with a single region near 37°N where the rain rate was large enough to cause full attenuation of the CloudSat signal.

At 1800 UTC, CloudSat again intersected the northern portion of the WCB, but, in contrast to the 0600 UTC overpass, did not observe the cold-frontal convection. Stratiform cloud and

precipitation in advance of the surface warm front (between 36°N-39°N) was far more extensive at this time than at 0600 UTC, and the cloud features along and above the frontal zone itself were still quite uniform (Figure 2.5b). The vertical gradient of θ_e in the frontal zone had increased in magnitude, and the region of constant θ_e associated with evaporating hydrometeors was confined to the lowest 1-2 km. An increase in cloud content within the frontal zone relative to 0600 UTC can be inferred from the increase in reflectivity values, which were greater than 15 dBZe through a large portion of the frontal zone, with some values under 5,000 meters likely underestimated due to attenuation. Precipitation rates at this time were nearly uniformly larger than at 0600 UTC with a large portion of the frontal region producing precipitation rates large enough that the CloudSat reflectivity signal was fully attenuated at the surface.

In the 36 hours between 1800 UTC 22 November and 0600 UTC 24 November, a significant change occurred in the thermodynamic and cloud structures within the warm frontal zone. We see the result of this transition in the CloudSat observations at 0600 UTC on 24 November, as it again passed near the cyclone center in a trajectory very similar to the overpass at 0600 UTC on 22 November. CloudSat again intersected convection along the cold front (south of 41°N), though the convection appears to be more intense than at earlier times, with larger reflectivity values and indication of full radar attenuation below 2 km above the surface (Figure 2.5c). The surface warm front is still clearly evident at and north of 41°N, and the vertical gradient of θ_e in the lowest levels of the troposphere remains relatively large; however, the cloud fields and thermodynamic structure above the low-level frontal zone are significantly different. The reflectivity structure exhibits a high degree of variability in both the vertical and horizontal at this time, as the cloud structures have become more convective and isolated. The presence of convection is borne out in the vertical structure of the θ_e field, the vertical gradients of which have

become much weaker above the frontal zone. In some regions, θ_e is nearly constant with height, indicating the presence of saturated vertical mixing. This can be seen in the shallow precipitating region between approximately 40°N and 41°N, and is especially evident between 41.5°N and 43.5°N at levels between 2-4 km. This layer is known to be characterized by strong latent heating, primarily due to the conversion between vapor and liquid (Joos and Wernli 2012). Also of note is the shallow-topped elevated-base convective features between 44°N and 46°N. These extend no higher than 7 km above the surface, are upright, have bases above 2 km, and are not producing precipitation at the surface. The origin of these features is not clear, and their properties beg further study with a numerical process model. It is notable that the significant differences in cloud vertical structure seen in the CloudSat radar reflectivity are not reflected in the MODIS cloud top pressure field (Fig. 3f).

Overall, in contrast to the reflectivity structures observed in the warm frontal region on 22 November, more individual and narrow cloud structures were observed on 24 November than deep and wide cloud structures. Precipitation retrievals indicate the signal was fully attenuated over a smaller range of latitudes, with regions containing large precipitation rates corresponding generally to regions characterized with weak vertical gradients of θ_e . Comparison between Figures 2.5b and 2.5c indicates the heavy precipitation at 1800 UTC 22 November was stratiform in nature, while precipitation at 0600 UTC 24 November was convective.

2.4.3 AMSR-E 89 GHz Scattering Index

Horizontal context for CloudSat's nadir pointing curtain observations may be obtained via the examination of the ice scattering signatures in higher frequency AMSR-E microwave channels. Relative to clear air and cloudy regions containing primarily liquid cloud particles, ice scattering

typically appears as a vertically polarized brightness temperature (TB89V) reduction due to volumetric scattering of microwave radiation by precipitation sized frozen hydrometeors (e.g., Spencer et al. 1989; Petty 1994; Weng and Grody 2000; Bennartz and Petty 2001; Kulie et al. 2010). In addition, ice scattering introduces differences in vertically – horizontally polarized brightness temperatures (TB89V-H), as well as the 89 GHz scattering index (S89; Petty 1994). The S89 linearly combines vertical and horizontal polarization brightness temperature observations with similar values (observed or modeled) in cloud-free regions of the nearby environment. It does so by calculating the brightness temperature reduction due to ice scattering as compared to a non-scattering atmosphere that returns the same polarization difference. In theory, S89 values in non-precipitating clouds do not typically exceed about 10 K, with significant scattering associated with S89 values larger than ~ 10 K (Petty 1994; Bennartz and Petty 2001). As such, elevated S89 values serve as valuable proxies for the column-integrated ice content. Elevated S89 values are also usually associated with higher surface precipitation rates; however, this relationship is complicated by variability in ice particle shape, size, and distribution that varies with precipitation type (Bennartz and Petty 2001; Bennartz and Bauer 2003).

Compared with the surrounding environment, clouds in the WCB exhibit TB89V reductions (Figures 2.6a, 2.6d, and 2.6g) on the order of ~ 30 – 60 K, and are closely associated with regions of surface precipitation shown earlier in Figures 2.4c, 2.4f, and 2.4j. Decreased TB89V values to the north of the WCB on 22 November (Figures 2.6a and 2.6d), and to the north/northwest of the WCB on 24 November (Figure 2.6g), are due to lower water vapor amounts and relatively clear skies, under which conditions ocean surface signatures may propagate through to the top of the atmosphere. The ocean surface signature can be clearly seen in the TB89V-H (Figures 2.6b, 2.6e, and 2.6h), where polarization differences larger than 50 K are indicative of the

highly polarized ocean surface signal. In contrast, reduced TB89V-H values in cloudy regions correspond to significant ice cloud content and perhaps surface precipitation in the WCB and attendant fronts.

Despite the complicated relationship with surface precipitation rate, the S89 figures for the 22 and 24 November WCB event effectively illustrate the extent and evolution of the frozen cloud shield associated with the WCB, and grossly display a similar trend as is observed in the CloudSat reflectivity profiles. Maximum S89 values routinely exceed 30K in the warm frontal region for all three overpasses, indicating significant scattering throughout the evolution of the WCB. The region over which the S89 field exceeds 10 K is rather expansive and slightly more homogeneous in the 22 November overpasses (Figures 2.6c and 2.6f) compared to the narrower and more convective scene observed on the 24 November overpass (Figure 2.6i). Note also the enhanced S89 values on 24 November between 40 and 45 N near the eastern United States coast in the region of the occlusion.

Figure 2.7 illustrates S89 relative frequency of occurrence (histogram) statistics for the three AMSR-E WCB overpasses. In generating this plot, we restricted our analysis to pixels for which S89 values exceeded 10 K, and with AMSR-E surface precipitation rate retrievals greater than 2 mm h^{-1} . As previously noted, significant S89 values associated with the WCB are observed on all three AMSR-E overpasses; however, changes in S89 histograms indicate subtle ice microphysical differences (e.g. ice particle size, shape, and/or distribution) between the various WCB phases. For instance, the S89 histogram peak shifts from ~ 20 to ~ 30 K between the first (solid) and second (dashed) 22 November AMSR-E overpasses. While the peak S89 value shifts significantly, note that the first overpass contains a larger percentage of S89 occurrences exceeding ~ 45 K compared to the second overpass. The maximum S89 value for both of the 22 November

overpasses is ~ 75 K. The 24 November (dash-dot) AMSR-E overpass S89 histogram peak (~ 20 K) is similar to the first 22 November overpass. Note, however, the markedly larger fraction of extremely high S89 values (> 45 K) compared to the earlier overpass times. This tangible increase in the fraction of intensive scattering events is indicative of systematically larger ice particles associated with the more convectively active 24 November WCB phase. The systematic scattering changes depicted in Figure 2.7 reflect the evolving ice microphysical composition of the cloud structures associated with the WCB.

2.5 Implications for Satellite Storm Sampling Frequency

Our analysis of this case study highlights several known benefits of repeated temporal sampling with multiple diverse remote sensing instruments. Specifically, observations of the warm frontal portion of the storm in approximately the same storm-relative location at multiple times revealed a distinct transition from stratiform to convective cloud structures. Collocated analysis of the thermodynamic environment provides the context for the observed cloud features, and confirms the presence of reduced static stability in regions with cloud features that appear convective. The fact that significant changes in the vertical cloud structure were observed in the CloudSat radar reflectivity and were not detectable in the passive infrared observations from MODIS, is indicative of the need for both active and passive observations of clouds in ETCs. However, repeated observations of the same storm-relative frontal position with active remote sensing instruments are rare. When CloudSat ground tracks were compared with cyclone locations in a database containing all extratropical cyclones that have occurred since the 2007 calendar year, it was found that 50% of the time CloudSat passed within 200 km of the cyclone center only once during the evolution of the storm. In 25% of the cyclone cases, there were no CloudSat overpasses

within 200 km of the storm center at all. The implication is that it is difficult to use CloudSat to examine, in a systematic fashion, the time evolution of frontal clouds in an extratropical system. Such an analysis is more straightforward over land in the continental United States and Europe, where there is ample coverage from ground based radar. However, operational radar systems are optimized for rain, and may not detect the subtle transitions in cloud structure that higher frequency radars, like CloudSat, can observe.

The current A-Train constellation and CloudSat frequency of frontal intersect has enabled a robust series of composite analysis (Naud et al. 2010; 2012; 2014; 2015); however, composites tend to smear out some of the details observed in individual case studies like ours, and an exploration of the cloud-scale processes that occur in and around mid-latitude cyclones will require measurements with a much higher temporal frequency. While instruments aboard current geostationary satellites can provide frequent observations, they are limited to passive visible and infrared channels, which can only observe cloud top properties similar to what we observed with MODIS in this case study. As noted above, visible and infrared observations are not capable of detecting changes in internal cloud structure. Sequential active microwave observations are not feasible using large platforms in polar orbit, and it is possible that a new paradigm (e.g., constellations of small satellites flying in formation) may be required. Such observing systems are currently in active development, and are being pioneered in the Cyclone Global Navigation Satellite System (CYGNSS) mission (Ruf et al., 2016). We also wish to point out that any conclusions we may draw about physical processes, even with repeated observations of the same storm-relative location, are circumstantial without quantitative estimates of latent heating rates and vertical motion. As such, it is our assertion that a critical need from future observing systems will be either direct estimates of vertical motion (i.e. from measurements of the Doppler spectrum) or

indirect estimates made using high temporal frequency observations of the cloud fields themselves (e.g. rapid temporal samples of the cloud radar reflectivity).

2.6 Summary and Conclusions

Cloud processes in extratropical cyclones are known to exert an influence on storm dynamics and frontal structure. While the overall synoptic dynamics of marine extratropical cyclones have been well understood for decades (e.g., Shapiro and Keyser 1990), recent studies have begun to explore cloud processes and mesoscale frontal evolution occurring in ETCs and their warm conveyor belts. In particular, Flaounas et al. (2015) observed two ETCs in the Mediterranean region during the HyMeX field campaign, one of which produced embedded convection that developed within the WCB. Unlike our case, the storm analyzed by Flaounas et al. (2015) exhibited convection that occurred south and west of the cyclone center. Other recent case studies from various field campaigns have examined the microphysical processes within ETCs and their impact on frontal evolution (Crosier et al. 2014; Dearden et al 2014, 2016; Lloyd et al. 2014; Vaughan et al 2015). Unlike our case, most of these studies have focused on cold frontal evolution, which exhibits different dynamics than a marine warm front. Using a late November 2006 case that was observed multiple times by various instruments aboard the polar orbiting A-Train satellite constellation, we were able to detect a significant transition in the mesoscale characteristics and distributions of clouds and precipitation within the warm frontal region at the poleward end of the warm conveyor belt. This transition was clearly visible in subsequent CloudSat overpasses of the warm front, but was not visible in passive infrared imagery.

While cloud top observations showed that the cloud shield produced by the anticyclonically curving portion of the WCB remained quite uniform throughout the WCB's evolution,

observations from AMSR-E (Figures 2.4, 2.6, and 2.7) and CloudSat (Figure 2.5) indicate a transition was occurring below the cloud top. The distribution of water vapor and cloud liquid water in the warm frontal zone were more spatially uniform on 22 November. Between 22 and 24 November, the cloud content became increasingly concentrated in small regions with greater intensity as the cyclone evolved. Cloud water and rain rates were no longer strongest at the warm front, but rather spread out throughout the WCB in intermittent pockets of convection. Details of the vertical structure in these convective regions were captured in the CloudSat radar reflectivity profiles and associated ECMWF data, which showed that the thermodynamic structure within the WCB had become more convective and unstable (Figure 2.5c) compared to the thermal stratification observed along the leading edge of the conveyor belt on the 22 November (Figures 2.5a-2.5b). Examination of the high frequency scattering signature from AMSR-E (Figures 2.6 and 2.7) confirmed an increase in the highest ice scattering values over this time period.

Taken together, the results lead us to conclude that a mesoscale stratiform to convective transition occurred within this extratropical cyclone. Summarizing what we observe of the stratiform - convective transition in this case, we note the following. The transition happens later in the cyclone life cycle, and is characterized by shallow convection rooted in the warm frontal zone, with destabilization evident in the lower troposphere. The 89 GHz scattering index indicates an increase in the amount of ice hydrometeors aloft in the region of the warm front and in the occluded sector, reflecting the transport of water from the lower to the upper troposphere. Taken together, the results indicate a possible increase in the lower-tropospheric latent heating maximum in the warm frontal region. As was shown in Posselt and Martin (2004), positive diabatic heating in the mid-troposphere is associated with PV redistribution; creating a reduced upper tropospheric PV anomaly and a positive anomaly in the lower troposphere (Methven 2015). The warm frontal

region in which we observe the transition from stratiform to convection is displaced to the east of the cyclone center, and it is unlikely that the latent heating induced positive PV anomaly is contributing directly to the strength of the cyclone vorticity maximum. However, we do note that the surface pressure minimum expands to the east with time while the sea level pressure minimum remains nearly stationary (Figures 2.1 and 2.2). In this case, the influence of the stratiform - convective transition appears to be twofold; extending the low-level trough toward the north and east, and perhaps also restricting the eastward movement of the upper-tropospheric wave via creation of a reduced upper-tropospheric PV anomaly. It is also possible that the lower tropospheric positive PV created via latent heat release may be advected into the region of the cyclone center, enhancing the cyclone circulation (e.g., Schemm and Wernli, 2013). Further exploration of the specific mechanisms will require numerical simulation (e.g., as in Posselt and Martin 2004; Schemm et al. 2013; Schemm and Wernli 2014).

It is difficult to determine how or why this transition occurred without use of numerical simulation. However, we may speculate from the fact that the weak θ_e gradient was located just above the warm frontal surface, that destabilization was likely caused by lower-tropospheric processes rather than cold air advection at upper levels. The source regions for the water vapor transported poleward in the WCB remained consistent throughout its evolution, while relatively cold and dry continental air was ingested into the storm at low levels from the north and west. Sustained latent heating within the warm frontal region or the surface sensible and latent heat fluxes north and west of the cyclone center could have played a role in the convective transition. Previous research has shown that extreme marine cyclogenesis can occur in the winter seasons east of continental land masses with large sea surface temperature gradients in the immediate vicinity (Sanders and Gyakum 1980). Extreme thermodynamic air-sea differences can increase

the baroclinicity and instability within the boundary layer (Cione et al. 1993; Vukovich et al. 1991), leading to large surface fluxes of latent and sensible heat release (Neiman and Shapiro 1993). Given that latent and sensible surface fluxes are primarily driven by large air-sea thermodynamic differences along with strong surface winds, both of which are featured in ETCs like the one presented in this case study, we hypothesize that these surface fluxes contributed to the convective evolution of the warm front and will be the main focus in future work. It is not clear how often such a transition happens in the warm frontal region of oceanic (or continental) cyclones. We are currently conducting composite studies of extratropical frontal structure (e.g., Naud et al. 2012; 2015), but as mentioned above composites have a tendency to obscure the details of frontal cloud horizontal and vertical structure. It is possible that recent and near future field campaigns (e.g., HyMeX; www.hymex.org or NAWDEX; www.nawdex.org) may help to shed light on the prevalence of convection in warm frontal regions. Numerical modeling studies have indicated large values of latent heating in the WCB in mature oceanic cyclones (e.g., Posselt and Martin 2004; Joos and Wernli, 2012). However, given the lack of in-situ or remote surface observations within this cyclone, it is not possible to conclude at this time how either surface fluxes or elevated latent heating could have affected this cyclone. Numerical modeling studies are perhaps best suited for a process-based study, and we leave such an analysis for future work.

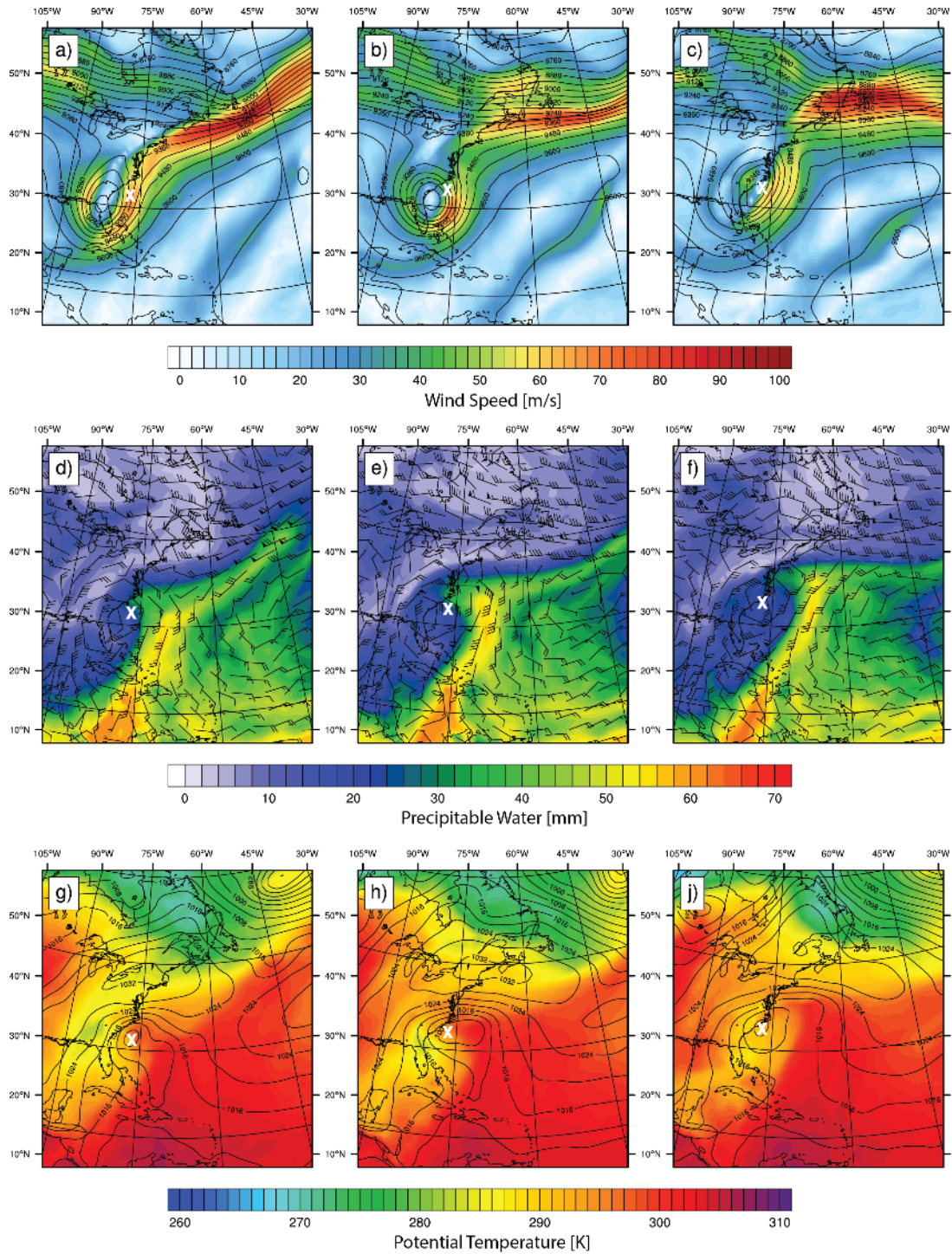


Figure 2.1: GFS Analysis for 1800 UTZ 21 Nov (a, d, g), 0600 UTC 22 Nov (b, e, h), and 1800 UTC 22 Nov (c, f, j). Row a-c: 300 hPa geopotential heights (m, black contours) and wind speed (m/s, colored). Row d-f: 700 hPa wind (knots, wind barbs) and total column precipitable water (mm, colored). Row g-j: 850 hPa Potential Temperature (K, colored) and sea level pressure (hPa, black contours). X marks the approximate location of the surface low center.

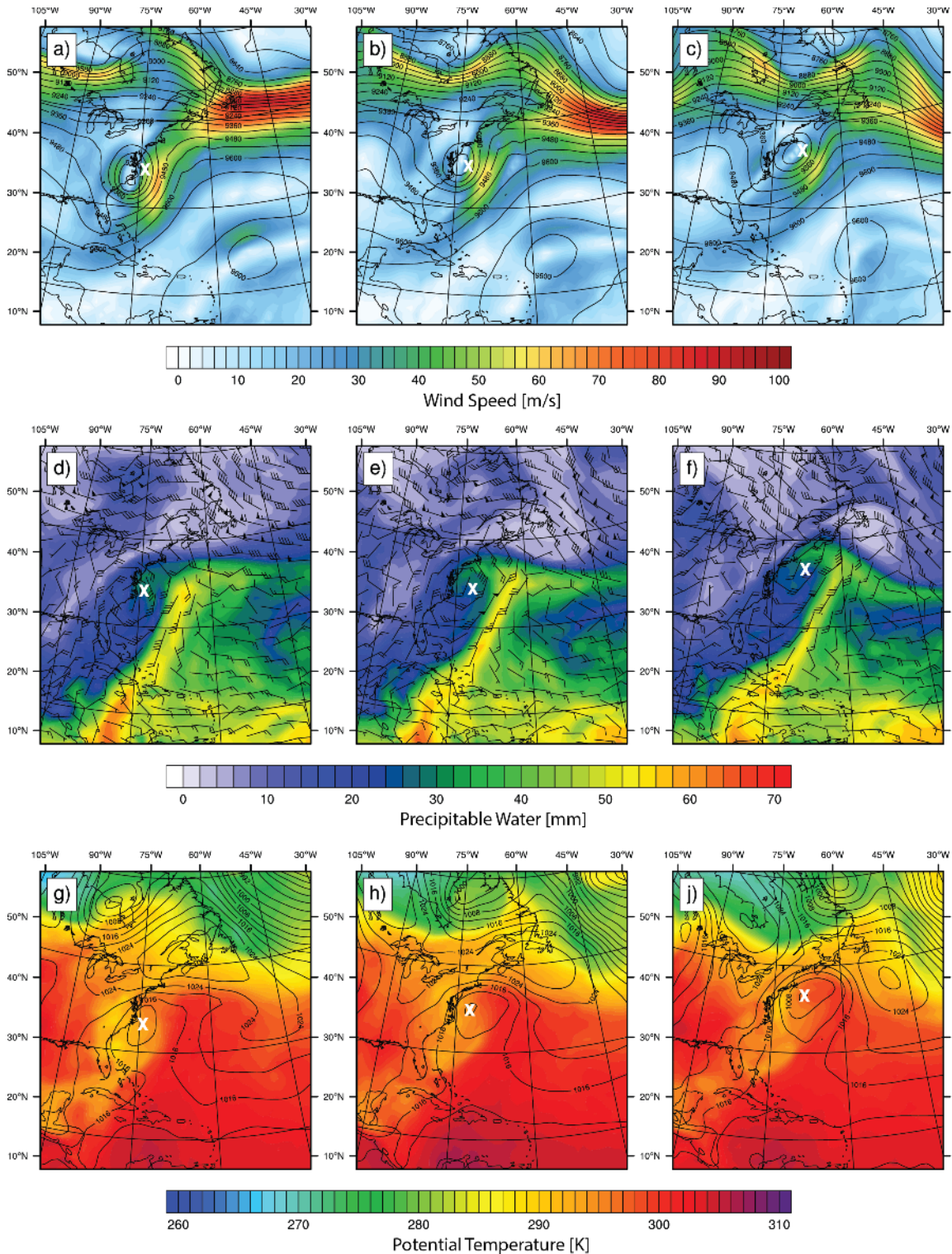


Figure 2.2: GFS Analysis for 0600 UTZ 23 Nov (a, d, g), 1800 UTC 23 Nov (b, e, h), and 0600 UTC 24 Nov (c, f, j). Row a-c: 300 hPa geopotential heights (m, black contours) and wind speed (m/s, colored). Row d-f: 700 hPa wind (knots, wind barbs) and total column precipitable water (mm, colored). Row g-j: 850 hPa Potential Temperature (K, colored) and sea level pressure (hPa, black contours). X marks the approximate location of the surface low center.

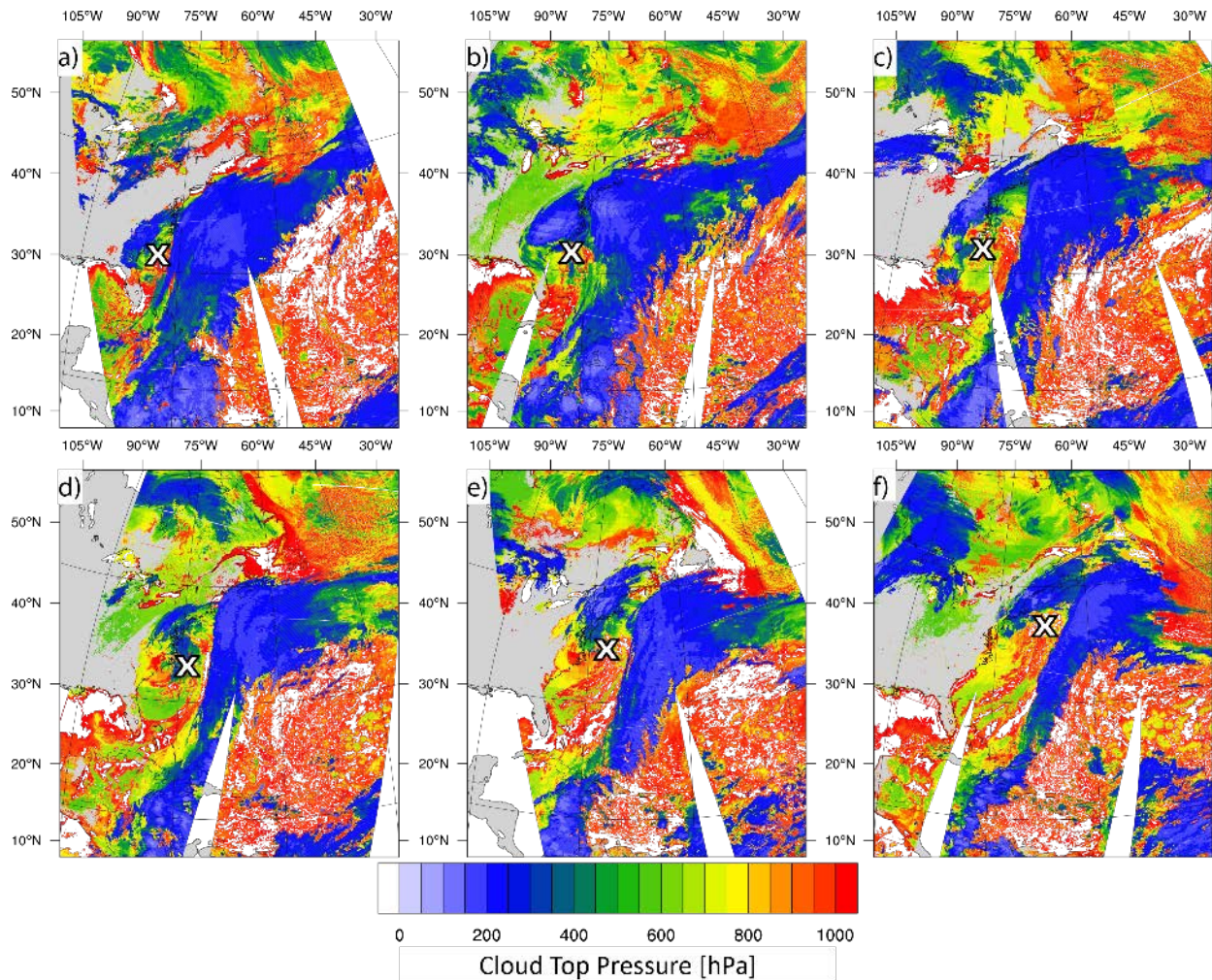


Figure 2.3: MODIS observed cloud top pressure (units: hPa) around approximately a) 1800 UTC 21 Nov, b) 0600 UTC 22 Nov, c) 1800 UTC 22 Nov, d) 0600 UTC 23 Nov, e) 1800 UTC 23 Nov, and f) 0600 UTC 24 Nov. The white regions indicate missing data. X marks the approximate location of the surface low center.

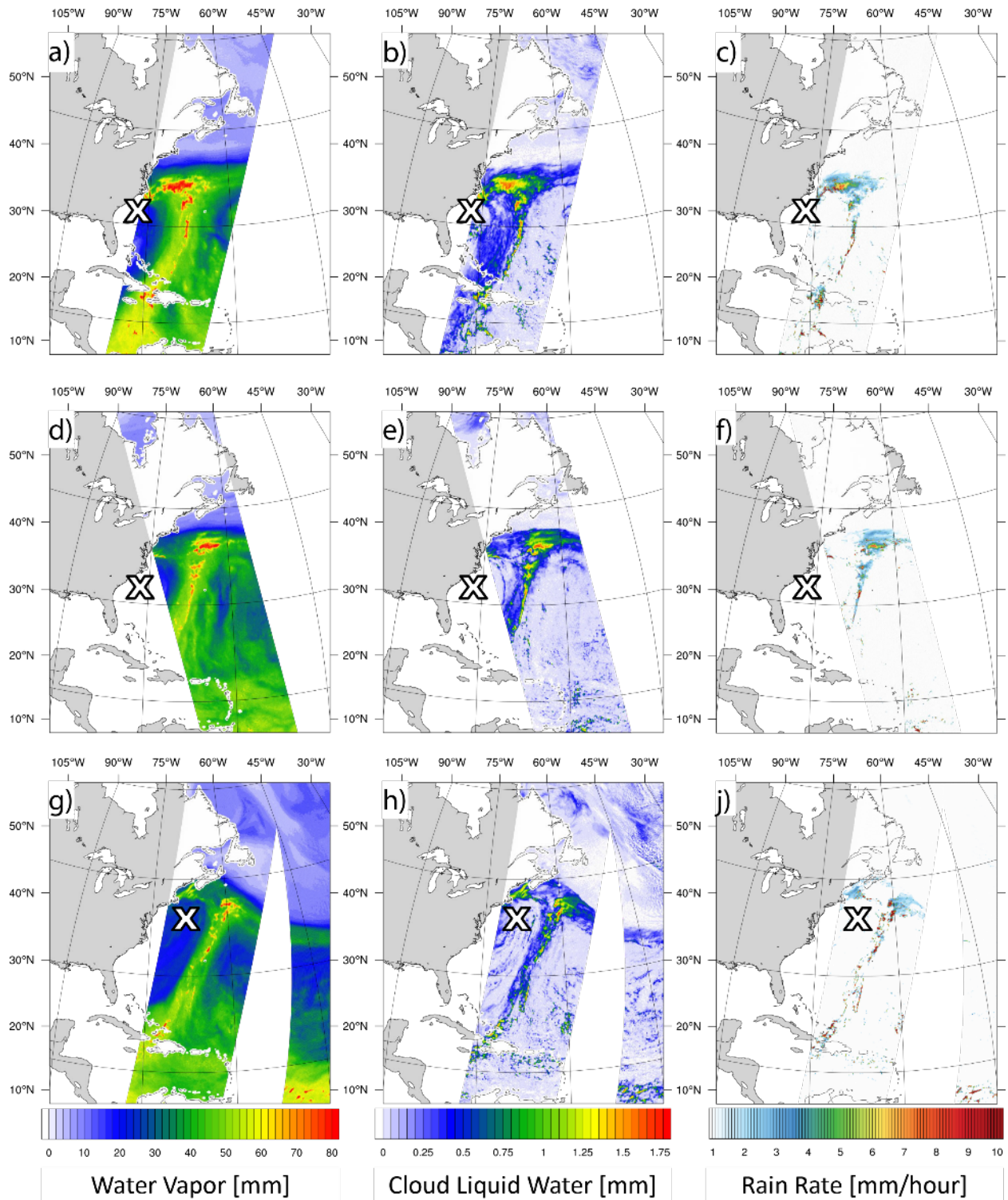


Figure 2.4: AMSR-E observed water vapor (a, d, g; Units: mm), cloud liquid water (b, e, h; Units: mm), and rain rate (c, f, j; Units: mm/hour) at approximately 0600 UTC 22 Nov (a-c), 1800 UTC 22 Nov (d-f), and 0600 UTC 24 Nov (g-j). X marks the approximate location of the surface low center.

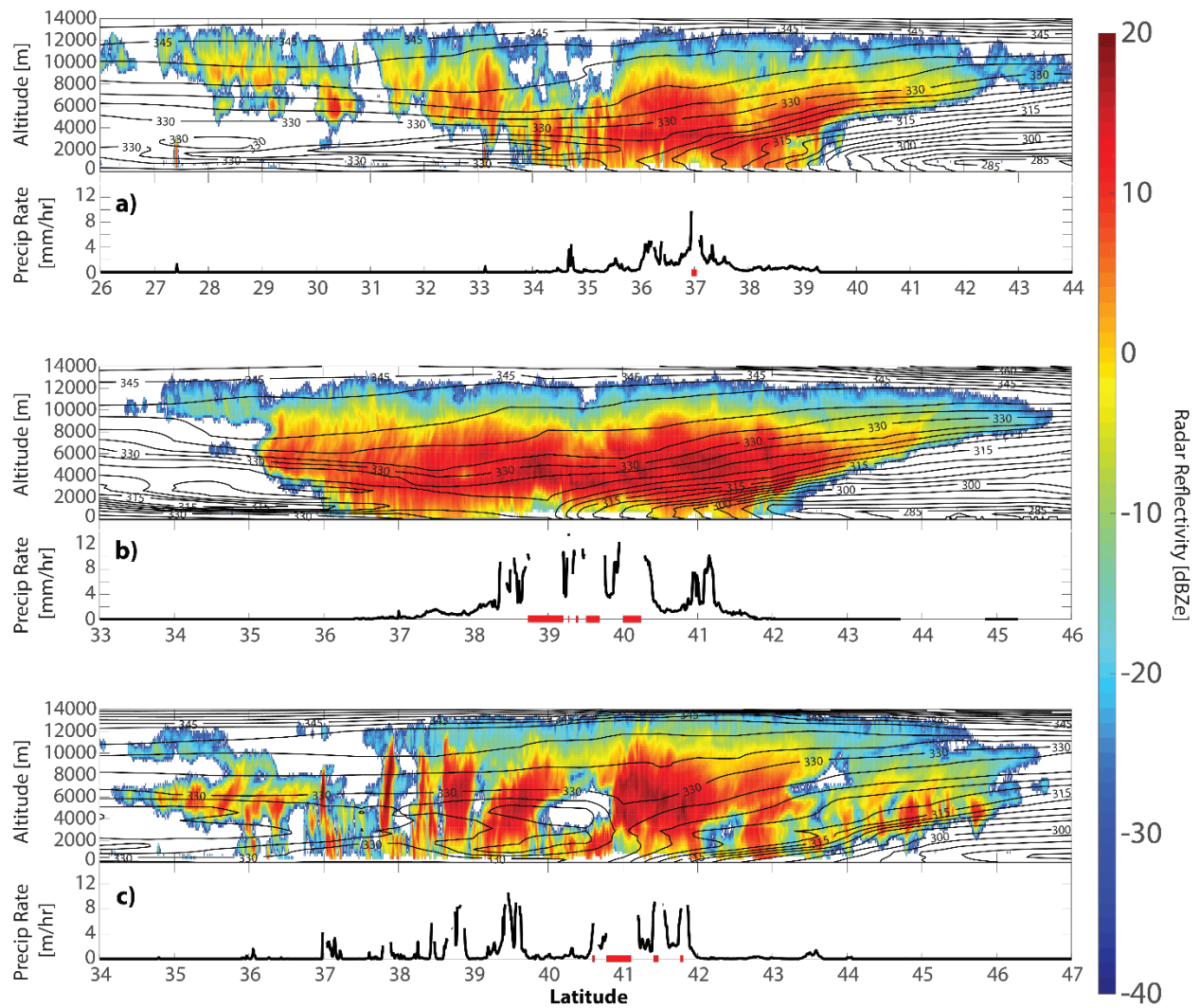


Figure 2.5: CloudSat Radar Reflectivity (dBZe) with Equivalent Potential Temperature (K, contours) and precipitation rate (black line plot, red values indicate missing data) at approximately a) 0600 UTC 22 Nov, b) 1800 UTC 22 Nov, and c) 0600 UTC 24 Nov 2006. Equivalent potential temperature is computed from ECMWF temperature and water vapor mixing ratio fields interpolated to the CloudSat track.

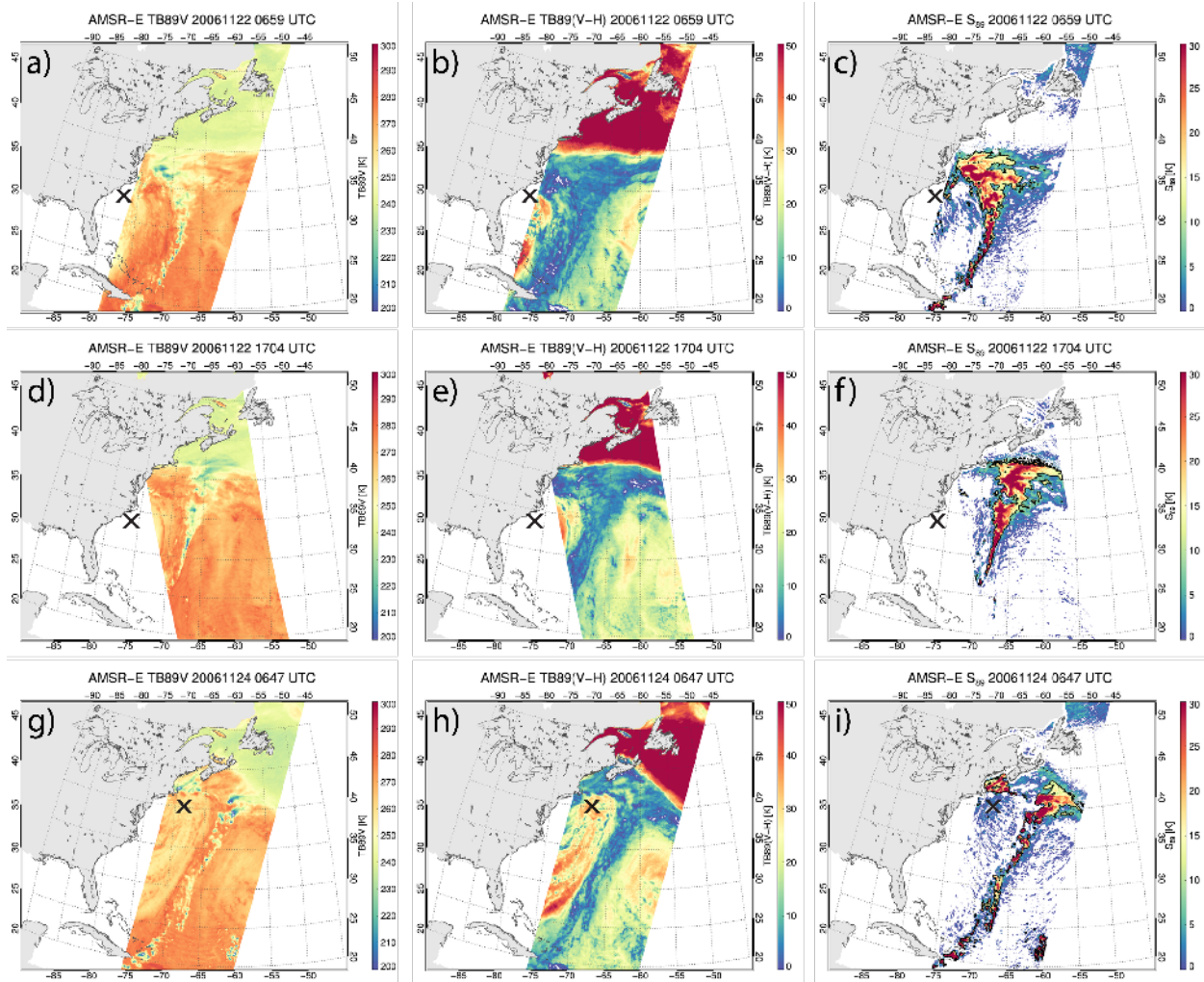


Figure 2.6: AMSR-E 89 GHz vertically polarized brightness temperature (a, d, and g), vertical – horizontal polarized brightness temperature difference (b, e, and h), and scattering index (c, f, and i) for 0659 UTC 22 November (a, b, and c), 1704 UTC 22 November (d, e, and f), and 0647 UTC 24 November (g, h, and i). Colored values correspond to values of each quantity, and the 10 GHz S₈₉ value is contoured in black in (c, f, and i). X marks the approximate location of the surface low center.

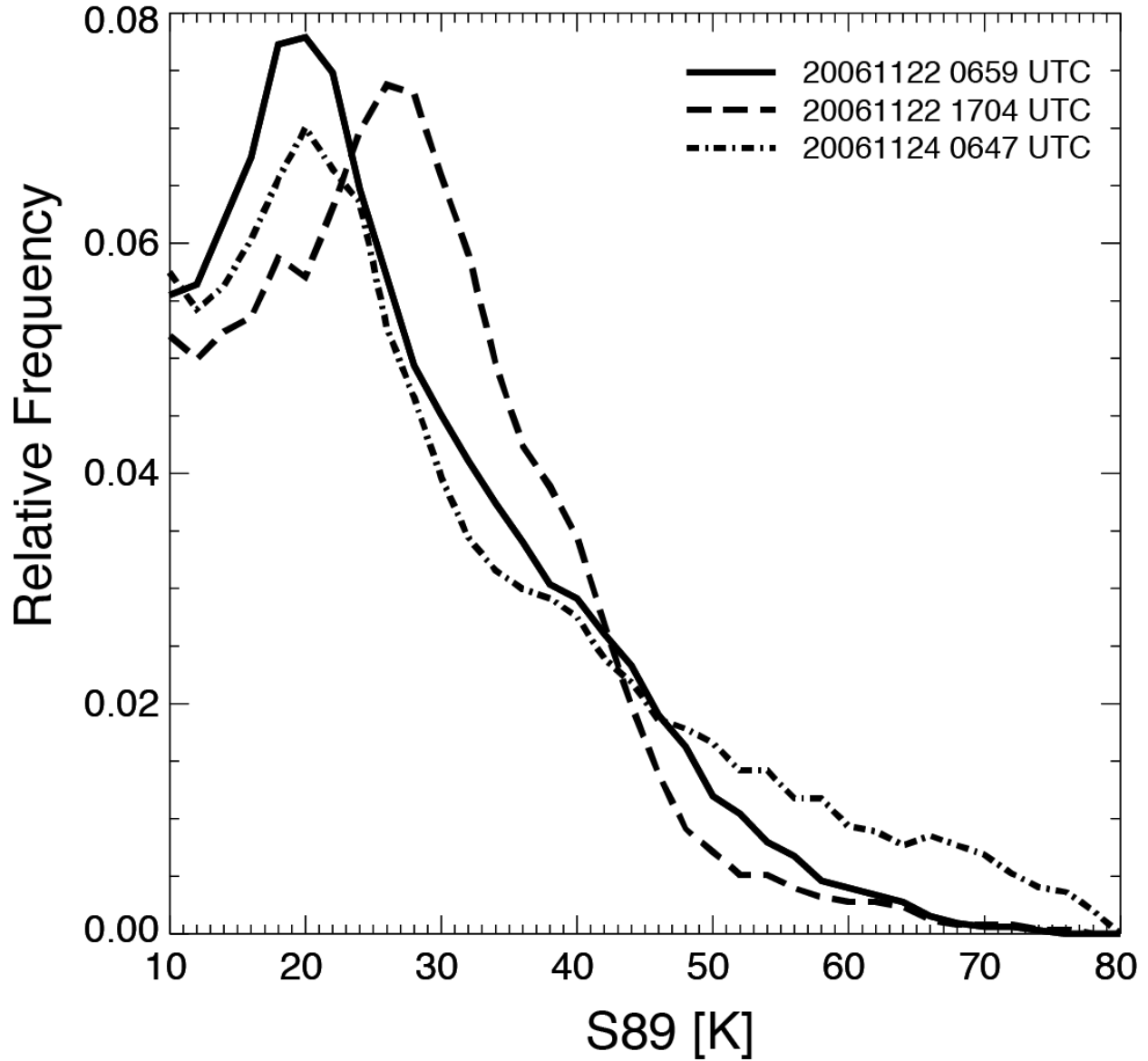


Figure 2.7: 89 GHz scattering index (S89) relative frequency of occurrence statistics for the three AMSR-E overpass times and geographic regions depicted in Fig. 7. Only pixels with S89 values exceeding 10 K and with associated AMSR-E surface precipitation rate retrievals exceeding 2 mm h⁻¹ are used to create the S89 histograms.

Chapter 3: Surface Heat Flux Analysis Around Extratropical Cyclones

3.1 Introduction

Surface sensible and latent heat fluxes (SHF and LHF, respectively) are produced by turbulent flow within the planetary boundary layer, and are primarily driven by surface wind speeds and differences in temperature and specific humidity between the surface and near atmosphere (typically around 10 meters above the surface). As discussed in Chapter 1, surface heat fluxes can transport energy and momentum between the surface and lower-atmosphere, influencing the development of weather systems from the synoptic scale down to the microscale. The increased energy being released from the surface into the atmosphere can decrease the static stability within the boundary layer and produce convective elements within extratropical cyclones (Vukovich et al. 1991). While there are several methods to estimate surface heat fluxes, the most common method is by using the bulk aerodynamic formulas, as they relate turbulent fluxes to observable spatial and temporal averages (Hartmann 1994). We can recall the bulk aerodynamic formulas from Chapter 1:

$$LHF = \rho_a L_v C_{DE} U (q_s - q_a) \text{ (Eqn. 3.1)}$$

$$SHF = \rho_a c_p C_{DH} U (T_s - T_a) \text{ (Eqn. 3.2)}$$

where ρ is air density at the surface, L_v is the latent heat of condensation, and c_p is specific heat at constant pressure. C_{DH} and C_{DE} are the exchange coefficients of sensible heat and moisture

(respectively), U is surface winds, T_s and T_a are temperature at the surface and 10 meters (respectively) and q_s and q_a are specific humidity at the surface and 10 meters (respectively).

As surface heat fluxes transport energy and momentum, they can increase the instability within the boundary layer. Strong positive surface heat fluxes are often associated with marine-based extratropical cyclones that form over warm ocean waters near cold continental landmasses. These marine-based ETCs provide the perfect opportunity for large surface heat fluxes to develop, as their strong surface winds draw cold-dry air from the landmass over a warm-moist ocean surface; as the bulk aerodynamic formulas indicate, this allows for large positive values of LHF and SHF. As discussed in Chapter 1, these strong fluxes can help strengthen an ETC by decreasing the static stability within the boundary layer. An influx of moisture, because of high surface heat fluxes, can decrease the height of the lifting condensation level, where once it intersects with the top of the boundary layer, can lead to the production of convective elements (Vukovich et al. 1991; Cione et al. 1993; Catto 2016).

Given that the extratropical cyclone discussed in Chapter 2 occurred in an area where strong surface heat fluxes were likely, it possible that surface heat fluxes contributed to the stratiform-to-convective transition observed by CloudSat within the warm front. This ETC formed off the coast of the United States over the warm-moist Gulf Stream and had strong surface winds associated with it, allowing it to possibly develop strong heat fluxes. In the next section, we will analyze the surface heat fluxes associated with the case study that was originally presented in Chapter 2, and examine if surface heat fluxes correlated with the stratiform-to-convective transition observed within the warm front.

3.2 Latent and Sensible Heat Fluxes Observed during the November 2006 Case Study

Estimates of surface sensible and latent heat fluxes were obtained from the second version of the Modern-Era Retrospective analysis for Research and Applications (MERRA-2; Rienecker et al. 2011; Posselt et al. 2012; Naud et al. 2012; 2015; 2016; Molod et al. 2015) hourly reanalysis data set, with a spatial resolution of $0.625^{\circ} \times 0.5^{\circ}$. We use the MERRA-2 reanalysis data in this part of our analysis due to its temporal resolution, which allow us to analyze how these surface fluxes might change at hourly time scales, if needed. Additionally, since MERRA-2 data are assimilated using various satellite observations (Gelaro et al. 2017), it will offer a natural transition between the analysis offered here and the satellite analysis in other chapters.

Throughout our case study of the late November 2006 marine extratropical cyclone, large values of latent and sensible heat fluxes were observed within its immediate vicinity (Figure 3.1). As the storm began to develop on 21 November, LHF and SHF values of over 500 W/m^2 and 250 W/m^2 (respectively) were observed in the western portion of the cyclone immediately off the coast; this is related to the cold and dry atmospheric air flowing over the relatively warm Gulf Stream oceanic current. As the cyclone moved poleward on 22 November, the local maximum of the surface heat fluxes shifted to the southern portion of the cyclone; SHF decreased to 200 W/m^2 while LHF hovered around 500 W/m^2 . The surface heat fluxes observed on these dates correlate well with previous ETC and surface heat flux analysis (e.g. Neiman and Shapiro 1993). This could indicate that the energy released by the surface into the atmosphere by these fluxes are being transported directly into the cyclone and warm conveyor belt, strengthening the cyclone and allowing its central low pressure to increase (Figure 2.2). However, a trajectory analysis of this cyclone would need to be conducted in the future in order to definitively state this. Though these

strong heat fluxes were observed within and around the cyclone as it developed, LHF and SHF values ended up decreasing as the cyclone continued to move poleward.

As the ETC continued to develop on 23 November, there was a large decrease in surface heat fluxes around the cyclone. Only a small localized area of heat fluxes were observed in the same areas as the previous two days, though even these values of 300 W/m^2 for LHF and 150 W/m^2 for SHF were lower than the previous two days. This can be related to a decrease in the surface wind speeds, as winds dropped to around 15 knots (compared to 30 knots on 21 November). However, as the fluxes near the coastline and cyclone center decreased, there was an increase in latent and sensible heat fluxes ahead of the warm front, around 40°N 60°W , at this time. This increase in heat fluxes, over 400 W/m^2 for LHF and 100 W/m^2 for SHF, can be associated with an increase in surface wind speeds observed at this time, along with cooler and drier air being transported from the polar regions, increasing these fluxes based on the bulk aerodynamic formulas.

This area of increased surface heat fluxes coincides with the location of the convective portion of the warm front observed on 24 November. Though CloudSat observations of the warm front were not available on 23 November, we can assume that the warm front was transitioning from stratiform to convective around this time based on the observations on 22 and 24 November (Figure 2.5). As this transition is occurring, an increase in sensible and latent heat fluxes around the warm front were observed, which could be increasing the instability in the lower atmosphere and fueling this convective transition. However, it is not possible to definitively state the surface heat fluxes observed were the cause of this transition, as there could be other factors (such as latent heating aloft within the warm front). Further modelling studies are needed in order to conclude what caused this transition, which will be discussed in Chapter 6.

Though reanalysis datasets like MERRA-2 assimilates satellite observations for its procedures (Rienecker et al. 2011, Gelaro et al. 2017), we believe that it is important to be able to estimate surface heat flux products directly from remote sensing platforms. Satellite data can provide near continuous coverage throughout the whole globe and can provide critical information when in-situ data is limited (such as over the oceans). Though there are various obstacles in regards to estimating surface heat fluxes from space, this thesis offers a foundation for improved and reliable surface heat flux estimates by utilizing a new satellite mission designed to offer improve wind speed estimates over the tropical and subtropical oceans.

3.3 Estimating Surface Heat Fluxes from Spaceborne Instruments

At the time of writing this thesis, no current satellite mission is able to directly observe surface heat fluxes. However, current satellite technology is able to observe the components needed to estimate surface heat fluxes, such as surface wind speeds, temperature, and specific humidity through scatterometers and radiometers. The advantage of using remote sensing to estimate surface heat fluxes is that it offers continuous coverage throughout most of the globe, whereas in-situ measurements can be limited in time and space. However, there are many difficulties when it comes to these estimates, as current satellite technology often cannot accurately observe surface processes in the presence of clouds and precipitation, leaving observational gaps. Additionally, many polar orbiting satellites can miss large portions of a synoptic or mesoscale system, excluding key data that might be needed for analysis. These errors and gaps can then be multiplied if one tries to use them for surface heat flux analysis.

These issues are seen in Figure 3.2, which are QuikSCAT wind speed observations of the same ETC discussed in Chapter 2 and Section 3.2. The QuikSCAT SeaWinds active microwave

instrument (13.4 GHz) was a polar orbiting instrument that observed signals reflected from the ocean surface, and using surface roughness to estimate near-surface wind speeds (Schlax et al. 2001). Though it provided good surface wind speed observations, heavy clouds and precipitation attenuated its signal, leading to gaps and inaccuracies within its observations. This can be problematic when observing surface winds within and around tropical and extratropical cyclones, as both feature heavy bands of precipitation. Missing winds in precipitating regions can be seen in QuikSCAT observations that were taken during the lifetime of the ETC that was the focus of our case study (Figure 3.2). While the observation from 22 November shows strong winds just off the coast of the United States, there are regions of missing data and areas of low surface wind speeds in this portion of the storm. When comparing this plot side-by-side with the rain impact from the same observation, one can see that rain had a large impact on the observation of these surface winds, and led to the decreased estimated wind speeds or missing data, neither of which are suitable for the estimates of surface heat fluxes. Along with signal attenuation, we see how QuikSCAT is missing large portions of this cyclone due gaps between swaths, especially areas where we expect strong surface winds and large sensible and latent heat fluxes (Figure 3.1).

If we were to use scatterometers, like QuikSCAT, to provide surface wind speed observations in order to estimate sensible and latent heat fluxes, it could lead to inconsistent and inaccurate results due to signal attenuation and gaps in coverage due to their orbits, especially in tropical and midlatitude regions. Additionally, the MERRA-2 reanalysis dataset uses these scatterometers and microwave radiometers, like QuikSCAT and SSMIS, for its surface wind speed estimates (Gelaro et al. 2017), which could lead to inaccurate estimates of sensible and latent heat fluxes. However, by using CYGNSS's improved coverage over the tropical and subtropical oceans, we could provide continuous and improved estimates of sensible and latent heat fluxes.

While the precipitation field in extratropical cyclones is small in comparison to tropical cyclones, and may not feature large heat fluxes, its ability to offer continuous coverage where previous instruments have lacked (Figure 3.2) could lead to better analysis of low-latitude extratropical cyclones.

3.4 Conclusions

While CYGNSS is designed to provide surface wind speed estimates, its ability to provide these observations in nearly all weather conditions could lead to improved and more consistent estimates of surface sensible and latent heat fluxes. As mentioned in Chapter 1, the exchange coefficients (C_{DH} and C_{DE}) are computed as a function of surface winds over the oceans, which allows CYGNSS to provide two of the main components needed to estimate surface heat fluxes. While the thermodynamic variables, like temperature and humidity, will need to be provided through a reanalysis dataset or other satellite missions, by using improved CYGNSS surface speed estimates, which will be shown in Chapter 5, we can take the next steps in offering improved latent and sensible heat flux estimates over the tropical and lower midlatitude oceans.

Our main concern regarding surface heat fluxes is how they influence the genesis and evolution of marine based extratropical cyclones. As mentioned in Chapter 1, CYGNSS is a tropical mission with a core mission to focus on surface winds in tropical cyclones, while extratropical cyclones typically develop outside the tropics outside of CYGNSS's range (Ruf et al. 2013, 2016). At first glance, it may seem difficult to estimate surface heat fluxes within extratropical cyclones using CYGNSS; however, a number of low-latitude extratropical cyclones and fronts do form within CYGNSS's orbit, and these cyclones often feature high values of surface latent and sensible heat fluxes. (Small et al. 2008; Hoskins and Hodges 2002, 2005; Graf et al.

2017). As we highlight in our next chapter, despite being a tropical satellite mission, CYGNSS is expected to observe a significant number of extratropical cyclones and fronts every year, which would aid in our understanding of how surface processes play a role in cyclogenesis and evolution at the lower latitudes (Crespo et al. 2017).

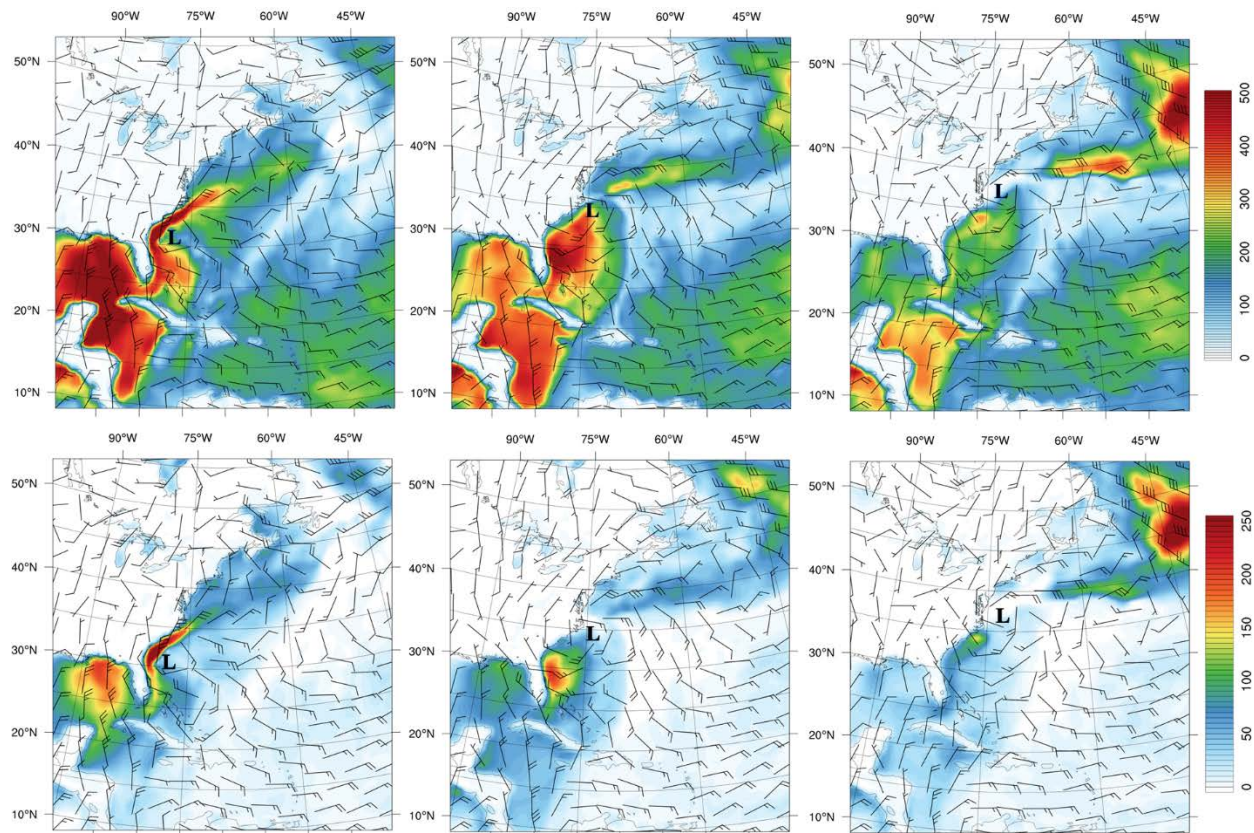


Figure 3.1: Surface latent heat flux (top, units: W/m^2) and sensible heat flux (bottom, units: W/m^2) on 21 November 1200 UTC (left), 22 November 1200 UTC (middle), and 23 November 1200 UTC (right); all overlaid with wind barbs of surface winds (m/s). **L** marks the approximate location of the cyclone center.

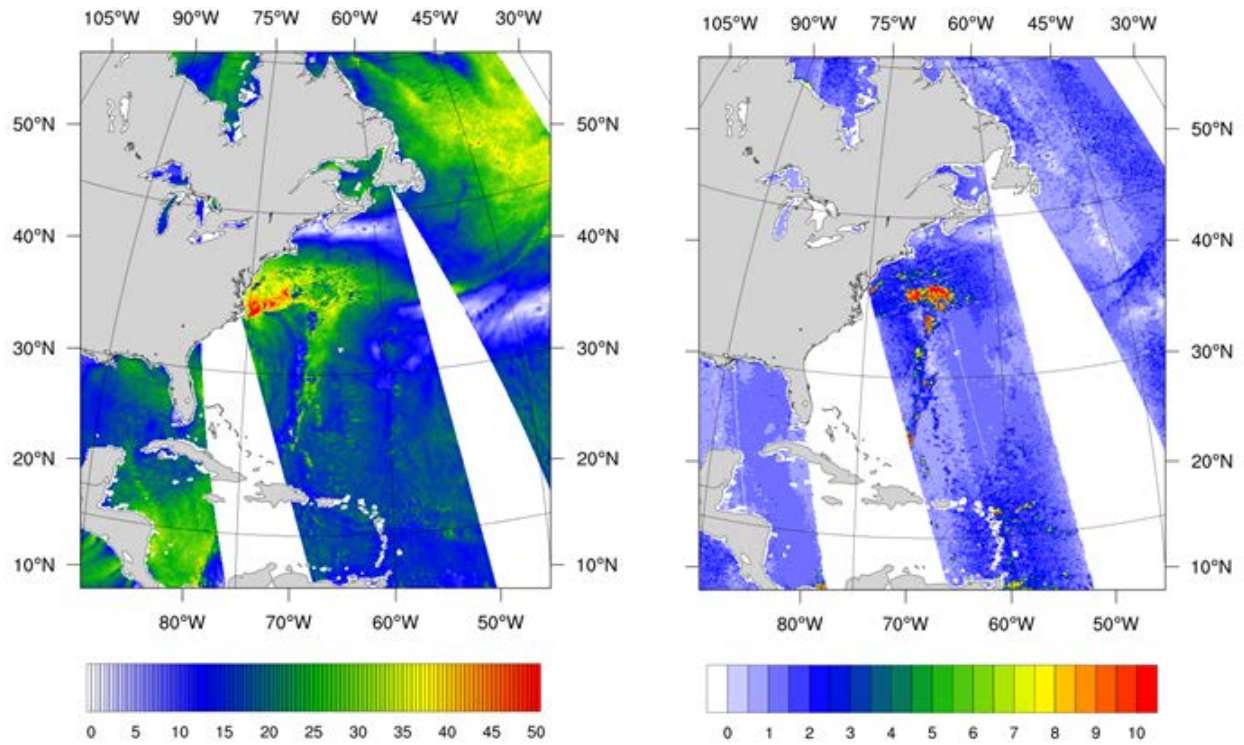


Figure 3.2: QuikSCAT observations from 22 November approximately 0700 to 1100 UTC. Left: Estimated surface wind speeds in knots. Right: Rain impact on surface wind observations, where: 0 = no rain impact, 10 = high rain impact.

Chapter 4: Assessing CYGNSS's Potential to Observe Extratropical Fronts and Cyclones

4.1 Introduction

Extratropical cyclones (ETCs) play a critical role in regulating Earth's energy balance, as they efficiently transport heat and energy from the tropical regions poleward, as well as influence the climate system through the clouds and precipitation they produce. ETCs and their fronts are associated with up to 90% of rainfall in storm track regions (Catto et al. 2012), and are an important source of freshwater for the middle and upper latitudes, as they produce a majority of the precipitation observed in the planet's temperate zones (Heideman and Fritsch 1988; Hawcroft et al. 2012).

Most of the water vapor that is converted to clouds and precipitation within extratropical fronts and cyclones is transported poleward by the warm conveyor belt (WCB; Harrold 1973; Browning et al. 1973; Carlson 1980; Browning 1986; Wernli 1997; Catto 2016). WCBs typically originate in a moist subtropical marine planetary boundary layer (PBL) between 20N°-47°N and 17S°-42°S (Wernli and Davies 1997; Eckhardt et al. 2004; Madonna et al. 2014), and transport large quantities of sensible and latent heat poleward and upward into ETCs (Browning 1990). The uptake of moisture in a WCB is commonly associated with anomalies of latent heat flux associated with a reduction of near-surface relative humidity and enhanced wind velocity (Neiman and Shapiro 1993; Pfahl et al. 2014).

The dynamics and evolution of ETCs at the synoptic level have been well-known for many decades (e.g., Bjerknes and Solberg 1922; Shapiro and Keyser 1990). However, there remain

unanswered questions associated with how changes in cyclone circulation and environment relate to variations to the distribution and intensity of clouds and precipitation, along with how surface processes, especially over the ocean, relate to ETC development (e.g. Crespo and Posselt 2016). Current in situ and remote sensing measurements are limited in their ability to observe surface processes in oceanic ETCs. The ocean surface around ETCs is often obscured by clouds, limiting the utility of visible and infrared remote sensing. Spaceborne passive microwave and radar instruments can penetrate clouds, but nearly all have infrequent revisit time and large data gaps, and/or have their signals attenuated by precipitation (as is the case for most scatterometers), causing them to miss key details in ETC development. As such, CYGNSS can observe a significant number of low-latitude extratropical fronts and cyclones, and aid in our understanding of how surface processes play a role in cyclogenesis and evolution in the lower-latitudes (Small et al. 2008; Hoskins and Hodges 2002, 2005; Graf et al. 2016). In this paper, we use an orbit simulator and a database of objectively identified ETC fronts and cyclone centers to demonstrate the frequency with which CYGNSS will observe marine extratropical cyclones forming in the lower midlatitudes, as well as show how representative the CYGNSS sampled surface winds and surface heat fluxes will be using a reanalysis dataset.

4.2 Data and Methods

4.2.1 Simulated CYGNSS Ground Tracks and Specular Point Locations

CYGNSS observes the signal from the Global Positioning System (GPS) reflected from the Earth's surface using a delay Doppler mapping instrument (DDMI) with a multichannel GNSS-R receiver, low-gain zenith antenna, and two high-gain nadir antennas. On every CYGNSS observatory, the DDMI selects four specular points each second within the highest sensitivity

region of its antenna view pattern. The wind-induced roughness of the ocean surface scatters the GPS signal, and the scattering signature is used to estimate the surface wind speeds at a 25 km spatial resolution per specular point (Ruf et al. 2016). Our analysis requires the locations of surface specular points for signals generated by the GPS transmitters, and observed by the CYGNSS constellation.

The Spacecraft Orbital Characterization Kit (SpOCK) simulates the trajectories of the GPS and CYGNSS constellations expected over a one-year period, assuming all eight satellites are in science data collecting mode and in their final constellation configuration. From the modeled positions and velocities of each transmitting (GPS) and target (CYGNSS) spacecraft, SpOCK derives the positions of the Earth's surface reflection points. These are defined as the locations where the angle between the local vertical and the GPS is equal to the angle between the local vertical and the CYGNSS observatory. Each CYGNSS satellite receives reflected signals from about 10 GPS transmitters at all times, but only the four signals with the highest range-corrected gains (RCGs) are selected, while the other specular points are ignored. The RCG is defined as the look-angle dependent antenna gain divided by the sum of the distance from CYGNSS to the surface specular point squared and the distance from the GPS satellite to the surface specular point squared. When all eight CYGNSS observatories are in science data collecting mode, the entire constellation returns 32 surface specular point observations each second.

4.2.2 Cyclone and Front Detection and Compositing Methodology

The cyclone and frontal transects are produced with the aid of an objective cyclone and front detection algorithm, which has previously been used to composite observations from A-Train satellite data (Naud et al. 2010; 2012; and 2015; Naud and Kahn 2015), and which we use in this

study to composite simulated CYGNSS specular point locations. Cyclone centers are identified using the algorithm described by Bauer and Del Genio (2006) and Bauer et al. (2016), and are freely available in an online database (<https://gcss-dime.giss.nasa.gov/mcms/>).

Identification of frontal boundaries utilizes 6-hourly gridded temperature, humidity, wind and geopotential height information (Naud et al. 2010; 2015; 2016), which were obtained from the second release of the Modern Era Retrospective analysis for Research and Applications (MERRA-2; Rienecker et al., 2011; Posselt et al., 2012; Molod et al., 2015). For this, aspects of two different objective and automated front detection algorithms are combined: a temperature gradient-based method described by Hewson (1998) and a wind direction and strength-based method used by Simmonds et al. (2012). As described in Naud et al. (2012), warm fronts are detected with the Hewson (1998) technique. Cold fronts are detected with both methods (see Schemm et al. (2015) for a discussion of each method's merits, and Naud et al. (2016) for a detailed description of how they are combined). Frontal locations are used as anchors for compositing MERRA-2 surface winds, latent and sensible heat fluxes along a line perpendicular to each front type, with the origin representing the frontal location at the surface, and the x-axis representing the distance from the front (e.g. Naud et al. 2012, 2015). The result is a database of front-relative composites for all fronts and cyclones detected within a given period of time.

CYGNSS observations commonly occur as continuous lines of specular points a few 100s of km in length along the Earth's surface, as a specific GPS transmitter's orbit carries it across the CYGNSS antenna gain pattern (Ruf et al. 2013, 2016). Using one year of synthetic CYGNSS footprints, and assuming no year-to-year variability in the orbits of either CYGNSS observatories or GPS transmitters, we can generate a synthetic sample of CYGNSS observations of fronts and cyclones from several years of MERRA-2 data. This second set of CYGNSS-specific warm and

cold front centered composites may then be compared with the full set of data sampled from all fronts and storms in MERRA-2 between 40°S-40°N to evaluate the robustness of CYGNSS's sampling.

4.3 Results

By using all extratropical cyclone features that were objectively identified in the MERRA-2 database from 2014-2015 and the one-year database of simulated CYGNSS specular points repeated over these two years, we can examine the frequency with which CYGNSS may observe ETCs and their fronts within the constellation's latitude range. Figure 4.1 depicts the expected frequency of number of simulated specular points that fall within 500 km of a cyclone center (Fig. 4.1a), and within 25 km of a warm front (Fig. 4.1b) and cold front (Fig. 4.1c) accumulated over both years. We use these constraints as ETCs often have diameters over 1000 km, while the fronts' direct surface impact and influence tends to occur close to the front itself (Naud et al. 2016). Despite the non-uniform sampling of the CYGNSS constellation (Fig. 4.1d), a significant portion of the globe between 40°S-40°N is observed by CYGNSS each day. As such, storms in the simulated CYGNSS sample exhibit a spatial distribution consistent with the preferred location of extratropical cyclones within the 40°S-40°N latitude band (e.g., Hoskins and Hodges 2002; 2005). The number of cyclones and fronts in the Northern Hemisphere increases with increasing distance from the equator. In the Southern Hemisphere, the number of CYGNSS simulated observations of cyclones and fronts is maximized around 25°S-35°S. Sampling of cyclones and fronts in the Northern Hemisphere are nearly twice as frequent in the western Atlantic relative to the eastern Atlantic, and nearly five times as frequent in the western Pacific relative to the eastern Pacific. These patterns reflect the influence of the warm western boundary currents (Kuroshio east of

Japan, Gulf Stream east of North America) on the development of ETCs. In the Southern Hemisphere, we see less zonal variability in ETC and front observations from CYGNSS. This is expected, as ETCs and associated WCBs are distributed more evenly throughout the Southern Hemisphere compared to the Northern Hemisphere (Eckhardt et al. 2004). While we do not know how many ETCs CYGNSS will observe per annum, our simulations imply that CYGNSS will be able to make many observations of ETCs developing in the lower latitudes.

Further assessment of the sampling effectiveness of the CYGNSS constellation can be assessed by examining the composite distribution of winds and surface fluxes across cold and warm fronts, and comparing the CYGNSS sub-sample with the full sample (40°S-40°N) from the MERRA-2 dataset. Figure 4.2 depicts the composite distribution of winds and surface latent and sensible heat fluxes for the entire database and for the CYGNSS subset for the 2014 and 2015 calendar years. Individual years are shown, as is the composite of all transects over two years; comparison between individual years and the total composite provides an estimate of the year-to-year variability in ETC locations compared to CYGNSS sampling. Since the observatories are intended to maintain even spacing around the Earth, their orbits will not change from year to year. If we assume consistent GPS transmitter orbits, then the differences between simulated observations in 2014 and 2015 will be due to changes in the location and frequency of ETCs in each year.

Consistent with previous studies (e.g., Sinclair 2013), wind speeds are maximized near the surface frontal boundary, with a local minimum at the location of the front itself. Wind speeds are larger in the warm sector ahead of cold fronts, with slightly weaker winds west of fronts in the cold air. This is consistent with stronger south to north transport ahead of the cold front associated with the warm conveyor belt (WCB). Winds are stronger poleward of warm fronts in a narrow

region approximately 100 km wide. The surface fluxes follow the distribution of winds in the cold air (west of cold fronts and poleward of warm fronts); however, they are much lower in the warm air equatorward and eastward of the cyclone center. Surface fluxes depend not only on the wind speed, but also on the surface to air temperature and water vapor contrast, and play a crucial role in ETC and front development (Neiman and Shapiro 1993). Smaller fluxes in the warm sector reflect the relatively higher near surface relative humidity in this region associated with the WCB, along with the relatively smaller air-sea temperature differences.

CYGNSS observes the distribution of wind speeds and fluxes across cold fronts (Fig. 4.2, left column) very effectively, with wind speed deviations in the composite of less than 0.5 m/s over a large range of distances from the surface front. While latent and sensible heat fluxes are also well observed, CYGNSS sampled fluxes exhibit a larger interannual range on the cold (west) side of the front relative to the warm (east) side. In addition, CYGNSS sampled sensible heat fluxes appear to be systematically larger than the full dataset by a few W/m^2 east of the frontal location. CYGNSS-sampled wind speeds and fluxes match the full sample very closely on the warm (equatorward) side of warm fronts (Fig. 4.2, right column), but exhibit more variability on the cold (poleward) side. CYGNSS-sampled wind speeds appear to be systematically higher by approximately 0.5 - 1.0 m/s. Consistent with higher wind speeds, latent heat fluxes are also larger poleward of the front in the CYGNSS sample, as compared with the full database. Interestingly, CYGNSS-sampled sensible heat fluxes are systematically lower on the cold side of the warm fronts. At first glance, this appears to run counter to the fact that the wind speeds are biased slightly high.

These discrepancies between the CYGNSS sub-sample and the complete MERRA-2 sample (40°S-40°N) on the cold side of warm fronts cannot be traced to retrieval errors, as the

CYGNSS-sampled data comes from the same source as the full dataset, and is not perturbed with any assumed retrieval noise. Instead, the differences are likely due to the CYGNSS sampling pattern. Recall that CYGNSS orbits in a tropical inclination with bounds at $\pm 35^\circ$ latitude; with a science antennae point at a 28° angle with respect to the sub-satellite point, dense specular point coverage extends to approximately 38° latitude, then rapidly decreases (Ruf et al. 2013). In practice, this means that there are relatively fewer CYGNSS samples with increasing distance poleward of the warm front. If the samples in the simulated CYGNSS dataset are biased equatorward, and if these samples also occur over regions with smaller air-sea temperature differences (as is more often the case at lower latitudes), then the surface sensible heat fluxes may be lower, even in the presence of slightly higher winds.

A more detailed evaluation of the CYGNSS sample versus the full MERRA-2 sample can be obtained by comparing histograms of wind speeds and surface fluxes over the full range of distances from the front, as well as for the cold and warm sides of the fronts independently (Figure 4.3). Histograms of wind speeds match closely for cold fronts, and there is little difference in the histograms of wind speeds on the cold versus warm sides of the fronts. The heat fluxes also match quite closely between the CYGNSS and full samples. As one might expect, given the greater air-sea temperature and water vapor contrast on the cold side of fronts, the latent and sensible heat fluxes are systematically higher in these regions.

In contrast to cold frontal regions, there are differences between the CYGNSS-sampled winds and fluxes in warm frontal regions. Close examination reveals that the histograms match much better on the warm side of fronts, relative to the cold side. On the cold side, it is clear that the CYGNSS sampled wind speeds are systematically higher across all values of wind speed by 0.5-1.0 m/s. In contrast, there are relatively fewer values of latent heat flux lower than $\sim 150 \text{ W/m}^2$,

and relatively greater numbers of latent heat flux values higher than $\sim 150 \text{ W/m}^2$ in the CYGNSS dataset.

4.4 Discussion and Conclusions

In this paper, we conducted an examination of the simulated CYGNSS sampling of MERRA-2 winds and surface fluxes across warm and cold fronts, using one year of simulated CYGNSS specular point locations and multiple years of cyclone center and front locations objectively identified in reanalysis data. Despite its tropical mission, we have shown that CYGNSS has the ability to observe extratropical cyclones and fronts developing in the lower-latitudes. Wind speed and surface flux distribution observed by simulated CYGNSS measurements matched the full cyclone sample very effectively, with somewhat larger deviations poleward of the warm fronts where CYGNSS does not observe as frequently. Our conclusion is that there will be sufficient information in the CYGNSS measurements during its nominal mission lifetime to provide new insights into the distribution of winds and surface fluxes in oceanic low-latitude ETCs, as well as future analysis of warm conveyor belts. As Madonna et al. (2014) stated, many WCBs begin their ascents near the surface over the oceans between $\sim 20^\circ$ - 40° in both hemispheres, an area that is well observed by CYGNSS. In addition, the ability of CYGNSS to observe winds even in regions of heavy precipitation, along with the planned co-location of CYGNSS surface winds with the Global Precipitation Measuring (GPM) mission Integrated Multi-satellite Retrievals (IMERG) precipitation dataset, will motivate studies of wind-precipitation relationships in frontal zones.

In closing, we wish to point out that the sampling study we have conducted provides the most optimistic estimate of CYGNSS's potential. In reality, the surface wind speed and surface flux retrievals will contain errors (2 m/s below 20 m/s wind speeds, 10% error above 20 m/s winds)

that derive from a number of different sources (Ruf et al. 2013). In addition, our study assumes consistent sampling with all eight CYGNSS spacecraft. In reality, there will be occasional periods where one or more of the spacecraft is taken out of science data mode and placed in drag mode to maintain constellation spacing. While this will lead to a small decrease in the number of samples available, we do not believe it will fundamentally change CYGNSS's sampling of ETCs and fronts.

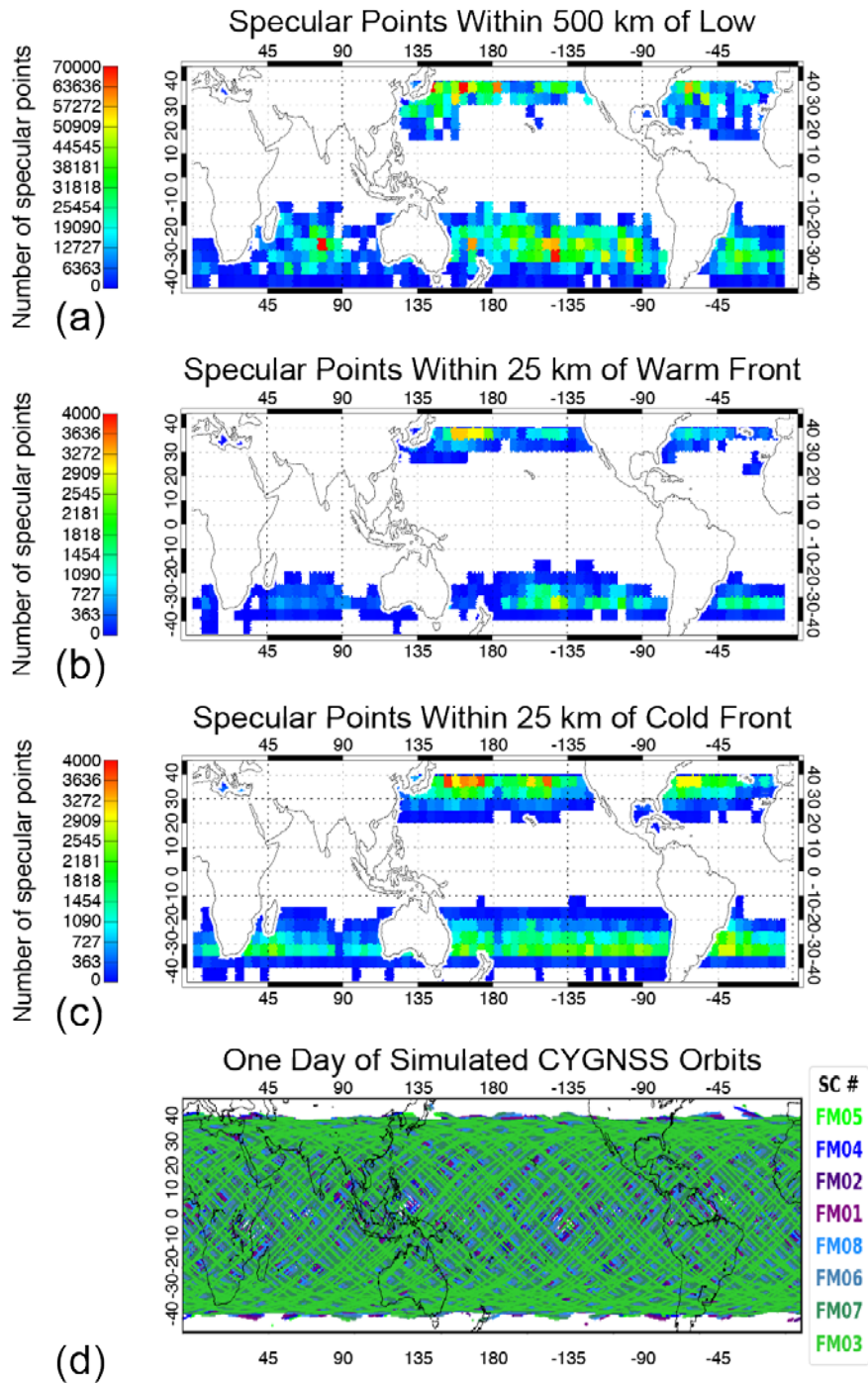


Figure 4.1: Frequency with which simulated CYGNSS specular points will pass within (a) 500 km of a low pressure center, (b) 25 km of a warm front, and (c) 25 km of a cold front over 2 years. The results are gridded into 5°x5° latitude/longitude boxes, and only results over ocean are shown. (d) Depiction of one day of simulated CYGNSS orbits showing the extent of coverage of each observatory in the constellation.

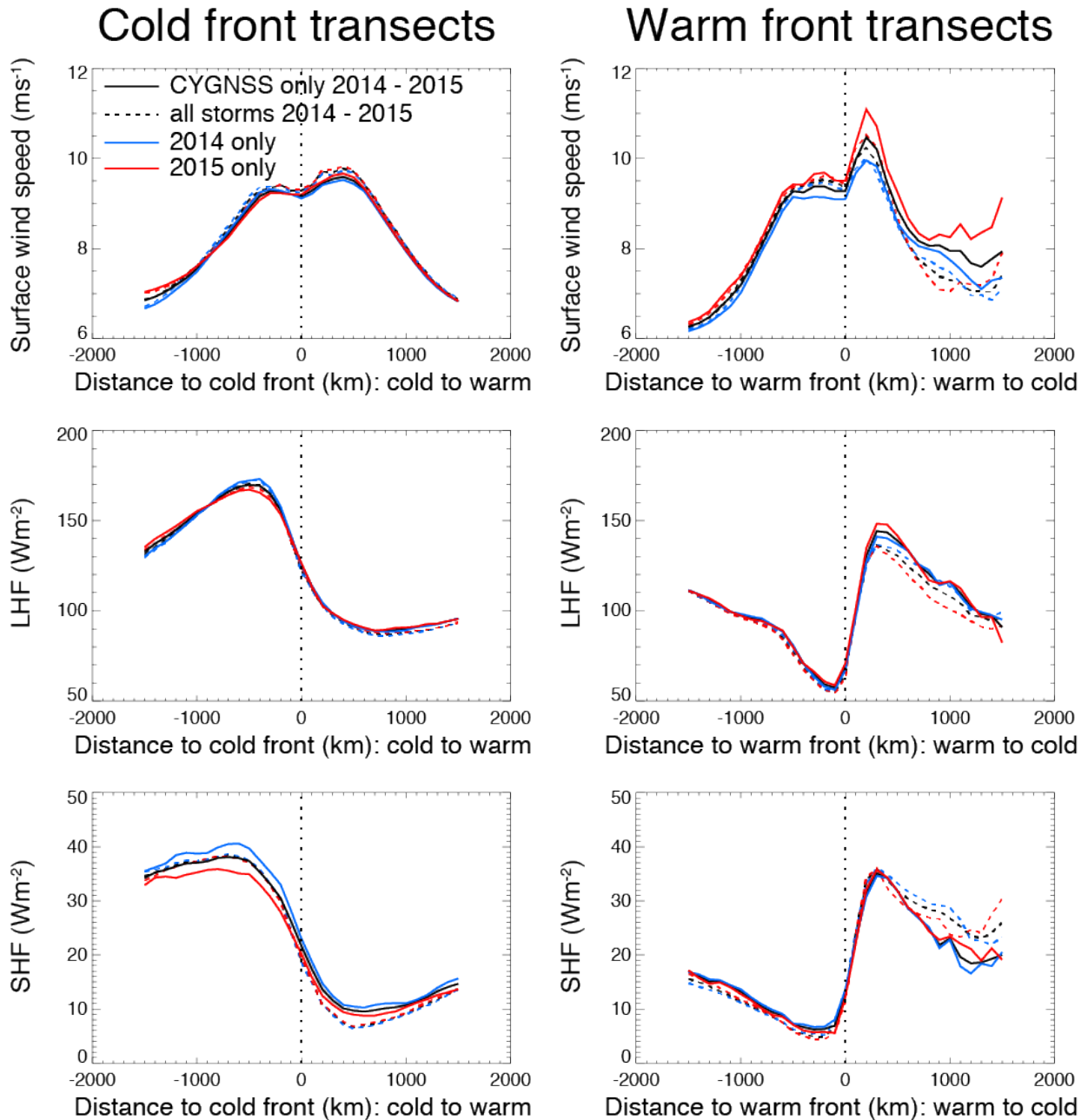


Figure 4.2: Distribution of winds (top row), latent heat flux (LHF; middle row), and sensible heat flux (SHF; bottom row) across cold fronts (left column) and warm fronts (right column) within the latitude range 40°S to 40°N . Shown are the results from the full set of storms (black lines), 2014 only (blue lines), and 2015 only (red lines) for the CYGNSS sample (solid) and the full sample (dashed).

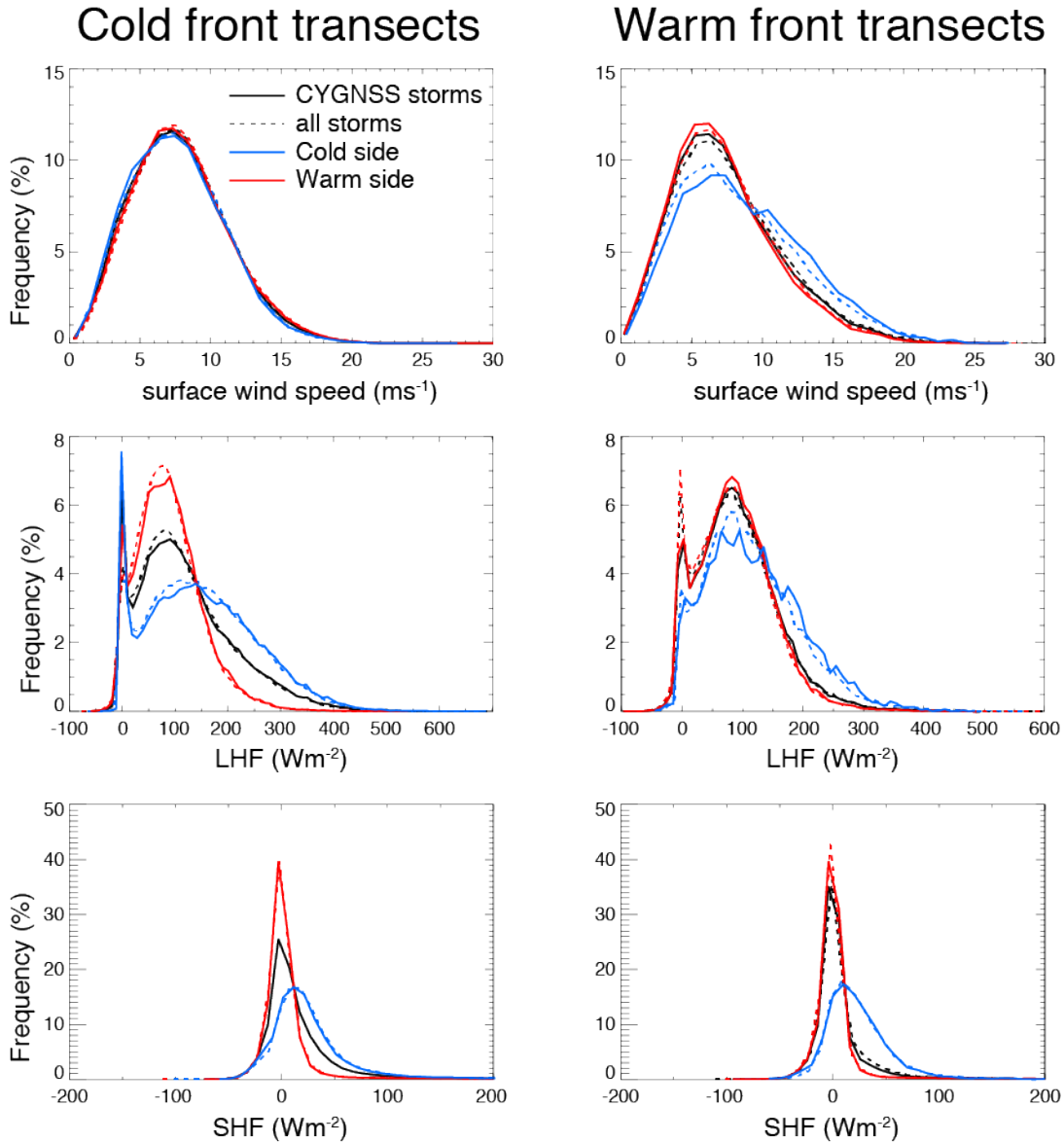


Figure 4.3: Frequency distribution of surface wind speeds (top row), latent heat flux (LHF; middle row), and sensible heat flux (SHF; bottom row) for cold fronts (left column) and warm fronts (right column). Results are divided into samples that occur only on the poleward and westward (cold) side of the cold and warm fronts (blue), only on the equatorward and eastward (warm) side of cold and warm fronts (red), and all samples (black). As in Fig. 4.2, the CYGNSS sample is represented by solid lines, while the full sample is dashed.

Chapter 5: CYGNSS Estimates of Latent and Sensible Heat Fluxes

5.1 Introduction

As mentioned in previous chapters, surface heat fluxes play a crucial role in the genesis and evolution of extratropical cyclones over the world's oceans, especially those that form over warm ocean surfaces near cold continental landmasses. Given the importance of these fluxes, it is crucial to our community that we can continually observe these fluxes. However, as discussed in Chapter 3, in-situ measurements over the world's oceans are limited to just a few buoys, preventing consistent measurement throughout the whole globe. Additionally, while polar orbiting satellites are able to fill in some of these gaps, they often cannot make proper surface observations in the presence of precipitation, and their orbits can cause them to miss areas of large surface heat fluxes, as seen in Figure 3.2. This is where the Cyclone Global Navigation Satellite System (CYGNSS) can fill in the gaps with improved coverage in the tropics and lower midlatitudes where other scatterometers have gaps in coverage due to their orbits. While the precipitation field in extratropical cyclones often does not feature large heat fluxes, this improved coverage could offer a unique tool for analyzing their development in the lower latitudes. Given its ability to observe and estimate surface winds in nearly all weather conditions, we can provide surface heat flux estimates wherever CYGNSS specular point observations are made and compliment the observations made routinely by current scatterometer and radiometer missions. Though thermodynamic variables will need to be provided from other sources, as will be discussed in the

next section, we can offer improved estimates of surface heat fluxes using surface wind observations from CYGNSS.

5.2 Data and Methods

5.2.1 COARE 3.5 Algorithm

The Coupled Ocean-Atmosphere Response Experiment (COARE) algorithm (Edson et al. 2013) is a widely used parameterization of the latent and sensible heat flux transfer coefficients. As described by Webster and Lukas (1992), COARE was initially designed to understand the principal processes in the region of the tropical western Pacific Ocean warm pool, such as the coupling of the ocean and atmosphere and the multi-scale interactions that extend the oceanic and atmospheric influence to other regions. The COARE bulk flux algorithm is based on the Monin-Obukhov similarity theory (MOST; Fairall et al. 1996, 1997), which has been widely used in estimates of surface heat fluxes over the oceans. COARE was originally intended for low to moderate wind speeds, but the latest version, COARE 3.5, is verified up to 25 m/s with direct flux measurements from various buoys. COARE 3.5 parameterizes the surface heat flux drag coefficients as a function of atmospheric stability, gustiness, and surface roughness, which can be mathematically expressed as:

$$C_D(z/z_0, z/L, G) = \frac{-\overline{uw}}{U_r S_r} = \frac{-\overline{uw}}{U_r^2 G} = \left[\frac{\kappa}{\ln(z/z_0) - \psi_m(z/L)} \right]^2 \quad (\text{Eqn. 5.1})$$

Where z is the height above the surface, κ is the von Kármán constant, z_0 is the aerodynamic roughness length, and ψ_m is a dimensionless function that accounts for the effects of atmospheric stratification. G is the gustiness parameter, defined as the ratio of the wind speed (S_r) to the vector-averaged wind (U_r) (Edson et al. 2013, Beljaars and Holtslag 1991). This parameter attempts to account for mass, momentum, and heat transfer at low wind speeds, but is non-zero because of

gustiness. This results in shear-driven turbulence produced by gusts that can drive significant exchanges in convective conditions (Fairall et al. 1996, Edson et al. 2013).

The drag coefficient algorithm was derived from thousands of direct covariance flux measurements collected over the midlatitude oceans throughout various field campaigns and programs. Given the drag coefficients, and external data sources of surface temperature, pressure, and water vapor, surface latent (LHF) and sensible (SHF) heat fluxes are computed using the standard bulk aerodynamic algorithms:

$$LHF = \rho_a L_v C_{DE} U (q_s - q_a) \text{ (Eqn. 5.2)}$$

$$SHF = \rho_a c_p C_{DH} U (T_s - T_a) \text{ (Eqn. 5.3)}$$

Here, L_v is the enthalpy of vaporization, U , T_a , q_a , and ρ_a are the wind, temperature, water vapor mixing ratio, and air density (respectively) 10 meters above the surface, and T_s and q_s are the sea surface temperature and water vapor mixing ratio, respectively. By using 10-meter surface winds (U) from CYGNSS and remaining variables from MERRA-2 hourly reanalysis data, we can obtain a first guess of the transfer coefficients (C_{DE} and C_{DH}) and surface heat fluxes. These are then placed into a stability iteration loop where the Monin-Obukhov length, roughness length, and transfer coefficients are computed, along with stability dependence and our latent and sensible heat fluxes. This loop repeats at least 3 times as the flux values reach an asymptote (Fairall et al. 2003, Edson et al. 2013), but for our purposes, we repeat the loop at least 10 times given the variability at each CYGNSS specular point. In the future, we plan to set up the loop to continue to iterate until the surface heat flux values reach an asymptote.

As mentioned earlier, the current COARE 3.5 algorithm has been verified for wind speeds up to 25 m/s and has been shown to yield accurate estimates of surface heat fluxes over the open ocean (Edson et al. 2013). This 25 m/s limitation primarily affects the computation of the drag

coefficient, as there is debate within the air-sea community regarding estimates the coefficient above this threshold. For our purposes, we do not calculate these fluxes when CYGNSS winds exceed 25 m/s, but future work could look into how to estimate these fluxes with high wind speed observations from CYGNSS. Additionally, we can compare our surface heat flux estimates from CYGNSS to heat flux estimates from the Kuroshio Extension Observatory (KEO) buoy and to surface heat flux estimates directly from MERRA-2. These comparisons are shown in Table 5.1, and will be discussed in further detail in Section 5.3.3.

5.2.2 Inputs to COARE from CYGNSS

The focus of this thesis is using surface wind observations from CYGNSS to estimate surface heat fluxes, as these wind speeds not only have a direct impact on these estimates, but also key in estimating the drag coefficients described in the last sub-section. The eight CYGNSS satellites orbit at a 35° inclination; its antenna field of view allows for consistent observations up to 38°, with some observations reaching beyond the 40th parallel in both hemispheres. As mentioned in Chapter 4, this allows us to observe extratropical cyclones that develop in the low-latitudes. Each CYGNSS observatory is able to measure GPS navigation signals that are scattered by the ocean surface using a delay Doppler mapping instrument (DDMI) that consists of a multichannel Global Navigation Satellite System reflectometry (GNSS-R) receiver, low-gain zenith antenna for reception of direct GPS signals, and two high-gain nadir antennas for surface scattered signal reception. CYGNSS uses the GPS L1 channel (1575 MHz, 19-cm wavelength), which does not experience appreciable attenuation in the presence of precipitation. The scattered signal and delay Doppler map (DDM) can then be used to estimate the approximate surface wind speed over a 25 x 25 km² region centered at the specular point location. The scattered power in

each DDM is highest near the specular point; this peak decreases as wind speed increases due to higher ocean roughness, and diffuse scattering away from the specular point increases with increasing wind speeds and ocean roughness (Ruf et al. 2016). This method allows CYGNSS to estimate surface wind speeds in nearly all weather conditions across the tropical and subtropical oceans.

5.2.3 Inputs to COARE from MERRA-2

Given that CYGNSS only provides surface wind speeds, we still need a source for temperature, specific humidity, and air density in order to estimate surface heat fluxes using the bulk aerodynamic formulas. Since coincidence between CYGNSS and other observations of thermodynamic quantities are limited, we have opted for using the Modern-Era Retrospective Analysis for Research and Applications, version 2 (MERRA-2) reanalysis dataset, which is an updated version of the original MERRA dataset (Rienecker et al. 2011, Gelaro et al. 2017). This hourly dataset at a $0.5^\circ \times 0.625^\circ$ resolution is the latest atmospheric reanalysis data set of the modern satellite era, which assimilates observations from various remote sensing instruments through the Goddard Earth Observing System (GEOS) model, which are detailed in Table 1 of Gelaro et al. (2017).

Given that CYGNSS specular point locations and MERRA-2 grid points do not always correlate, we need to estimate these thermodynamic variables along the CYGNSS specular point locations in order to estimate the surface heat fluxes. For the purposes of this thesis, we used the nearest neighbor approach by simply taking the MERRA-2 values at the grid point closest to the CYGNSS specular point in time and space. While this may introduce some inaccuracies, as the values are not varied to account for changes in time and space, we assume that the impact is

minimal, but can be assessed in future work. Given MERRA-2's finer resolution and data every hour, it is unlikely that these thermodynamic variables vary in short spatial and temporal scales. While these could vary within some weather phenomenon at these scales, this method should suffice for this extratropical analysis in this thesis.

5.2.4 Simple Sensitivity Analysis

While the COARE 3.5 algorithm has been shown to accurately estimate surface sensible and latent heat fluxes over the world's oceans up to wind speeds of 25 m/s, inaccuracies in the inputs could lead to inaccurate and variable estimates of the output fluxes. In order to estimate these sensitivities, we first generate 1000 perturbations for each of the inputs to the flux algorithm; these perturbations have a mean of zero and standard deviations consistent with assumed uncertainties in the MERRA analysis fields (from MERRA-2: air temperature, 1 Kelvin; sea surface temperature, 0.5 Kelvin; relative humidity: 5%; from CYGNSS: wind speed, 2 m/s. These random variables are then added to each input, individually, to create a distribution of perturbations at each specular point observed by CYGNSS in a single day, which are then plugged into the COARE 3.5 algorithm to create a distribution of surface heat fluxes for each input variable. We can then take the standard deviation of the surface heat fluxes at each point and average these standard deviations for the whole series, giving us a standard deviation for the whole series, which can then be interpreted as the general sensitivity for each input within the COARE 3.5 algorithm. Given that a single day of CYGNSS observations can produce over 1.5 million specular point observations, we limited our simple sensitivity analysis to just 15 September 2017 due to limited computing power and time. Along with the analysis across the entire CYGNSS mission for a whole day, we estimate these standard deviations within 25 km of the KEO buoy in the Western Pacific

Ocean, as this can highlight some of the variability that is possible in smaller regions, and will allow us to compare these sensitivities to KEO data in future work.

5.3 Results

CYGNSS has observed multiple extratropical cyclones in both hemispheres since it entered full science mode on 18 March 2017; our analysis here focuses on two of those ETCs: 21 March 2017 in the Western Pacific Ocean off the coast of Japan and 30 October 2017 in the Western Atlantic Ocean off the coast of the United States. As discussed in Chapter 4, we expect a majority of our ETC observations from CYGNSS to occur in these basins, as it favorable for ETC development and high surface heat fluxes. The following two subsections will show CYGNSS wind speed observations of these ETCs, as well latent and sensible heat flux estimates within and around these cyclones.

5.3.1 CYGNSS Surface Wind Observations of Extratropical Cyclones

Figure 5.1 displays an extratropical cyclone that develops over a 21-hour period as it is observed by CYGNSS. As it begins to form at 0000 UTC on the 21 March, even though the sea-level pressure indicates that the system is relatively weak, CYGNSS is already observing wind speeds around this time exceeding 15 m/s near the core of the cyclone, with winds on the equatorward side of the ETC reaching 25 m/s. While there is still some noise with the CYGNSS observations early on in its mission, we see that it is able to still capture some of the strong winds within and around this ETC as it begins to develop off the coast of Japan. Indeed, while there are some strong winds south of the cyclone, we can see that CYGNSS is able to observe the change in wind speeds as it observes the ETC and the calm open ocean.

Given CYGNSS's orbit, we do not see additional observations of this cyclone until around 2100 UTC on the same day. As the sea level pressure contours indicate, this ETC has strengthened with a low pressure below 980 hPa by this time, and the CYGNSS observations indicate the strengthening of this system. Though there is still some noise within the CYGNSS observations, overall it is able to observe the high wind speeds associated with this strong ETC, as winds are exceeding 25 m/s near the cyclone center. Much like the observations at 0000 UTC, CYGNSS is able to capture the change in wind speeds between the calmer open oceans and the faster wind speeds within the cyclones (with some exceptions). CYGNSS is also showing higher wind speeds in the southwest portion of the cyclone. This is key, as the next subsection will show that this is an area of high surface heat flux values. While CYGNSS is able to capture most of the wind speeds within the ETC at this time, it appears that it could be over-estimating the surface winds at the cyclone center. While one would expect higher wind speeds just outside the cyclone center, much like a hurricane, surface winds can be relatively low at the center of circulation of an ETC. This is likely an issue that will be addressed in future CYGNSS data releases that can better resolve these areas where the ocean surfaces are still rough but wind speeds are relatively calm.

Figure 5.2 highlights the extratropical cyclone observed by CYGNSS on 30 October 2017. Unlike the ETC in Figure 5.1, this cyclone moves poleward much more rapidly, only allowing for a few hours of observations. Additionally, the cyclone center is just beyond the range of the CYGNSS observatories. Nevertheless, CYGNSS is still able to observe the equatorward side of this ETC as it develops and moves poleward in the Western Atlantic Ocean. At 0000 UTC on 30 October, we see that CYGNSS observes high wind speeds, exceeding 25 m/s, on the southern end of the cyclone around the cold front. Much like the 21 March case study, there is noise in the wind speed estimates, but overall CYGNSS is able to observe high wind speeds around this part of the

ETC. Given that the storm developed rapidly, and moved from the ocean over land, our observations are limited compared to the previous case study. Even so, at 0300 UTC, while some winds have weakened at this point as the cyclone center moves further away, CYGNSS is still able to observe the strong winds associated with this cyclone, as they still exceed 25 m/s at some points.

Even though CYGNSS is not able to capture a majority of this ETC, much like the other case study, it was able to observe the southwestern portion of this cyclone, where high surface heat fluxes are expected. It is in these areas where, as cyclones turn counterclockwise in the northern hemisphere, they bring cold dry air over from the continents over warm and moist ocean surfaces. Coupled with the strong winds observed from CYGNSS, we expect that these will be areas of strong latent and sensible heat fluxes, as estimated by the bulk aerodynamic formulas (Eqns. 5.2 and 5.3).

5.3.2 CYGNSS Estimates of Surface Heat Fluxes around Extratropical Cyclones

By taking the CYGNSS surface wind speed estimates from these cyclones and inputting them, along with the thermodynamic variables from MERRA-2, into the COARE 3.5 algorithm described in Section 5.2.1, we can get estimates of latent and sensible heat fluxes within and around the ETCs discussed in the previous subsection. Figure 5.3 highlights the surface heat fluxes associated with the 21 March ETC in the Western Pacific Ocean around 2100 UTC. While there is some noise in these estimates given the noise from the CYGNSS observations, there is a large-scale signal in the surface heat fluxes. Though the storm had moved away from land at this time, strong latent and sensible heat fluxes continued to be observed in the southwest of the cyclone center, exceeding 400 W/m^2 and 150 W/m^2 , respectively. Additionally, there are strong heat fluxes directly west of the cyclone center; both of these locations correlate with high wind speed

observations seen in Figure 5.1, as well as strong air-sea differences in temperature and specific humidity. There is a region containing relatively large heat flux values just north of the cyclone center, where strong winds persist, along with moderate air-sea differences in temperature and water vapor. While not as prominent as the fluxes observed to the west and southwest of the cyclone center, these could still play a role in ETC development.

Figure 5.4 displays the surface heat flux estimates associated with the 30 October ETC at 0300 UTC. Much like the previous case study, we see large latent and sensible heat fluxes southwest of the cyclone center, this time exceeding 800 W/m^2 and 300 W/m^2 , respectively. A notable feature of this case study is the fact that these large flux values are exclusively located behind the cold front, which can be detected in the sea level pressure trough south of the cyclone center. This reflects our initial hypothesis that these fluxes will be focused in areas where cold dry air is interacting with the warm moist ocean surface, associated with strong surface winds. The fact that this cyclone formed closer to land than the 21 March case study may help to explain why these heat fluxes are twice as large. As this ETC formed closer to land, there is a smaller area for the air-sea differences to equalize, along with higher wind speeds as Figure 5.2 indicates, allowing for strong heat flux values.

These high flux values in both case studies indicate that a preponderant amount of heat and energy are being transported from the surface into the near atmosphere, and this turbulence is being induced by the strong surface winds as observed by CYGNSS. This energy being released into the near atmosphere can then be transported into the extratropical cyclone, which can go on and fuel the cyclone as it evolves. While we cannot quantify how much these surface heat fluxes play a role in the evolution of these ETCs, the observations shown here correspond well to previous studies

(e.g. Neiman and Shapiro 1993) that looked at surface heat flux influence on extratropical cyclones.

5.3.3 Comparisons of CYGNSS Surface Heat Fluxes with KEO

While we have initial estimates of CYGNSS-based surface heat fluxes that appear to be realistic, we still need to compare these estimates with an independent estimate. Traditionally, one would use direct heat flux in-situ measurements for comparisons and validation, but at the time of writing this thesis, there were no buoys available within CYGNSS's range that offered these direct flux measurements. However, we can estimate surface heat fluxes with buoys that provide measurements of surface winds, temperature, and specific humidity. One such instrument in the Kuroshio Extension Observation (KEO) buoy, which lies in the Western Pacific Ocean at 32.3° N and 144.6° E. By using its observations to compute latent and sensible heat fluxes from the COARE 3.5 algorithm, we can compare its heat flux estimates with those retrieved from CYGNSS. These comparisons are listed in Table 5.1, which also shows the direct flux estimates obtained from the MERRA-2 reanalysis data set.

Since KEO data was limited since CYGNSS's launch, we did not have comparison data for the two case studies discussed earlier, and instead picked dates with higher surface heat fluxes as observed by the KEO buoy. One of these comparisons can be seen in Figure 5.5; as Typhoon Talim approached Japan on 15-16 September 2017, CYGNSS was able to estimate high latent heat fluxes associated with this tropical cyclone. Though KEO, whose location is noted in the magenta diamond, was distant from this cyclone, it still recorded relatively large values of surface heat flux that could have been associated with this Typhoon. Even with these limited observations, we see that there is often not much agreement among the three sources when it comes to surface heat flux

estimates. While there may be some similarities and relationship between the KEO and MERRA-2 surface heat flux estimates, the CYGNSS observations tend to vary and do not have a definite signal when comparing between the KEO and MERRA-2 fluxes. One reason for this is that the closest CYGNSS specular point to the KEO buoy does vary (whereas the MERRA-2 grid points are consistent), but as will be shown, surface wind speeds being used to compute these surface heat fluxes lead to most of these differences, as it is the lone variable that changes between CYGNSS, KEO, and MERRA-2. There are differences in temperature and humidity observations between KEO and MERRA-2 that lead to differences in heat flux estimates, but for now we are focusing on surface winds as that is the variable we receive from CYGNSS and varies between the three datasets.

As Table 5.2 shows, the surface wind speed estimates at these times can vary between these three observing and reanalysis systems. While there is some variability between KEO and MERRA-2 wind speeds, the greatest variability comes from CYGNSS, where differences in wind speeds are exceeding 15m/s when compared to KEO or MERRA-2. These differences in wind speed estimates correlate with extreme differences in LHF and SHF estimates. One example is seen on 25 September at 08z, as the CYGNSS surface wind observations are exceeding 23 m/s, compared to 5-7 m/s from KEO and MERRA-2. As we recall from earlier chapters and sections, LHF (Eqn. 5.2) and SHF (Eqn. 5.3) are functions of surface wind speeds, and the drag coefficients used in LHF and SHF calculations (Eqn. 5.1) are a function of surface wind speeds. If the surface wind speeds are variable, it can lead to inconsistent estimates of surface heat fluxes. Ultimately, further analysis and comparisons are needed as the sample points here are limited, but this shows that CYGNSS is still early in its mission, wind speed estimates might still have some errors, which could feed into inconsistent estimates of surface sensible and latent heat fluxes as they were not

all flagged and filtered out before this analysis. In the future, this is an area of an improvement, especially as the data improves.

While some of the differences in surface fluxes related to the inputs, there are differences between COARE 3.5 and MERRA-2 even with the same inputs. As we see at 11z on 16 September in Tables 5.1 and 5.2, wind speeds from CYGNSS and MERRA-2 are nearly identical, but their latent heat flux values greatly differ. This is most likely coming from the differences in flux algorithms. As Figure 5.6 shows (from Garfinkel et al. (2011)), we see that as wind speeds increase, the difference in drag coefficient computed by MERRA-2 ('new' line) and those calculated by COARE increases. These differences in drag coefficients could be one reason as to why surface flux values may differ, even with the same inputs.

5.3.4 COARE 3.5 Sensitivity Analysis

Given the possible variability from the inputs that go into the COARE 3.5 algorithm, it is necessary to estimate the sensitivity of the inputs and the impact they could have on the heat flux estimates when one assume the potential errors associated with these inputs. As mentioned in section 5.2.4, by taking the standard deviations for each input (listed in Table 5.3), creating perturbations for each, we can calculate the standard deviation for these fluxes as a result of these perturbations. As a result, we can see how much these surface heat flux estimates can vary when accounting for the possible errors with these inputs of temperature, humidity, and wind speed (Table 5.3). When looking at a whole day of data, variations in latent heat flux are greatest from the 10-meter air temperature, followed by relative humidity and wind speed, with some variation from surface temperature. With the exception of relative humidity, we can also observe relevant variations from these inputs when it comes to sensible heat flux estimates. While these values are

smaller, one should note that sensible heat fluxes in general are lower compared to latent heat fluxes, as one can see with the surface heat flux averages on the left side of Table 5.3.

As a comparison, we also looked at the sensitivity of the algorithm on a smaller area, specifically within an approximately 25-km radius around the KEO buoy, which will allow for comparisons with KEO in the near future. With nearly all the variables, the standard deviations for the surface heat fluxes decreased compared to the full day of data, with the exception of variations from surface wind speeds. Most likely, as the CYGNSS data is still new and has some noise in it, this variation could be exaggerated when looking at a few limited sample points. Additionally, we assume the same standard deviations across the board for each input, but these standard deviations for temperature and humidity from MERRA-2 could vary under different conditions (such as precipitation and heavy winds), which were not taken into account with in either sensitivity analysis. Additionally, the surface winds from CYGNSS have a standard deviation of 2 m/s. However, this only applies to winds up to 20 m/s, with it becoming 10% above this threshold (Ruf et al. 2016). Since we ignore wind speeds above 25 m/s for the COARE 3.5 algorithm, we assume this 2 m/s standard deviation for wind speeds between 20-25 m/s, which could lead to some additional errors.

As Figures 5.7 and 5.8 indicate, a majority of latent heat flux estimates tend to occur between 0 and 200 W/m², while a majority of sensible heat flux estimates is at or just above zero W/m². These graphs show that, over the course of one day across CYGNSS's orbit, when one looks at high values of sensible and latent heat fluxes, these values are not as common, and possibly could have greater sensitivity. As seen in Table 5.4, when we break down latent heat flux by 100 W/m² bins and estimate the standard deviations in each from the sensitivity analysis, we see an increase in variation the higher the fluxes become with relation to wind speed and relative

humidity. Part of this variation could come from the fact that there are fewer sample points at these high fluxes, which could lead to some natural variation. However, as these fluxes increase, it is mainly due to increases in wind speed and air-sea differences, which could introduce additional errors that could affect the sensitivity of the algorithm. If one were to look at multiple days of CYGNSS estimates of heat fluxes, it is possible that these standard deviations could decrease, but that will have to be determined in future work.

Despite these potential errors in this simple sensitivity analysis, we see how much of an impact these variations of the inputs could have on our surface latent and sensible heat flux estimates. While some of these variations may be out of our control, future work could be done to calibrate these surface heat flux estimates in order to reduce these variations that could occur in these calculations.

5.4 Conclusions

In Chapters 3 and 4, we discussed the theory behind being able to use CYGNSS to observe extratropical cyclones that form in the lower latitudes, and the importance of being able to estimate surface heat fluxes from space borne instruments wherever in-situ observations may be limited. As a result, this chapter helps prove the questions and theories laid out in those chapters, demonstrating that CYGNSS is not only able to observe ETCs that form in the lower latitudes, but can also be a vital tool with which to estimate sensible and latent heat fluxes at the ocean surface. While there is still work to be done with these surface heat flux algorithms, as well as further validation and calibration of the CYGNSS surface wind observations, this chapter provides a foundation for future work when it comes to estimating surface heat fluxes from the CYGNSS mission.

In the 21 March ETC case study, we see that CYGNSS was able to observe a majority of this cyclone as it developed throughout the day. It was able to obtain observations through its core, as well as some, but limited, observations on the poleward side of the ETC ahead of the warm front. As discussed in Chapter 4, CYGNSS is limited when it comes to observing the poleward side of warm fronts, as these are often at the edge of CYGNSS's range. Even though these observations were limited, they could provide some useful analysis of the contrast in fluxes equatorward and poleward of these fronts in the near future. Meanwhile, the 30 October case study has CYGNSS observations not only just on the equatorward side of this cyclone, but further away from the cyclone center as it rapidly moved poleward. Nevertheless, it still observed high wind speeds associated with this ETC as it formed just off the east coast of the United States over the western Atlantic Ocean. These two case studies showed that CYGNSS is not only able to observe low-latitude extratropical cyclones, but can observe portions of the ETCs where surface heat fluxes are the greatest.

Both of these case studies featured large surface heat fluxes as they formed over warm ocean waters near cold and dry continental air masses. In the southwest sector of these cyclones, they were pulling cold and dry air off these continents over the warm and moist ocean surfaces, which, coupled with the strong wind speeds, can increase the surface sensible and latent heat fluxes. Given their locations, CYGNSS was able to continually observe and estimate the strong surface heat fluxes associated with these extratropical cyclones. While the observations from these cyclones correlate well with previous studies, and one can assume that the energy being released from the surface into the atmosphere from these surface heat fluxes are playing a role in the evolution of these respective ETCs, it is difficult to quantify how much of an impact they actually had. Since these cyclones also moved out of CYGNSS's range after these quick time periods, it is

hard to say if they strengthened unless we used a different satellite or analysis tool. Future modelling analysis will be needed to quantitatively state how much of an impact these surface heat fluxes had on these extratropical cyclones, and the magnitude of the fluxes needed to change the stability of the lower troposphere in order to make the column unstable (as seen in the CloudSat observations in Figure 2.5).

Even though this is a relatively new way to estimate surface heat fluxes, we were able to use a well-known surface heat flux algorithm to estimate these fluxes up to wind speeds of 25 m/s. While the surface heat flux estimates from CYGNSS paint relatively good pictures of the details occurring within these case studies, when compared to KEO and MERRA-2 heat flux values, the data are varying greatly. While there are disagreements in the respective heat flux estimates from KEO and MERRA-2, the variations in heat flux estimates from CYGNSS have a greater variety, usually resulting in the variations from the latest surface wind speed estimates. We can see these variations as well in the sensitivity analysis, especially when looking at smaller spatial scales. Given that the CYGNSS data is still being processed and calibrated, these variations will likely decrease in the near future. Nevertheless, we are still able to extract a signal amongst the noise from CYGNSS when looking at these surface heat flux estimates at a larger scale, such as those shown in Figures 5.3 and 5.4. The future calibration of CYGNSS winds could improve these surface heat flux estimates at smaller scales, so that they could be used in mesoscale analysis and potential field campaigns.

Date	Time	Latent Heat Flux (W/m ²)			Sensible Heat Flux (W/m ²)		
		KEO	CYGNSS	MERRA-2	KEO	CYGNSS	MERRA-2
2017-09-15	07z	118.64	83.41	156.91	6.28	3.21	9.38
2017-09-15	09z	163.26	169.90	176.00	14.59	16.37	18.53
2017-09-15	11z	175.67	130.00	198.54	15.29	15.51	25.45
2017-09-16	10z	247.09	346.23	207.38	49.20	53.44	32.13
2017-09-16	11z	270.97	182.33	230.11	55.24	29.71	38.01
2017-09-22	07z	249.80	299.61	268.42	22.56	48.55	43.27
2017-09-24	04z	171.43	435.54	236.30	11.05	35.95	21.17
2017-09-24	05z	191.88	174.53	213.87	11.29	12.26	17.72
2017-09-25	02z	361.72	196.80	204.76	51.16	36.11	37.01
2017-09-25	08z	170.12	622.31	229.06	32.14	132.79	47.42

Table 5.1: Comparisons of latent and sensible heat flux (W/m²) estimates from KEO, CYGNSS, and MERRA-2.

Date	Time	Surface Wind Speeds (m/s)		
		KEO	CYGNSS	MERRA-2
2017-09-15	07z	6.40	3.41	5.52
2017-09-15	09z	8.03	8.00	6.14
2017-09-15	11z	7.95	5.20	6.55
2017-09-16	10z	9.09	12.49	5.42
2017-09-16	11z	10.10	6.50	6.49
2017-09-22	07z	8.55	12.92	8.57
2017-09-24	04z	7.53	18.42	7.82
2017-09-24	05z	7.93	7.89	7.25
2017-09-25	02z	9.81	6.83	5.47
2017-09-25	08z	5.21	23.03	6.51

Table 5.2: Comparisons of surface wind speeds from KEO, CYGNSS, and MERRA-2, which correspond to the same times listed in Table 5.1.

2017-09-15 All CYGNSS	Average from COARE	Average from MERRA2	MERRA σ	COARE σ	σ from TS	σ from TA	σ from RH	σ from Wind
SHF	8.77	11.03	15.15	13.82	5.63	11.34	0.23	2.44
LHF	124.59	126.77	62.72	86.33	17.05	37.32	24.79	28.90
σ Inputs	-	-	-	-	0.5 K	1 K	5%	2 m/s

2017-09-15 25km radius KEO	Average COARE	Average MERRA2	MERRA σ	COARE σ	σ from TS	σ from TA	σ from RH	σ from Wind
SHF	10.44	15.26	8.74	8.74	4.10	8.27	0.18	2.90
LHF	125.15	167.40	30.26	47.59	15.85	25.45	21.29	36.05
σ Inputs	-	-	-	-	0.5 K	1 K	5%	2 m/s

Table 5.3: Results from the simple sensitivity analysis of the COARE 3.5 algorithm, created from the random perturbations generated using the standard deviations (σ) for each variable. Top table are the results for the entire CYGNSS constellation on 15 September 2017, and the bottom table is from the same day, but within a 25 km radius of the KEO buoy (32.3°N, 144.6°E).

<i>LHF</i> (W/m^2)	< 0	0-100	100-200	200-300	300-400	400-500	500+
σ from Wind	2.14	22.05	32.46	38.69	45.33	52.02	71.83
σ from RH	19.86	16.35	25.79	42.58	57.66	68.79	73.82

Table 5.4: Same sensitivity analysis from Table 5.3, but with 100 W/m^2 binned results of latent heat flux.

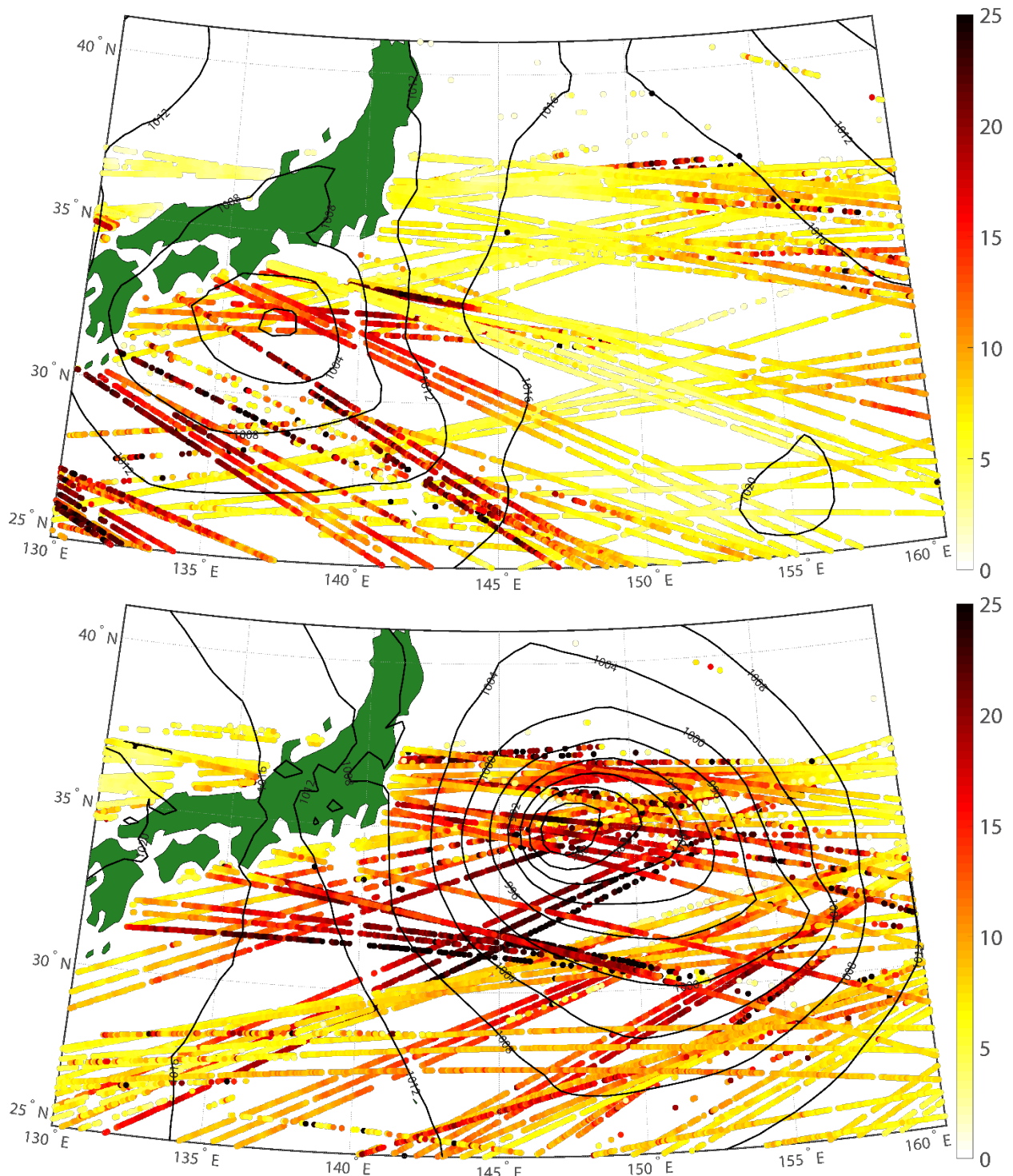


Figure 5.1: CYGNSS surface wind [m/s] observations on 21 March 2017. Mean sea level pressure (hPa, black contour) shown at 00z (top) and 21z (bottom), with CYGNSS winds ± 3 hours around this time.

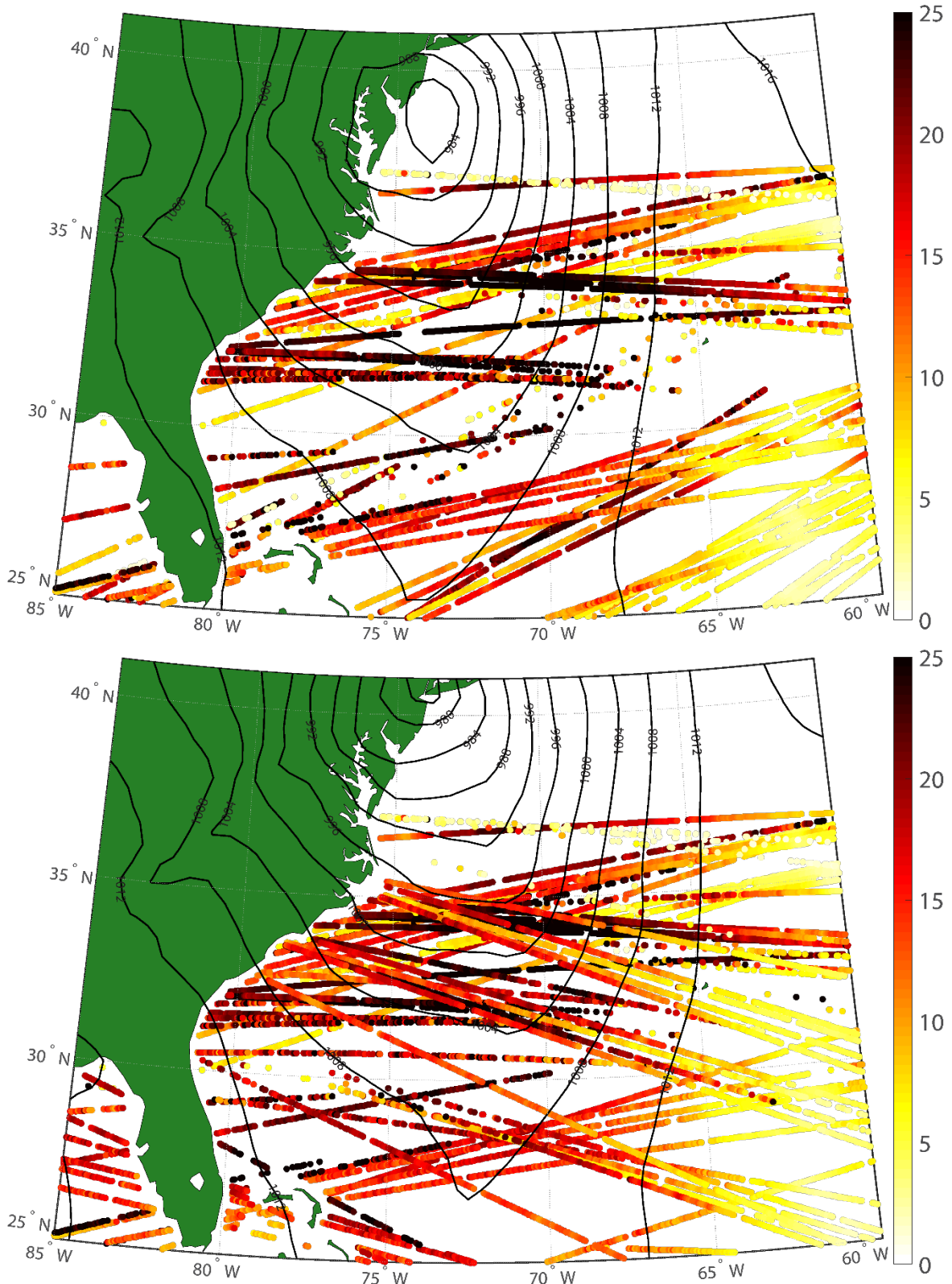


Figure 5.2: CYGNSS surface wind [m/s] observations on 30 Oct. 2017. Mean sea level pressure (hPa, black contour) shown at 00z (top) and 03z (bottom), with CYGNSS winds ± 3 hours around this time.

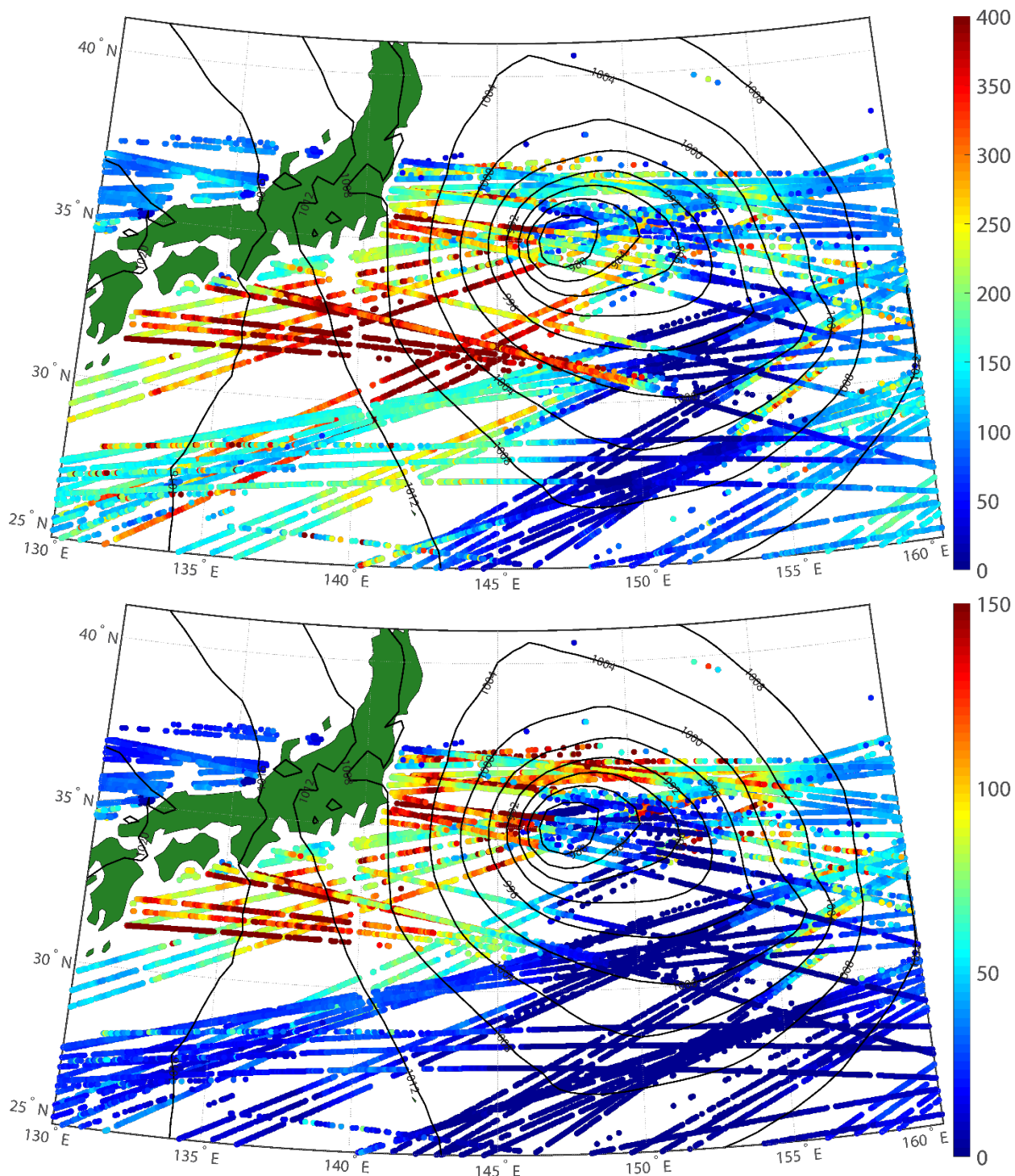


Figure 5.3: Latent (top) and sensible (bottom) heat flux estimates [W/m^2] on 21 March 2017. Mean sea level pressure (hPa, black contour) shown at 21z, with CYGNSS heat fluxes ± 3 hours around this time.

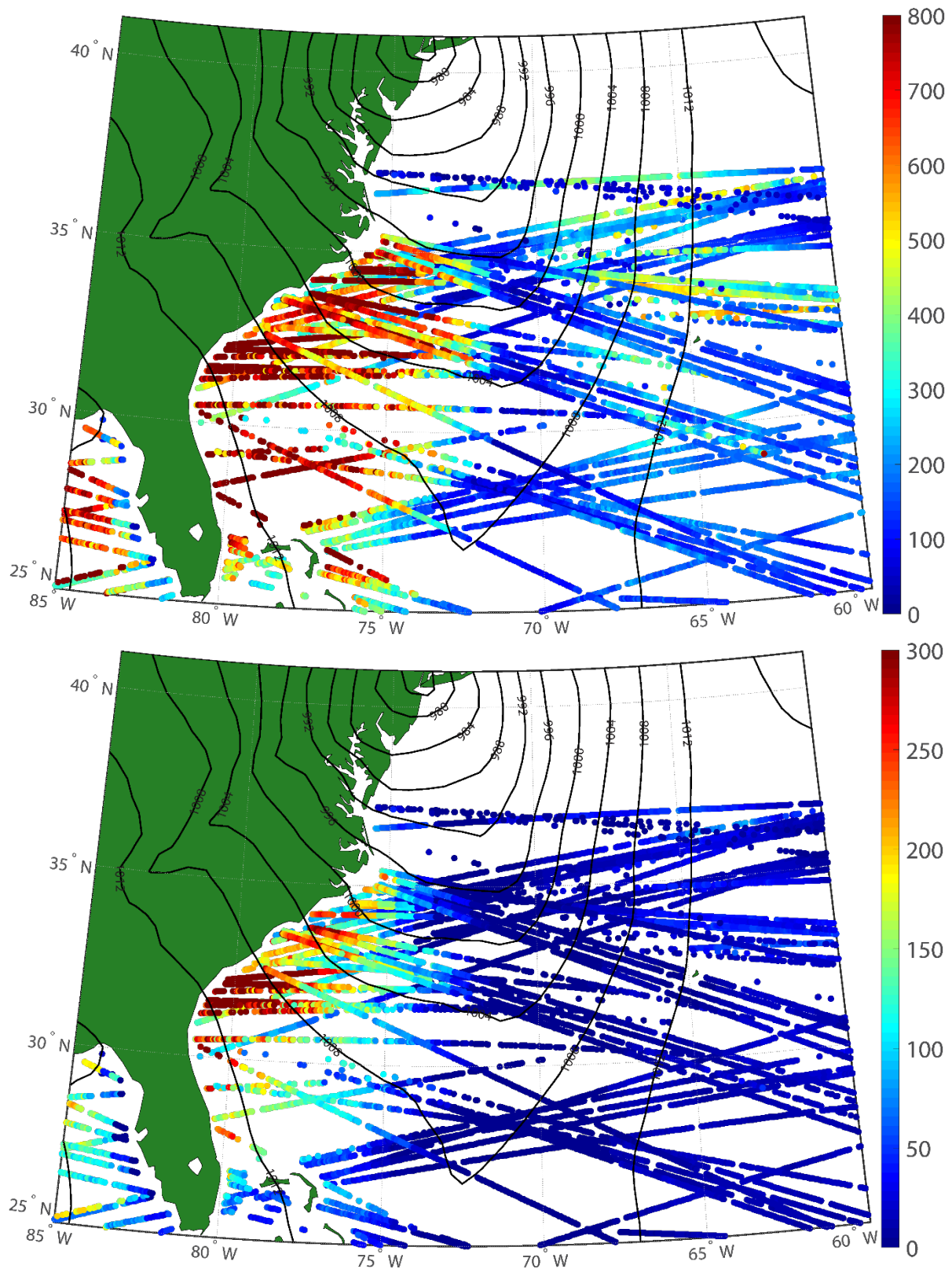


Figure 5.4: Latent (top) and sensible (bottom) heat flux estimates [W/m^2] on 30 October 2017. Mean sea level pressure (hPa, black contour) shown at 03z, with CYGNSS heat fluxes ± 3 hours around this time.

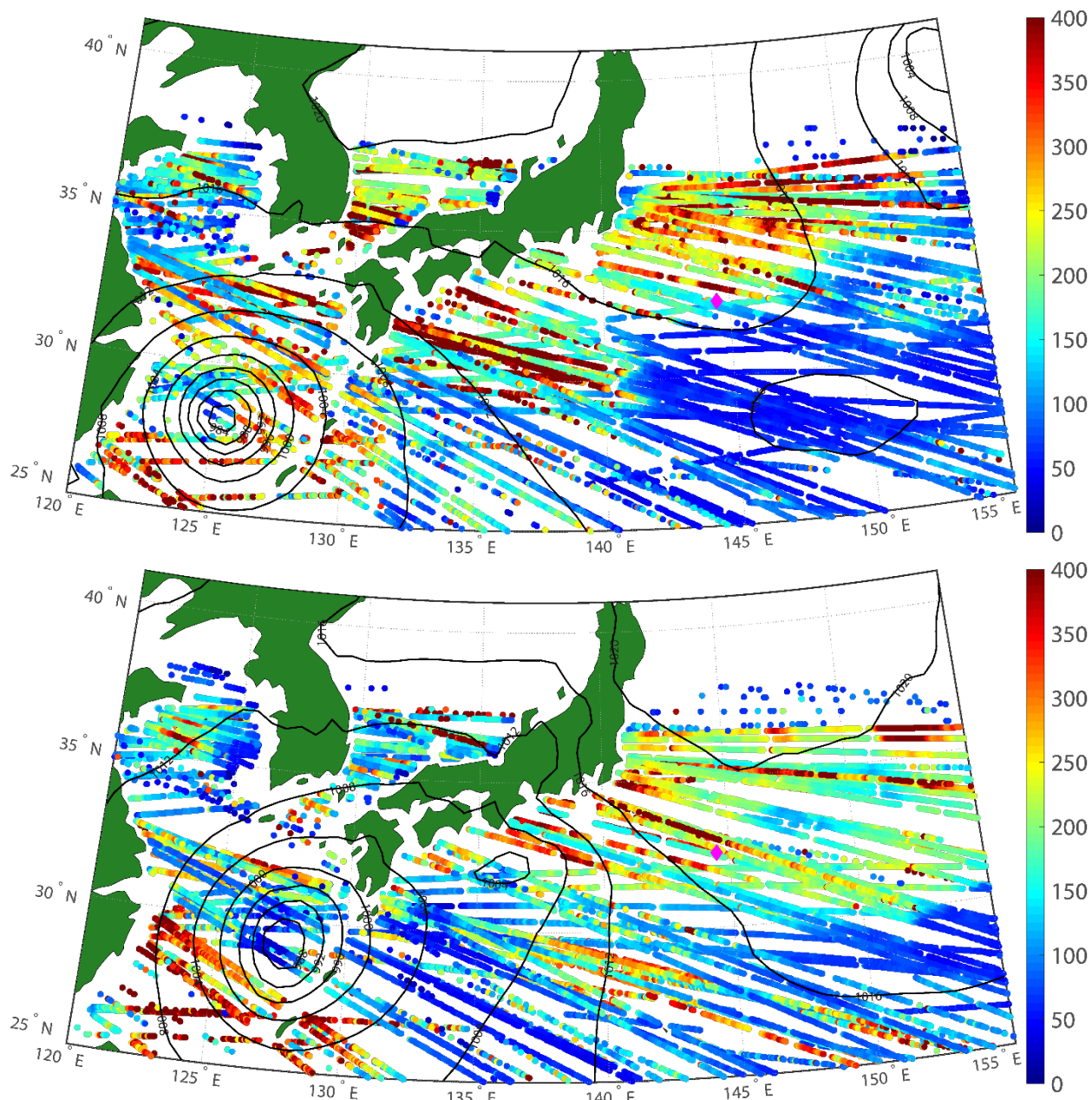


Figure 5.5: Latent heat flux estimates (W/m^2) on 15 (top) and 16 (bottom) September 2017 of Typhoon Talim. Mean sea level pressure (hPa, black contour) shown at 1200 UTC each day, with CYGNSS heat fluxes ± 3 hours around each time period.

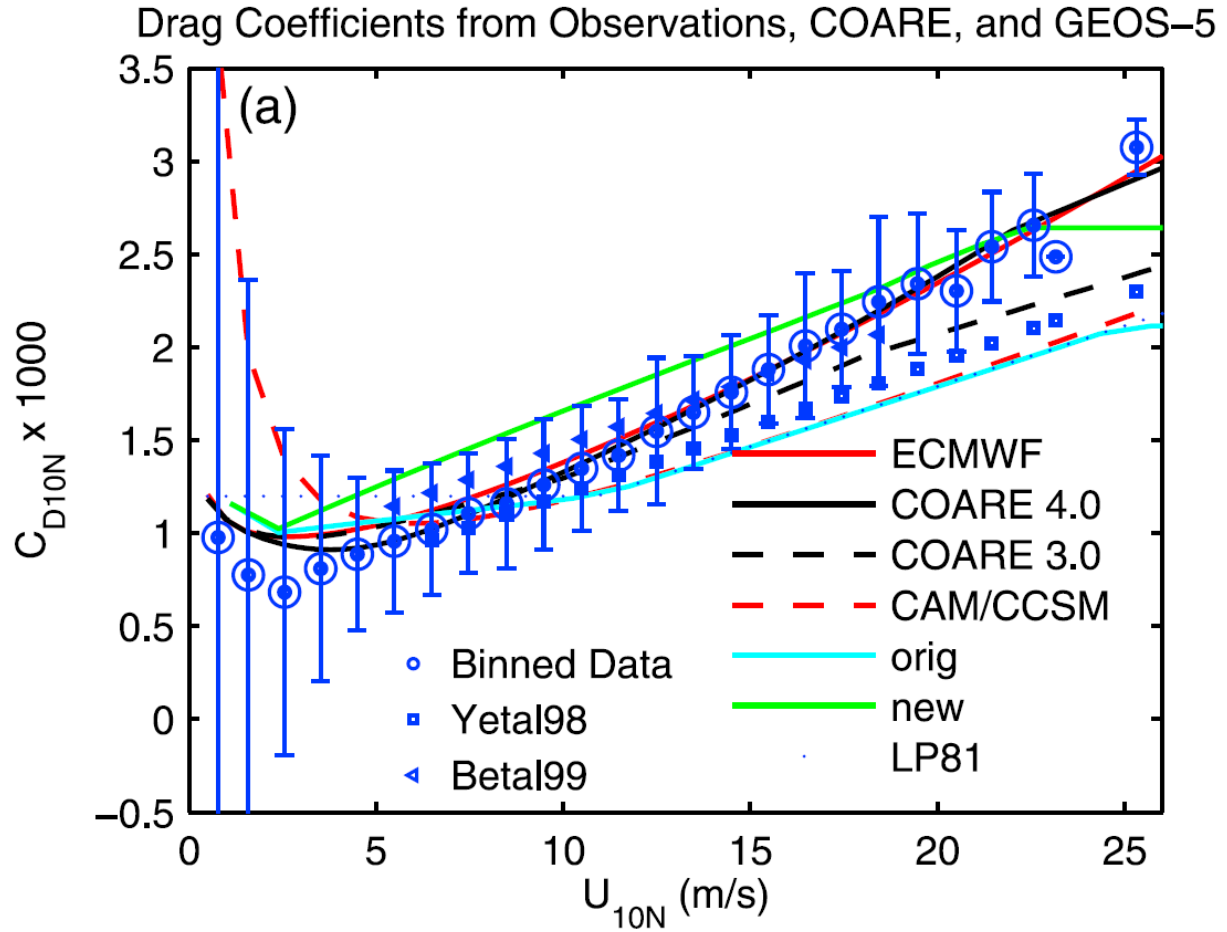


Figure 5.6: From Garfinkel et al. (2011), relation of the drag coefficient ($C_{D10N} \times 1000$) and wind speed (U_{10N}) between various heat flux algorithms.

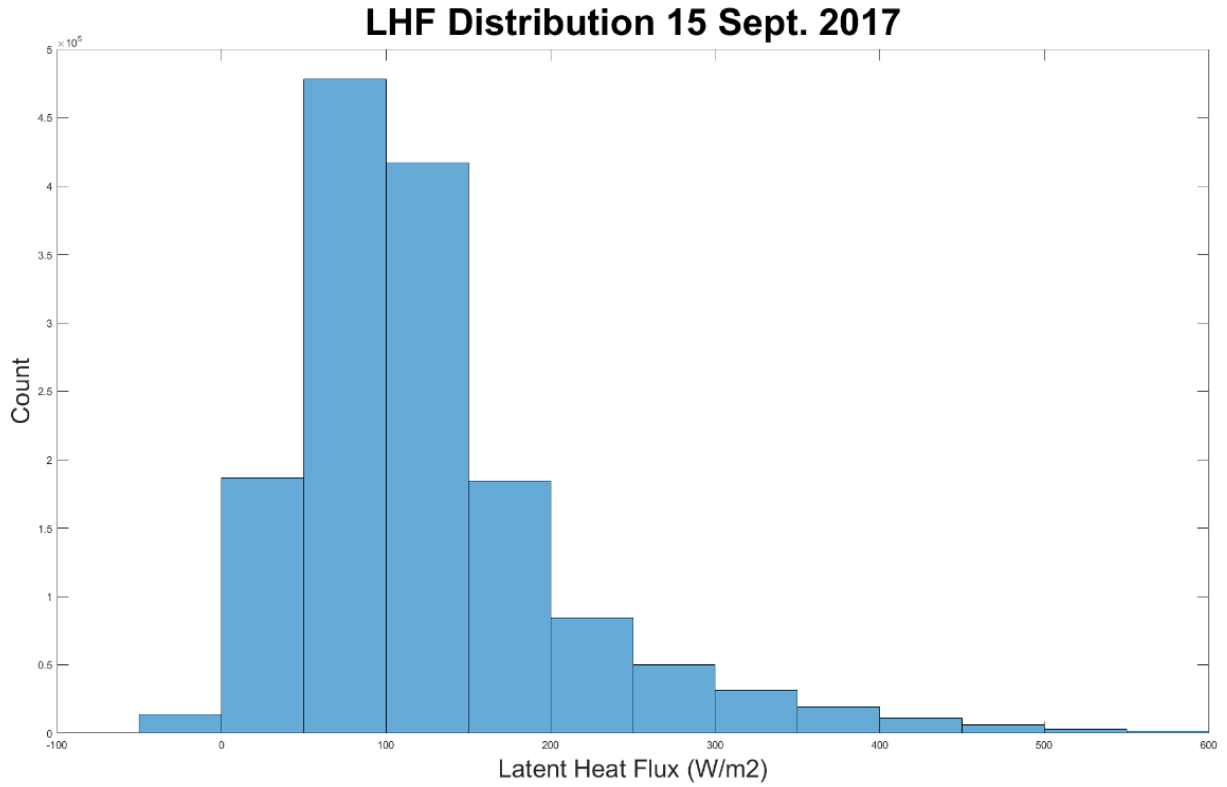


Figure 5.7: Distribution of latent heat flux estimates (W/m^2) across an entire day (15 Sept 2017), with bins of 50 W/m^2 .

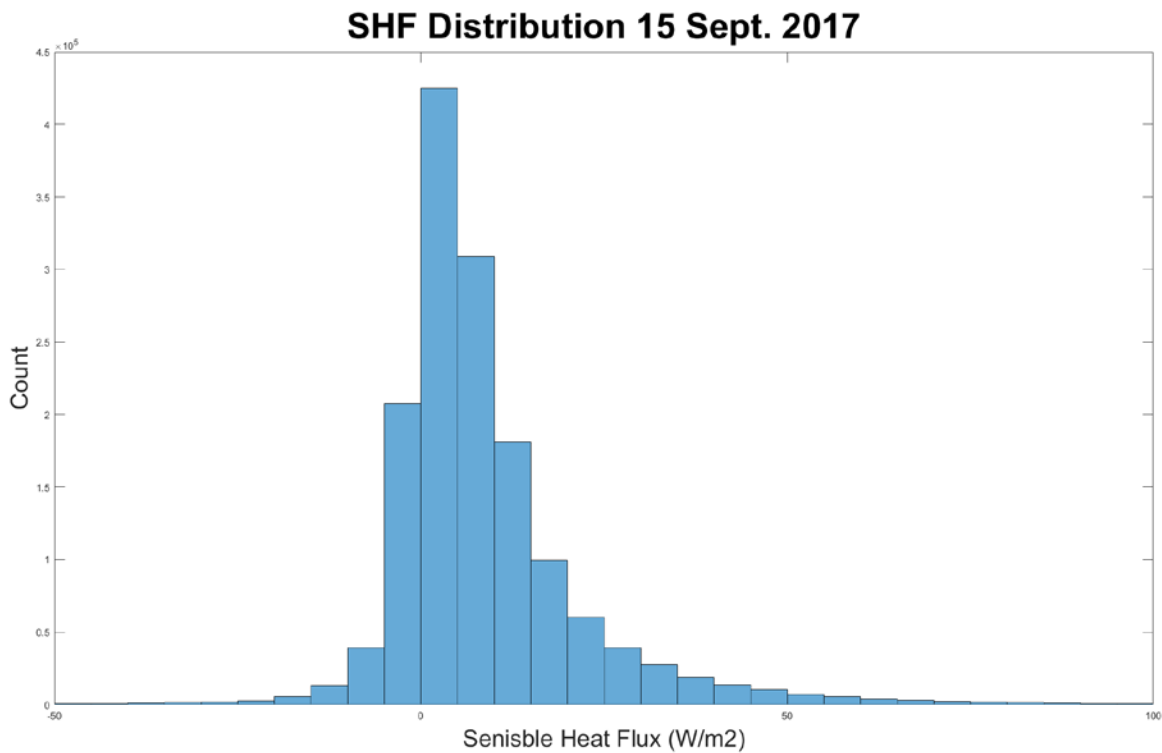


Figure 5.8: Same as Figure 5.7, but with sensible heat flux (W/m^2) with bins of 10 W/m^2 .

Chapter 6: Conclusions

6.1 Summary of Thesis

Throughout this thesis, we have seen the importance of being able to observe Extratropical Cyclones (ETCs) as these systems have a large-scale impact on Earth's weather and climate. As discussed in the introduction, the community has developed a good understanding of ETC development at the synoptic scale thanks to the Norwegian Cyclone Model and Shapiro-Keyser Cyclone Model. Recent studies have highlighted how ETCs can develop at the smaller mesoscale level thanks to significant progress from field campaigns and modelling studies, but there are still some uncertainties with how ETCs interact with the surface, especially when they develop over the oceans where observations are limited. New satellite technology over the last two decades have allowed us to explore in detail the interiors of marine-based ETCs and improve our knowledge of how they interact with the surface.

Chapter 2 focused on a case study of a marine-based extratropical cyclone that was observed multiple times by the Afternoon-Train (A-Train) satellite constellation, which offered a unique perspective of ETC development. While MODIS imagery made it seem like this was a typical ETC based on its cloud shield structure, CloudSat revealed the unique structural evolution within its warm front. As seen in Fig. 2.5, the warm front transitioned from a relatively stable and stratiform structure to unstable and convective within a 36-hour period. Given that there were no CloudSat observations of the warm front during the apart transition, it is difficult to conclude as to

why this transition occurred. However, one of the hypothesis that emerged from this case study was the possible influence of surface heat fluxes.

As discussed in Chapters 1 and 3, surface heat fluxes play a large role in ETC development, especially as they form over warm-moist ocean surfaces near cold-dry continental air masses. Large heat fluxes were associated with our late November 2006 case study as this ETC developed near the US east coast, with combined heat flux values exceeding 800 W/m^2 . However, as this cyclone moved poleward, these surface heat fluxes near the coast diminished around the same time when we would have expected the warm front to transition into a convective structure (23-24 November). Though these surface heat fluxes decreased, there was a noticeable increase in latent heat fluxes ahead of the warm front on 23 November (Fig. 3.1), which could have introduced some instability near the surface in this region. While this instability might have led to the convective transition observed within the warm front, we can only definitely state that this was more of a correlation, as future modelling studies are needed in order to state if these surface heat fluxes ahead of the warm front led to its stratiform-to-convective transition.

Given the importance of surface heat fluxes over the oceans and their impact on extratropical cyclones and other weather phenomenon, it is important to be able to estimate these from spaceborne instruments, as in situ measurements are limited over the ocean surfaces. However, at the time of writing this thesis, currently no spaceborne instruments can directly measure surface heat fluxes. Though we can estimate these fluxes using estimates of temperature, specific humidity, and wind speed from other instruments, these observations can be limited in presence of precipitation, which could lead to inaccuracies in latent and sensible heat fluxes. Additionally, these polar orbiting satellites can miss large portions in the tropical and sub-tropical regions, which can cause them to miss key features in weather systems that feature large surface

heat fluxes, like those discussed in Chapter 3. This is where we can use CYGNSS for surface heat flux estimates, as CYGNSS can not only provide improved wind speeds in nearly all weather conditions, but offers continuous coverage up to the 38th parallel in both hemispheres. This improved coverage could give us better estimates of surface heat fluxes, especially those associated with extratropical cyclones that develop in the lower-latitudes.

Given that CYGNSS is a tropical satellite mission, one would not expect it to be able to observe extratropical cyclones. Despite its mission and orbit, the constellation orbits at a 35° inclination, and with its antenna field of view, it can make continuous observations up to 38° in both hemispheres. As Chapter 4 showed by taking 2 years of ETC center and front locations, as well as simulated CYGNSS specular point locations for the same amount of time, we can see that CYGNSS is expected to make a significant amount of ETC observations. A majority of these observations should be coming from the Western Atlantic and Western Pacific Oceans in the Northern Hemisphere. This is mainly due to the influence from the Gulf Stream and Kuroshio Currents (respectively), as both transport warm water poleward parallel to continents that are cold and dry during the winter season. The interactions here provide ideal basins for extratropical cyclogenesis, as they can be a source of surface sensible and latent heat fluxes that can provide energy for these ETCs to develop and evolve.

By using surface winds from CYGNSS and temperature, specific humidity, and air density from MERRA-2, we can estimate surface sensible and latent heat fluxes along CYGNSS's track using the COARE 3.5 algorithm, as discussed in Chapter 5. While there is still some noise from the CYGNSS observations, which then produce noise in our SHF and LHF estimates, overall we still get reasonable results of surface heat fluxes from CYGNSS. We can see this with the surface heat flux observations around the ETCs on 21 March and 30 October 2017, as CYGNSS showed

large heat flux values associated with these systems as they developed and strengthened on their respective days. Correlating with previous studies, we see how strong heat fluxes are associated with extratropical cyclones as they develop over warm ocean surfaces near cold continental air masses. Though we can observe this relation, we cannot quantitatively state how much of a direct impact these surface heat fluxes had on the formation and evolution of these ETCs. Future modelling work is necessary to formally define this relation and the causation of this correlation.

While CYGNSS offers decent surface heat flux estimates when observed at a larger scale, there is still some noise and variations in these estimates. By comparing CYGNSS SHF and LHF estimates to those estimated by the KEO buoy and MERRA-2, we can see that there is some variation in the CYGNSS observations, with many of them coming from the variations in wind speed estimates from CYGNSS (Tables 5.1 and 5.2). Additionally, we see through the sensitivity analysis how variations in our inputs could influence our surface heat flux estimates. As wind speed estimates from CYGNSS continue to improve, we would expect this to trickle down into our surface heat flux estimates along CYGNSS's tracks. Even as CYGNSS surface wind speed observations improve, we need to take into account the variations from the inputs, like temperature, humidity, and wind speed, as these inaccuracies could lead to variations to our surface heat flux estimates (Table 5.3). While some of these variations are outside of our control, they still need to be considered when estimating sensible and latent heat fluxes.

6.2 Future Work

Given the importance of surface heat fluxes and CYGNSS's improved observational capability, the first main step beyond this thesis is to develop a surface heat flux Level-2 product for the entire CYGNSS mission. This would be completed using the same COARE 3.5 algorithm

presented in Chapter 5 (or any updated versions that are developed in the future). While MERRA-2 data has been useful in the analysis presented in this thesis, it may not suffice if we were to develop an L2 product for CYGNSS given the time lag (data for each month is released 2-3 weeks after the month has ended). As a result, we will need to use a different dataset for the thermodynamic variables (temperature, humidity) with a shorter time lag. One such dataset could be the SeaFluxCDR product, which will provide these variables every three hours across the global oceans. While the temporal resolution could present some issues compared to the MERRA-2 reanalysis data currently being used, it will allow us to develop this product at a faster rate so that the general scientific community can use it.

As part of this product development for CYGNSS, we would need to perform a calibration and validation of the product using direct latent and sensible heat flux in-situ measurements. We plan to do this using various field campaigns set to take place within the next two years, such as Propagation of Intra-Seasonal Tropical Oscillations (PISTON), Cloud, Aerosol and Monsoon Processes Philippines Experiment (CAMP²Ex), and Years of the Maritime Continent (YMC). We can also compare these fluxes to fluxes estimated by other buoys, such as the National Data Buoy Center (NDBC), in between field campaigns. We would also be able to expand beyond the simple sensitivity analysis presented in Chapter 5 as we continue to receive newer and improved data from CYGNSS. By creating this product and accurately validating it, it will allow us to offer better analysis of surface heat fluxes within and around extratropical cyclones that form in the lower latitudes. Additionally, we can apply this same product and algorithm to better analyze tropical cyclones, the Madden-Julien Oscillation, and other tropical convection observed by CYGNSS.

Though we have shown that CYGNSS can observe extratropical cyclones that form in the lower latitudes, we would also like to perform an overall composite analysis of its extratropical

sampling as a way to confirm the results presented in Chapter 4 of this thesis. Along with focusing on a few case studies, this composite analysis will process the first two years of CYGNSS data for all ETC centers and fronts observed by the mission. We can use this data, combined with analysis from the Global Precipitation Mission (GPM) and A-Train, to examine differences in frontal winds, clouds, and precipitation across storms and fronts between the Northern and Southern Hemispheres (c.f., Naud et al. 2012), paying particular attention to the cyclone initiation regions east of the Northern Hemisphere continents. Specifically, the ETC and CYGNSS data will allow us to investigate the conditions in the early stages of extratropical cyclones that may influence moist processes, latent heat release, and ultimately significant intensification of the cyclones.

As discussed throughout this thesis, observations of temperature and humidity must come from other sources in order to estimate latent and sensible heat fluxes, as CYGNSS provides surface wind speed observations. While future missions, like the Time-Resolved Observations of Precipitation structure and storm Intensity with a Constellation of Smallsats (TROPICS), could fill in some of these gaps, the timelines for both missions do not have much overlap compared to a combined mission. However, if a follow-on mission to CYGNSS were to launch in the future, it could help fill in some of these gaps with if it provides observations of temperature and specific humidity. This satellite would need to provide temperature and humidity both at the surface and at 10-meters in order to estimate the fluxes. Additionally, a follow-on mission with a higher orbit inclination ($\sim 50^\circ$ - 60°) would be able to observe a larger number of extratropical cyclones that form in the midlatitudes.

As discussed in Chapter 3, there was a definite correlation between high surface heat fluxes and extratropical cyclone development; however, this was not able to conclude how much of an influence surface fluxes had on the development of the ETC as it was only based on the limited

observations available. By developing a three-dimensional modelling study, one could look at how these surface fluxes might have played a role in not only the overall develop of the ETC, but as well as the stratiform-to-convective transition observed within the warm front featured in Chapter 2. This modelling study would do this by varying difference in temperature and humidity between the surface and 10 meters, along with the winds at the surface, near the area where the warm front transition occurred that correlated with high surface fluxes. This would not only allow one to see how fluxes vary as temperature, humidity, and wind speed change, but how these might have impacted the development of this extratropical cyclone and its warm front. By using the initial observations from CloudSat and the thermodynamic profiles from ECMWF (Figure 2.5), one could calculate the fluxes needed over a period of time to make the atmosphere near the surface unstable in order to reach the instability observed by CloudSat.

6.3 Importance of Thesis

While CYGNSS is a tropical satellite mission, we have shown that it can observe extratropical cyclones as they develop in the lower latitudes. Most of CYGNSS's extratropical observations are heavily focused on the equatorward side of these cyclones, but as the results have shown, these are areas of high surface heat fluxes that can strengthen ETCs and introduce instability and convection. By using improved wind speeds from CYGNSS, we can get better estimates and coverage of these surface heat fluxes within and around low-latitude ETCs, which will lead to a better understanding of how surface processes play a role in extratropical cyclone development.

Throughout this thesis, we utilized CYGNSS's capabilities beyond its original mission. While the surface heat flux results are not perfect, we believe that this work sets the foundation for

future milestones that we hope are accomplished by the scientific community in the near future. One such milestone is the ability to use GNSS-R and CYGNSS like technologies in a polar orbiting constellation in order to have a better understanding of the surface processes that are involved with nearly all extratropical cyclones, not just those that develop in the lower-latitudes. Additionally, it is our hope that we will soon have the capability of estimate surface heat fluxes from space in all weather conditions. While we may never see direct heat flux measurements from spaceborne instruments, the work presented here shows the importance of being able to estimates heat fluxes from a remote sensing platform. This would require improved estimates of temperature and specific humidity from space as well. While there are some satellites missions currently planned to address these gaps (such as TROPICS), we still lack the ability to accurately estimate these fluxes from one satellite mission. It is the hope of the author that this thesis sets the foundation for the continued advancement of surface heat flux estimates and the overall advancement of the scientific community.

References

- Barnes, W. L., T. S. Pagano, and V. V. Salomonson, 1998: Prelaunch characteristics of the moderate resolution imaging Spectroradiometer (MODIS) on EOS-AM1. *IEEE Trans. Geosci. Remote Sens.*, **36**, 1088-1100.
- Bauer M. and A. D. Del Genio, 2006: Composite analysis of winter cyclones in a GCM: influence of climatological humidity. *J. Climate*, **19**, 1652-1672, doi:10.1175/JCLI3690.1.
- Bauer, M., G. Tselioudis and W. B. Rossow, 2016: A new climatology for investigating storm influences in and on the extratropics. *J. Appl. Meteorol. Climatol.*, **55**, 1287-1303, doi:10.1175/JAMC-D-15-0245.1.
- Beljaars, A. C. M., and A. A. M. Holtslag, 1991: Flux parameterization over land surfaces for atmospheric models. *J. Appl. Meteor.*, **30**, 327–341.
- Bender, F., V. Ramanathan, and G. Tselioudis, 2012: Changes in extratropical storm track cloudiness 1983–2008: observational support for a poleward shift. *Climate Dyn.*, **38**, 2037–2053, doi:10.1007/s00382-011-1065-6.
- Bennartz R., and P. Bauer, 2003: Sensitivity of microwave radiances at 85–183 GHz to precipitating ice particles, *Radio Sci.*, **38** (4), 8075, doi:10.1029/2002RS002626.
- Bennartz, R., and G. W. Petty, 2001: The sensitivity of microwave remote sensing observations of precipitation to ice particle size distributions. *J. Appl. Meteorol.*, **40**, 345-364.
- Berry, G., M. J. Reeder, and C. Jakob, 2011: A global climatology of atmospheric fronts. *Geophys. Res. Lett.*, **38**, doi:201110.1029/2010GL046451.
- Bjerknes, J. and H. Solberg, 1922: Life cycle of cyclones and the polar front theory of atmospheric circulation. *Geofys. Publ.* **3**, 1–18.
- Bjerknes, J., 1919: On the structure of moving cyclones. *Mon. Wea. Rev.*, **47**, 95–99.
- Boutle, I. A., S. E. Belcher, and R. S. Plant, 2011: Moisture transport in midlatitude cyclones. *Quart. J. Roy. Meteor. Soc.*, **137**, 360–373.
- Browning, K. A., 1986: Conceptual models of precipitation systems. *Wea. Forecasting*, **1**, 23-41, doi:10.1175/1520-0434(1986)001,0023:CMOPS.2.0.CO;2.
- Browning, K. A., 1990: Organization of clouds and precipitation in extratropical cyclones. *Extratropical Cyclones: The Erik Palmén Memorial Volume*, C. W. Newton and E.O. Holopainen, Eds., Amer. Meteor. Soc., 129–153.

- Browning, K. A., M. E. Hardman, T. W. Harrold, and C. W. Pardoe, 1973: Structure of rainbands within a mid-latitude depression. *Quart. J. Roy. Met. Soc.*, **99**, 215-231, doi:10.1002/qj.49709942002.
- Businger, S., T. M. Graziano, M. L. Kaplan, and R. A. Rozumalski, 2005: Cold-air cyclogenesis along the Gulf-Stream front: investigation of diabatic impacts on cyclone development, frontal structure, and track. *Meteor. Atmos. Phys.*, **88**, 65-90.
- Carlson, T.N., 1980: Airflow through midlatitude cyclones and the comma cloud pattern. *Mon. Wea. Rev.*, **108**, 1498-1509, doi:10.1175/1520-0493(1980)108,1498:ATMCAT.2.0.CO;2.
- Catto J. L., C. Jakob, G. Berry and N. Nicholls, 2012: Relating global precipitation to atmospheric fronts. *Geophys. Res. Lett.*, **39**, L10805, doi:10.1029/2012GL051736.
- Catto, J. L., 2016: Extratropical cyclone classification and its use in climate studies. *Rev. Geophys.* **54**, 486–520, doi: 10.1002/2016RG000519.
- Chagnon J. M., S. L. Gray, J. Methven, 2013: Diabatic processes modifying potential vorticity in a North Atlantic cyclone. *Quart. J. Roy. Meteor. Soc.*, **139**, 1270–1282. DOI:10.1002/qj.2037
- Cione, J. J., S. Raman, and L. J. Pietrafesa, 1993: The Effect of Gulf Stream-induced Baroclinicity on U.S. East Coast Winter Cyclones. *Mon. Wea. Rev.*, **121**, 421–430.
- Crespo, J. A., and D. J. Posselt, 2016: A-Train Based Case Study of Stratiform - Convective Transition within a Warm Conveyor Belt, *Mon. Wea. Rev.*, **144**, 2069–2084, doi: 10.1175/MWR-D-15-0435.1. ©American Meteorological Society. Used with permission.
- Crespo, J.A., D.J. Posselt, C.M. Naud, and C.D. Bussy-Virat, 2017: Assessing CYGNSS's Potential to Observe Extratropical Fronts and Cyclones. *J. Appl. Meteorol. Climatol.*, **56**, 2027-2034, doi:10.1175/JAMC-D-17-0050.1. ©American Meteorological Society. Used with permission.
- Crosier, J., T. W. Choullarton, C. D. Westbrook, A. M. Blyth, K. N. Bower, P. J. Connolly, C. Dearden, M. W. Gallagher, Z. Cui, and J. C. Nicol, 2014: Microphysical properties of cold frontal rainbands. *Quart. J. Roy. Meteor. Soc.*, **140**: 1257–1268. doi: 10.1002/qj.2206
- Davis, C. A., 1992: A potential vorticity analysis of the importance of initial structure and condensational heating in observed cyclogenesis. *Mon. Wea. Rev.*, **120**, 2409-2428.
- Dearden, C., G. Vaughan, T. Tsai, and J. Chen, 2016: Exploring the diabatic role of ice microphysical processes in two North Atlantic summer cyclones. *Mon. Wea. Rev.* doi:10.1175/MWR-D-15-0253.1, **in press**.
- Dearden, C., P. J. Connolly, G. Lloyd, J. Crosier, K. N. Bower, T. W. Choullarton, and G. Vaughan, 2014: Diabatic Heating and Cooling Rates Derived from In Situ Microphysics Measurements: A Case Study of a Wintertime U.K. Cold Front. *Mon. Wea. Rev.*, **142**, 3100–3125. doi: http://dx.doi.org/10.1175/MWR-D-14-00048.1

- Eckhardt, S., A. Stohl, H. Wernli, P. James, C. Forster, and N. Spichtinger, 2004: A 15-Year Climatology of Warm Conveyor Belts. *J. Climate*, **17**, 218-237, doi:10.1175/1520-0442(2004)017,0218:AYCOWC.2.0.CO;2.
- Edson, J., V. Jampana, R. Weller, S. Bigorre, A. Plueddemann, C. Fairall, S. Miller, L. Mahrt, D. Vickers, and H. Hersbach, 2013: On the exchange of momentum over the open ocean, *J. Phys. Oceanogr.*, **43**, 1589–1610, doi:10.1175/JPO-D-12-0173.1.
- Evans, M. S., D. Keyser, L. F. Bosart, and G. M. Lackmann, 1994: A satellite-derived classification scheme for rapid maritime cyclogenesis. *Mon. Wea. Rev.*, **122**, 1381–1416.
- Fairall, C. W., A. B. White, J. B. Edson, and J. E. Hare, 1997: Integrated shipboard measurements of the marine boundary layer. *J. Atmos. Oceanic Technol.*, **14**, 338-359.
- Fairall, C. W., Bradley, E. F., Hare, J. E., Grachev, A. A., and Edson, J. B., 2003: Bulk parameterization of Air-sea Fluxes: Updates and Verification for the COARE Algorithm, *J. Climate*, **16**, 571–591.
- Fairall, C. W., E. F. Bradley, D. P. Rogers, J. B. Edson, and G. S. Young, 1996: Bulk Parameterization of Air–sea Fluxes for Tropical Ocean–Global Atmosphere Coupled Ocean–Atmosphere Response Experiment. *J. Geophys. Res.*, **101**, 3747–3764.
- Field P. R., A. Gettelman, R. B. Neale, R. Wood, P. J. Rasch and H. Morrison, 2008: Cyclone compositing to constrain climate model behavior using satellite observations. *J. Climate*, **21**, 5887-5903.
- Field, P. R., and R. Wood, 2007: Precipitation and cloud structure in midlatitude cyclones. *J. Climate*, **20**, 233-254.
- Flaounas, E., K. Lagouvardos, V. Kotroni, C. Claud, J. Delanoë, C. Flamant, E. Madonna, and H. Wernli, 2015: Processes leading to heavy precipitation associated with two Mediterranean cyclones observed during the HyMeX SOP1, *Quart. J. Roy. Meteor. Soc.*, doi:10.1002/qj.2618.
- Garfinkel, C.I., A. Molod, L. D. Oman and I.-S. Song, 2011: Improvement of the GEOS-5 AGCM upon Updating the Air-Sea Roughness Parameterization. *Geophys. Res. Lett.*, **38**, L18702, doi:10.1029/2011GL048802.
- Gelaro, R., W. McCarty, M.J. Suárez, R. Todling, A. Molod, L. Takacs, C.A. Randles, A. Darmenov, M.G. Bosilovich, R. Reichle, K. Wargan, L. Coy, R. Cullather, C. Draper, S. Akella, V. Buchard, A. Conaty, A.M. da Silva, W. Gu, G. Kim, R. Koster, R. Lucchesi, D. Merkova, J.E. Nielsen, G. Partyka, S. Pawson, W. Putman, M. Rienecker, S.D. Schubert, M. Sienkiewicz, and B. Zhao, 2017: The Modern-Era Retrospective Analysis for Research and Applications, Version 2 (MERRA-2). *J. Climate*, **30**, 5419–5454.
- Govekar, P. D., C. Jakob, and J. L. Catto, 2014: The relationship between clouds and dynamics in Southern Hemisphere extratropical cyclones in the real world and a climate model, *J. Geophys. Res. Atmos.*, **119**, 6609-6628, DOI:10.1002/2013JD020699.

- Govekar, P. D., C. Jakob, M. J. Reeder, and J. Haynes, 2011: The three-dimensional distribution of clouds around Southern Hemisphere extratropical cyclones, *Geophys. Res. Lett.*, **38**, L21805, doi:10.1029/2011GL049091.
- Graf, M. A., H. Wernli, and M. Sprenger, 2017: Objective classification of extratropical cyclogenesis. *Quart. J. Roy. Meteor. Soc.*, **143**, 1047–1061, doi:10.1002/qj.2989.
- Grams, C. M., and Coauthors, 2011: The key role of diabatic processes in modifying the upper-tropospheric wave guide: A North Atlantic case-study. *Quart. J. Roy. Meteor. Soc.*, **137**, 2174–2193.
- Harrold, T. W., 1973: Mechanisms influencing the distribution of precipitation within baroclinic disturbances. *Quart. J. Roy. Meteor. Soc.*, **99**, 232–251, doi:10.1002/qj.49709942003.
- Hartmann, D. L., 1994: *Global Physical Climatology*. Academic Press, 411 pp.
- Hawcroft M., L. Shaffrey, K. Hodges, H. Dacre, 2012: How much northern hemisphere precipitation is associated with extratropical cyclones? *Geophys. Res. Lett.*, **39**, L24809, doi:10.1029/2012GL053866
- Heideman, K. F., and J. M. Fritsch, 1988: Forcing mechanisms and other characteristics of significant summertime precipitation. *Wea. Forecasting*, **3**, 115–130, doi:10.1175/1520-0434(1988)003<0115:FMAOCO.2.0.CO;2.
- Hewson, T. D., 1998: Objective fronts. *Meteor. Appl.*, **5**, 37–65.
- Hoskins, B. and K. Hodges, 2002: New Perspectives on the Northern Hemisphere Winter Storm Tracks. *J. Atmos. Sci.*, **59**, 1041–1061, doi:10.1175/1520-0469(2002)059<1041:NPOTNH>2.0.CO;2
- Hoskins, B. and K. Hodges, 2005: A New Perspective on Southern Hemisphere Storm Tracks. *J. Climate*, **18**, 4108–4129, doi: 10.1175/JCLI3570.1.
- Hoskins, B.J. and N.V. West, 1979: Baroclinic waves and frontogenesis. Part II: Uniform potential vorticity jet flows—cold and warm fronts. *J. Atmos. Sci.*, **36**, 1663–1680.
- Igel, A. L., and S. C. van den Heever, 2014: The role of latent heating in warm frontogenesis. *Quart. J. Roy. Meteor. Soc.*, **140**, 139–150.
- Joos, H., and H. Wernli, 2012: Influence of microphysical processes on the potential vorticity development in a warm conveyor belt: A case-study with the limited-area model COSMO. *Quart. J. Roy. Meteor. Soc.*, **138**, 407–418.
- Kawanishi, T., T. Sezai, Y. Ito, K. Imaoka, T. Takeshima, Y. Ishido, A. Shibata, M. Miura, H. Inahata, and R.W. Spenser, 2003: The advanced microwave scanning radiometer for earth observing system (AMSR-E), NASDA's contribution to the EOS for global energy and water cycle studies. *IEEE Trans. Geosci. Remote Sens.*, **41**, 184–194.

- Keyser, D., B.D. Schmidt, and D.G. Duffy, 1989: A technique for representing three-dimensional vertical circulations in baroclinic disturbances. *Mon. Wea. Rev.*, **117**, 2463-2494.
- King, M. D., W. P. Menzel, Y. J. Kaufman, D. Tanré, B. C. Gao, S. Platnick, S. A. Ackerman, L. A. Remer, R. Pincus, and P. A. Hubanks, 2003: Cloud and Aerosol Properties, Precipitable Water, and Profiles of Temperature and Water Vapor from MODIS. *IEEE Trans. Geosci. Remote Sens.*, **41**, 442-458.
- Klein, S. A. and C. Jakob, 1999: Sensitivities of frontal clouds simulated by the ECMWF model. *Mon. Wea. Rev.*, **127**, 2514-2531.
- Kulie, M. S., R. Bennartz, T. J. Greenwald, Y. Chen, and F. Z. Weng, 2010: Uncertainties in Microwave Properties of Frozen Precipitation Implications for Remote Sensing and Data Assimilation. *J Atmos Sci*, **67**, 3471-3487.
- Kuo, Y.-H., M. A. Shapiro, and E. G. Donall, 1991: The interaction between baroclinic and diabatic processes in a numerical simulation of a rapidly intensifying extratropical marine cyclone. *Mon. Wea. Rev.*, **119**, 368-384.
- Lau, N.-C., and M. W. Crane, 1995: A satellite view of the synoptic-scale organization of cloud properties in midlatitude and tropical circulation systems. *Mon. Wea. Rev.*, **123**, 1984-2006.
- Lau, N.-C., and M. W. Crane, 1997: Comparing satellite and surface observations of cloud patterns in synoptic-scale circulation systems. *Mon. Wea. Rev.*, **125**, 3172-3189.
- Lloyd, G., C. Dearden, T. W. Choullarton, J. Crosier, and K. N. Bower, 2014: Observations of the Origin and Distribution of Ice in Cold, Warm, and Occluded Frontal Systems during the DIAMET Campaign. *Mon. Wea. Rev.*, **142**, 4230-4255. doi: <http://dx.doi.org/10.1175/MWR-D-13-00396.1>.
- Madonna, E., H. Wernli, H. Joos, and O. Martius, 2014: Warm conveyor belts in the ERA-Interim Dataset (1979–2010). Part I: Climatology and Potential Vorticity Evolution. *J. Climate*, **27**, 3–26, doi:10.1175/JCLI-D-12-00720.1.
- Martinez-Alvarado, O., H. Joos, J. Chagnon, M. Boettcher, S. Gray, B. Plant, J. Methven, and H. Wernli, 2013: The dichotomous structure of the warm conveyor belt. *Quart. J. Roy. Meteor. Soc.*, **140**, 1809-1824, doi:10.1002/qj.2276.
- Massacand, A. C., H. Wernli, and H. C. Davies, 2001: Influence of upstream diabatic heating upon an alpine event of heavy precipitation. *Mon. Wea. Rev.*, **129**, 2822–2828.
- Methven, J., 2015: Potential vorticity in warm conveyor belt outflow. *Quart. J. Roy. Meteor. Soc.*, **141**, 1065–1071. doi: 10.1002/qj.2393.
- Molod, A., Takacs, L., Suarez, M., and Bacmeister, J., 2015: Development of the GEOS-5 atmospheric general circulation model: evolution from MERRA to MERRA2, *Geosci. Model Dev.*, **8**, 1339-1356, doi:10.5194/gmd-8-1339-2015.

- Naud C. M. and B. H. Kahn, 2015: Thermodynamic phase and ice cloud properties in northern hemisphere winter extratropical cyclones observed by Aqua AIRS. *J. Appl. Meteorol. Climatol.*, **54**, 2283-2303, doi:10.1175/JAMC-D-15-0045.1.
- Naud C. M., A. D. Del Genio and M. Bauer, 2006: Observational constraints on cloud thermodynamic phase in midlatitude storms. *J. Climate*, **19**, 5273-5288.
- Naud C. M., D. J. Posselt, and S. C. van den Heever, 2012: Observational analysis of cloud and precipitation in midlatitude cyclones: northern versus southern hemisphere warm fronts, *J. Climate*, **25**, 5135-5151, doi:10.1175/JCLI-D-11-00569.1.
- Naud C. M., D. J. Posselt, and S. C. van den Heever, 2015: A CloudSat-CALIPSO view of cloud and precipitation properties across cold fronts over the global oceans. *J. Climate*, **28**, 6743-6762, doi:10.1175/JCLI-D-15-0052.1.
- Naud, C. M., J. F. Booth, and A. D. Del Genio, 2014: Evaluation of ERA-interim and MERRA cloudiness in the Southern Ocean. *J. Climate*, **27**, 2109-2124, doi:10.1175/JCLI-D-13-00432.1.
- Naud, C.M., A. D. Del Genio, M. Bauer, and W. Kovari, 2010: Cloud vertical distribution across warm and cold fronts in CloudSat-CALIPSO data and a general circulation model. *J. Climate*, **23**, 3397-3415, doi:10.1175/2010JCLI3282.1.
- Naud, C.M., J.F. Booth, and A.D. Del Genio, 2016: The relationship between boundary layer stability and cloud cover in the post-cold frontal region. *J. Climate*, **29**, 8129-8149, doi:10.1175/JCLI-D-15-0700.1.
- Neiman, P.J. and M.A. Shapiro, 1993: The life cycle of an extratropical marine cyclone. Part I: Frontal-cyclone evolution and thermodynamic air-sea interaction. *Mon. Wea. Rev.*, **121**, 2153-2176, doi:10.1175/1520-0493(1993)121,2153:TLCOAE.2.0.CO;2.
- Oort, A. H., 1971: The observed annual cycle in the meridional transport of atmospheric energy. *J. Atmos. Sci.*, **28**, 325–339.
- Parkinson, C. L., 2003: Aqua: an earth-observing satellite mission examine water and other climate variables. *IEEE Trans. Geosci. Remote Sens.*, **41**, 173-183.
- Petty, G. W., 1994: Physical retrievals of over-ocean rain rate from multichannel microwave imagery. Part 1: Theoretical characteristics of normalized polarization and scattering indexes. *Meteor. Atmos. Phys.*, **54**, 79-99.
- Pfahl, S. E. Madonna, M. Boettcher, H. Joos, and H. Wernli, 2014: Warm Conveyor Belts in the ERA-Interim Dataset (1979–2010). Part II: Moisture Origin and Relevance for Precipitation. *J. Climate*, **27**, 27–40, doi:10.1175/JCLI-D-13-00223.1.
- Pomroy, H. R., and A. J. Thorpe, 2000: The evolution and dynamical role of reduced upper-tropospheric potential vorticity in intensive observing period one of FASTEX. *Mon. Wea. Rev.*, **128**, 1817–1834.

- Posselt, D. J., A. R. Jongeward, C.-Y. Hsu, and G. L. Potter, 2012: Object-Based Evaluation of MERRA-Simulated Cloud Physical Properties and Radiative Fluxes during the 1998 El Nino - La Nina Transition. *J. Climate*, **25**, 7313-7327, doi: 10.1175/JCLI-D-11-00724.1.
- Posselt, D. J., and J. E. Martin, 2004: The Effect of Latent Heat Release on the Evolution of a Warm Occluded Thermal Structure. *Mon. Wea. Rev.*, **132**, 578-599.
- Posselt, D. J., G. L. Stephens, and M. Miller, 2008: CloudSat: Adding a New Dimension to a Classical View of Extratropical Cyclones. *Bull. Amer. Meteor. Soc.*, **89**, 599-609.
- Reed, R. J., A. J. Simmons, M. D. Albright, and P. Uden, 1988: The role of latent heat release in explosive cyclogenesis: Three examples based on ECMWF operational forecasts. *Wea. Forecasting*, **3**, 217-229.
- Reed, R.J. and F. Sanders, 1953: An Investigation of the Development of a Mid-Tropospheric Frontal Zone and its Associated Vorticity Field. *J. Meteor.*, **10**, 338-349.
- Reeves, H. D., and G. M. Lackmann, 2004: An Investigation of the Influence of Latent Heat Release on Cold-Frontal Motion. *Mon. Wea. Rev.*, **132**, 2864-2881.
- Rienecker M. M., M. J. Suarez, R. Gelaro, R. Todling, J. Bacmeister, E. Liu, M. G. Bolisovich, S. D. Schubert, L. Takacs, G.-K. Kim, S. Bloom, J. Chen, D. Collins, A. Conaty, A. Da Silva, W. Gu, J. Joiner, R. D. Koster, R. Lucchesi, A. Molod, T. Owens, S. Pawson, P. Pegion, C. R. Redder, R. Reichle, F. R. Robertson, A. G. Ruddick, M. Sienkiewicz and J. Woollen, 2011: MERRA: NASA's Modern Era Retrospective analysis for Research and Applications. *J. Climate*, **24**, 3624-3648, doi: 10.1175/JCLI-D-11-00015.1.
- Rienecker M. M., M. J. Suarez, R. Gelaro, R. Todling, J. Bacmeister, E. Liu, M. G. Bolisovich, S. D. Schubert, L. Takacs, G.-K. Kim, S. Bloom, J. Chen, D. Collins, A. Conaty, A. Da Silva, W. Gu, J. Joiner, R. D. Koster, R. Lucchesi, A. Molod, T. Owens, S. Pawson, P. Pegion, C. R. Redder, R. Reichle, F. R. Robertson, A. G. Ruddick, M. Sienkiewicz and J. Woollen, 2011: MERRA: NASA's Modern Era Retrospective analysis for Research and Applications. *J. Climate*, **24**, 3624-3648.
- Ruf, C., A. Lyons, M. Unwin, J. Dickinson, R. Rose, D. Rose and M. Vincent, 2013: CYGNSS: Enabling the Future of Hurricane Prediction, *IEEE Geosci. Remote Sens. Mag.*, **1**, 52-67, doi:10.1109/MGRS.2013.2260911.
- Ruf, C., R. Atlas, P. Chang, M. P. Clarizia, J. Garrison, S. Gleason, S. Katzberg, Z. Jelenak, J. Johnson, S. Majumdar, A. O'Brien, D. J. Posselt, A. Ridley, R. Rose, and V. Zavorotny, 2016: New Ocean Winds Satellite Mission to Probe Hurricanes and Tropical Convection. *Bull. Amer. Meteor. Soc.*, **97**, 385-395, doi:10.1175/BAMS-D-14-00218.1.
- Sanders, F. and J.R. Gyakum, 1980: Synoptic-Dynamic Climatology of the "Bomb." *Mon. Wea. Rev.*, **108**, 1589-1606.

- Schemm S., I. Rudeva and I. Simmonds, 2015: Extratropical fronts in the lower troposphere – global perspectives obtained from two automated methods. *Quart. J. Roy. Meteorol. Soc.*, **141**, 1686-1698, doi:10.1002/qj.2471.
- Schemm, S., and H. Wernli, 2014: The Linkage between the Warm and the Cold Conveyor Belts in an Idealized Extratropical Cyclone. *J. Atmos. Sci.*, **71**, 1443–1459.
- Schemm, S., H. Wernli, and L. Papritz, 2013: Warm conveyor belt in idealized moist baroclinic wave simulation. *J. Atmos. Sci.*, **70**, 627–652.
- Shapiro, M.A. and D. Keyser, 1990: Fronts, jet streams, and the tropopause. *Extratropical Cyclones, The Erik Palmén Memorial Volume*, C.W. Newton and E. Holopainen, Eds., Amer. Meteor. Soc., 167-191.
- Shapiro, M.A., 1970: On the Applicability of the Geostrophic Approximation to Upper-Level Frontal-Scale Motions. *J. Atmos. Sci.*, **27**, 408-420.
- Simmonds I., K. Keay and J. A. T. Bye, 2012: Identification and Climatology of southern hemisphere mobile fronts in a modern reanalysis. *J. Climate*, **25**, 1945-1962, doi: 10.1175/JCLI-D-11-00100.1.
- Sinclair, V. A., 2013: A 6-yr climatology of fronts affecting Helsinki, Finland, and their boundary layer structure. *J. Appl. Meteor. Clim.*, **52**, 2106-2124, doi:10.1175/JAMC-D-12-0318.1.
- Small, R. J., S. P. deSzoeko, S. P. Xie, L. O’Neill, H. Seo, Q. Song, P. Cornillon, M. Spall and S. Minobe, 2008: Air–sea interaction over ocean fronts and eddies. *Dyn. Atmos. Oceans*, **45**, 274–319, doi:10.1016/j.dynatmoce.2008.01.001.
- Spencer, R. W., H. M. Goodman, and R. E. Hood, 1989: Precipitation retrieval over land and ocean with the SSM/I: Identification and characteristics of the scattering signal. *J. Atmos. Oceanic Technol.*, **6**, 254–273.
- Stephens, G. L., D. G. Vane, R. J. Boain, G. G., Mace, K. Sassen, Z. Wang, A. J. Illingworth, E. J. O’Connor, W. B. Rossow, S. L. Durden, S. D. Miller, R. T. Austin, A. Benedetti, C. Mitrescu, and the CloudSat Science Team, 2002: The cloudsat mission and the a-train: a new dimension of space-based observations of clouds and precipitation. *Bull. Amer. Meteor. Soc.*, **83**, 1771-1790.
- Stephens, G. L., D. G. Vane, S. Tanelli, E. Im, S. Durden, M. Rokey, D. Reinke, P. Partian, G. G. Mace, R. Austin, T. L’Ecuyer, J. Haynes, M. Lebsock, K. Suzuki, D. Waliser, D. Wu, J. Kay, A. Gettelman, Z. Wang, and R. Marchand, 2008: Cloudsat mission: performance and early science after the first year of operation. *J. Geophys. Res.*, **113**, D00A18, doi:10.1029/2008JD009982.
- Stoelinga, M. T., 1996: A potential vorticity-based study of the role of diabatic heating and friction in a numerically simulated baroclinic cyclone. *Mon. Wea. Rev.*, **124**, 849-874.

- Stohl, A., 2001: A 1-year Lagrangian ‘‘climatology’’ of airstreams in the Northern Hemisphere troposphere and lowermost stratosphere. *J. Geophys. Res.*, **106** (D7), 7263–7279.
- Tselioudis G, and W. B. Rossow, 2006: Climate feedback implied by observed radiation and precipitation changes with midlatitude storm strength and frequency, *Geophys. Res. Lett.*, 33, Art. No. L02704, doi: 10.1029/2005GL024513.
- Tselioudis G., Y. Zhang and W. B. Rossow, 2000: Cloud and radiation variations associated with northern midlatitude low and high sea level pressure regimes. *J. Climate*, **13**, 312-327.
- Vaughan, G., J. Methven, D. Anderson, B. Antonescu, L. Baker, T. P. Baker, S. P. Ballard, K. N. Bower, P. R. A. Brown, J. Chagnon, T. W. Choularton, J. Chylik, P. J. Connolly, P. A. Cook, R. J. Cotton, J. Crosier, C. Dearden, J. R. Dorsey, T. H. A. Frame, M. W. Gallagher, M. Goodliff, S. L. Gray, B. J. Harvey, P. Knippertz, H. W. Lean, D. Li, G. Lloyd, O. Martínez–Alvarado, J. Nicol, J. Norris, E. Öström, J. Owen, D. J. Parker, R. S. Plant, I. A. Renfrew, N. M. Roberts, P. Rosenberg, A. C. Rudd, D. M. Schultz, J. P. Taylor, T. Trzeciak, R. Tubbs, A. K. Vance, P. J. van Leeuwen, A. Wellpott, and A. Woolley, 2015: Cloud Banding and Winds in Intense European Cyclones: Results from the DIAMET Project. *Bull. Amer. Meteor. Soc.*, **96**, 249–265. doi: <http://dx.doi.org/10.1175/BAMS-D-13-00238.1>.
- Vukovich, F. M., J. W. Dunn, and B. W. Crissman, 1991: Aspects of the evolution of the marine boundary layer during cold-air outbreaks off the southeast coast of the United States. *Mon. Wea. Rev.*, **119**, 2252-2279.
- Webster, P. J., and R. Lukas, 1992: TOGA COARE: The coupled ocean–atmosphere response experiment. *Bull. Amer. Meteor. Soc.*, **73**, 1377–1416.
- Weng F., and N. C. Grody, 2000: Retrieval of ice cloud parameters using microwave imaging radiometers. *J. Atmos. Sci.*, **57**, 1069-1081.
- Wentz, F. J., 2013: SSM/I Version-7 Calibration Report, report number 011012, *Remote Sensing Systems*, Santa Rosa, CA, 46pp.
- Wernli, H and H.C. Davies, 1997: A Lagrangian-based analysis of extratropical cyclones. I: The method and some applications. *Quart. J. Roy. Meteor. Soc.*, **123**, 467–489, doi:10.1002/qj.49712353811.
- Wernli, H., 1997: A Lagrangian-based analysis of extratropical cyclones. Part II: A detailed case-study. *Quart. J. Roy. Meteor. Soc.*, **123**, 1677-1706, doi:10.1002/qj.49712354211.
- Whittaker, J. S., and C. A. Davis, 1994: Cyclogenesis in a saturated environment. *J. Atmos. Sci.*, **51**, 889-907.